Effect of phonon interference on the thermal conductivity and heat carriers

Haoxue Han

université PARIS-SACLAY — CentraleSupélec — **École Centrale Paris**

THÈSE DE DOCTORAT DE L'UNIVERSITE PARIS-SACLAY,

préparée à CentraleSupélec

présentée par

Haoxue Han

ÉCOLE DOCTORALE N° 579
Sciences mécaniques et énergétiques, matériaux et géosciences

Spécialité de doctorat : Thermique

Effect of Phonon Interference on the Thermal Conductivity and Heat Carriers

Soutenue le 19 Octobre 2015

Jury :	M	Yu. KOSEVICH	Professeur	Président du Jury
	M	B. PERRIN	Directeur de Recherche	Rapporteur
	M	S. MERABIA	Chargé de Recherche	Rapporteur
	M	K. TERMENTZIDIS	Chargé de Recherche	Examinateur
	M	Y. CHALOPIN	Chargé de Recherche	Examinateur
	M	S. VOLZ	Directeur de Recherche	Directeur de thèse

École Centrale des Arts et Manufactures
Grand Établissement sous tutelle
du Ministère de l'Éducation Nationale
Grande Voie des Vignes
92295 Châtenay-Malabry Cedex
Tél : 33 (1) 41 13 10 00
Télex : 634 991 F EC PARIS

Laboratoire d'Énergétique Moléculaire et Macroscopique, Combustion (E.M2.C.)
UPR 288, CNRS et École Centrale Paris
Tél : 33 (1) 41 13 10 31
Fax : 33 (1) 47 02 80 35

2015 - 09

Acknowledgement

I would love to thank Ang, my wife and best friend, for her generous support and encouragement. My thanks to my parents for their unconditional love and support during my studies in France. I am always trying my best to make them proud. Words become pale in front of the hope and happiness that my family brings to me, especially at the hardest moments.

I am very grateful for the support from Dr Sebastian Volz. I couldn't find another advisor as encouraging as Sebastian who provides a great working environment. I would also like to thank Prof Yuriy Kosevich who has excited many excellent ideas on interferences and helped guide me through my second year of PhD. Thanks to Junichiro Shiomi Sensei in Tokyo University for supporting my staying in Tokyo to conduct a joint project and Takuma Shiga Sensei's help on the force constant calculations from DFT. Thanks to Professor Colin Lambert in Lancaster University for giving me a class on Green's function and the training on molecular electronics in his team. Thanks to Professor Roberto D'Agosta for giving a class on DFT in our team. I would thank the members of the Thermal Nanoscience Team and elsewhere for helpful discussions and happy times: Dr Shiyun Xiong, Dr Yuxiang Ni, Dr Shenghong Ju, Dr Kimmo Sääskilahti, Benoît Latour, Dr Wassim Kassem, Jordane Soussi, Dr José Ordonez, Dr Yann Chalopin, Dr Laurent Tranchant, Sergei Gluchko, Feng Merlin Lei, Lantao Yu and Yunhui Wu.

Finally, I would like to thank China Scholarship Council for providing the fellowship No. 201204490095 during this work and the support from EM2C laboratory and CNRS on the conference expenses.

Abstract

Wave interference of phonons can modify the phonon spectrum and thereby the group velocity and phonon population. These wave interferences allow the flow of thermal energy to be manipulated by controlling the materials lattice thermal conductivity and by using thermal mirrors to reflect thermal phonons. The technological application of the phonon interference in materials, such as enhanced thermoelectric energy conversion and improved thermal insulation, has thrusted the exploration for highly efficient wave interference materials.

First, we provide a new approach to demonstrate that heat in solids can be manipulated like light. While heat convection by fluids and heat radiation by light can be reasonably controlled, the understanding of heat conduction through solids is less straightforward and has been an important challenge both in physics and engineering. We precisely control the heat flow by designing an atomic-scale phononic metamaterial, which contains deliberate flaws in the crystalline atomic lattice, channeling the heat through different phonon paths. Destructive interference between heat waves following different paths leads to the total reflection of the heat current and thus to the remarkable reduction in the material ability to conduct heat. By exploiting this destructive phonon interference, we model a very counter-intuitive possibility of thermal transport: more heat flow is blocked by the opening of additional phonon channels. Our thermal metamaterial is a good candidate for high-finesse atomic-scale heat mirrors. We provide an important further insight into the coherent control of phonons which can be applied both to sound and heat propagation.

Secondly, we introduce a novel ultra-compact nanocapacitor of coherent phonons formed by high-finesse interference mirrors based on atomic-scale semiconductor metamaterials. Our molecular dynamics simulations show that the nanocapacitor stores monochromatic terahertz lattice waves, which can be used for phonon lasing - the emission of coherent phonons. Either one- or two-color phonon lasing can be realized depending on the geometry of the nanodevice. The two-color regime of the interference cavity originates from different incidence-angle dependence of phonon wave packet transmission for two wave polarizations at the respective antiresonance frequencies. Coherent phonon storage can be achieved by cooling the nanocapacitor initially thermalized at room temperature or by

the pump-probe technique. The linewidth narrowing and the computed relative phonon participation number confirm strong phonon confinement in the interference cavity by an extremely small amount of resonance defects. The emission of coherent terahertz acoustic beams from the nanocapacitor can be realized by applying tunable reversible stress which shifts the antiresonance frequencies.

Finally, we investigate the role of two-path destructive phonon interference induced by long-range interatomic forces on the thermal conductance and conductivity of a silicon-germanium alloy by atomistic calculations. The thermal conductance across a germanium atomic plane in the silicon lattice is substantially reduced by the destructive interference of the nearest-neighbour phonon path with a direct path bypassing the defect atoms. Such an interference causes a fivefold reduction in the lattice thermal conductivity in a SiGe alloy at room temperature. We demonstrate the predominant role of harmonic phonon interferences in governing the thermal conductivity of solids by suppressing the inelastic scattering processes at low temperature. Such interferences provide a harmonic resistive mechanism to explain and control heat conduction through the coherent behaviors of phonons in solids.

Résumé

L'interférence des ondes de phonon peut modifier le spectre de phonons et ainsi la vitesse de groupe et la population de phonons. Ces interférences permettent de manipuler le flux d'énergie thermique en contrôlant la conductivité thermique et en utilisant des miroirs pour réfléchir les phonons. L'application technologique de ces interférence de phonons dans les matériaux, par exemple l'amélioration des performances de conversion thermoélectrique et l'optimisation des propriétés d'isolant thermique de certains matériaux, a propulsé l'exploration des matériaux incluant les interférences de phonons plus efficaces.

Dans un premier temps, nous proposons une nouvelle approche pour démontrer que la chaleur dans les solides peut être manipulée comme la lumière. Nous contrôlons avec précision le flux thermique par le bias d'un métamatériau qui comporte des défauts dans son réseau cristallin. Les interférence destructive entre les ondes de chaleur suivant différents chemins mène à la réflexion totale de certains modes de phonon et à une réduction remarquable de la conductance thermique. En exploitant cette interférence, nous obtenons un résultat contre-intuitif concernant le transport thermique: plus de chaleur est bloquée par l'ouverture des canaux additionnels de phonon. Ce métamatériau thermique est un bon candidat pour jouer le rôle de miroir atomique thermique de haute finesse. Nous renforçons la compréhension sur le contrôle des phonons thermique par des effets de cohérence qui peuvent être appliqués à la fois au son et à la propagation de chaleur.

Dans un deuxième temps, nous introduisons un nano-condensateur ultra-compact de phonons cohérents formé par les miroirs interférenciels de haute finesse basés sur un métamatériau semi-conducteur à l'échelle atomique. Nos simulations de dynamique moléculaire montrent que le nano-condensateur stocke les ondes monochromatiques TéraHertz, qui peuvent et peut être utilisé comme un laser à phonons à travers l'émission de phonons cohérents. Un laser à phonon soit d'une ou de deux couleurs peut être réalisé en fonction de la géométrie du nano-dispositif. Le stockage des phonons cohérents peut être réalisé par le refroidissement du nano-condensateur initialement thermalisé à la température ambiante ou excité à l'aide de lasers de pompe. Le rétrécissement de la largeur de raie et du nombre relatif de participation de phonons confirme un

confinement dans la nanocavité généré par une quantité extrêmement faible de défauts de résonance. L'émission d'impulsions acoustiques cohérentes TeraHertz du nano-condensateur peut être réalisé en appliquant une contrainte réversible accordable qui décale les fréquences d'antirésonance.

Enfin, nous étudions l'effet des interférences destructrice entre des phonon issus de deux chemins induit par les forces interatomiques de longue portée sur la conductance thermique et la conductivité d'un alliage silicium-germanium par des calculs atomiques. La conductance thermique à travers un plan atomique de germanium dans un réseau de silicium est sensiblement réduite par les interférences destructrices entre les phonons suivant des chemins définis par l'interaction avec l'atome voisin et avec l'atome suivant. Une réduction d'un facteur cinq de la conductivité thermique dans un alliage SiGe à la température ambiante a été observée en introduisant les forces de longue portée. Nous démontrons le rôle prédominant des interférences harmoniques de phonons régissant la conductivité thermique des solides en supprimant la diffusion inélastique de phonon à basse température. De telles interférences fournissent un mécanisme résistif harmonique pour contrôler la conduction de chaleur à travers les comportements cohérents des phonons dans les solides.

Contents

List of Figures

Chapter 1

Introduction

Wave interference of phonons can modify the phonon spectrum and thereby the group velocity and phonon population. These wave interferences allow the flow of thermal energy to be manipulated by controlling the material lattice thermal conductivity and by using thermal mirrors to reflect thermal phonons. The technological application of the phonon interference in materials, such as enhanced thermoelectric energy conversion and improved thermal insulation, has thrusted the exploration for highly efficient wave interference materials. In the Introduction of this thesis, we discuss recent developments in the understanding and coherent control of heat transport. The rational design and fabrication of nanostructures provides unprecedented opportunities for creating wave-like behaviour of heat, leading to a fundamentally new approach for manipulating the transfer of thermal energy.

1.1 Phonon as a wave

Heat conduction is made possible mainly by the Brownian motion of heat carriers such as phonons, electrons, or molecules. During the last two decades, phonon transport in micro- and nano-structures is found to exhibit distinct features compared to their behaviours in bulk materials and strongly depends on the system size. As the characteristic dimension of the system approaches the mean free path of the heat carriers, the thermal transport undergoes a transition from a diffusive to a ballistic regime. The wave nature of phonons thereby becomes a fundamental and crucial phenomenon to be understood in the hope of tailoring the thermal transport of nano-materials. The engineering of thermal transport by exploiting the coherent behaviour of phonons in solids is of fundamental interest and could also be exploited in applications.

Recent development of advanced theoretical and experimental methods allow for precise control of heat transport at mesoscopic scale and is important across a number of research domains, including high efficiency thermoelectrics [Snyder

and Toberer (2008); Bell (2008); Venkatasubramanian et al. (2001); Hsu et al. (2004); Hochbaum et al. (2008); Poudel et al. (2008); Biswas et al. (2012)], nanoelectronics [Tian et al. (2007)], fuel cells [Steele and Heinzel (2001)], thermal barrier coatings [Padture et al. (2002)] and ultralow thermal conductivity materials [Costescu et al. (2004); Chiritescu et al. (2007)]. Since the past few decades, engineering heat transport in nanostructured materials has been achieved mainly by the introduction of atomics-cale impurities, nanoparticles, interfaces and grain boundaries [Toberer et al. (2012); Vineis et al. (2010); Cahill et al. (2014); Zebarjadi et al. (2012)]. The diffuse scattering of phonons on these structural defects reduce heat flow. In contrast, recently a new approach for controlling nanoscale heat transport involves the coherent reflection and transmission of thermal phonons at interfaces [Luckyanova et al. (2012); Ravichandran et al. (2014); Simkin and Mahan (2000); Zen et al. (2014); Maldovan (2013); Alaie et al. (2015)]. The resulting phonon interference modifies the phonon band structure. The phonons travel ballistically in the structure until they are scattered at the boundaries. Coherent wave transport of electrons moving in semiconductor materials [Ashcroft and Mermin (1976); Kittel (2005)] and photons in photonic crystals have been widely demonstrated [Yablonovitch (1987); John (1987); Joannopoulos et al. (1997)]. The wave interferences are well understood for the case of electrons. Analogous acoustic wave interferences have been employed to achieve complete sound reflections and a number of new acoustic devices [Kushwaha et al. (1993); Liu et al. (2000)]. Given the remarkable success in electronic, photonic and phononic wave interference to manipulate electrons, light and sound waves, it is certainly beneficial to find its counterpart in thermal vibrations, thereby enabling a new twist for manipulating heat flow.

1.2 Phonon interference in thermal transport

Generally in the transport processes, the heat flow depends on the energy of heat carriers (phonon), their number (phonon population), the moving speeds (group velocities) and the average distances travelled before scattering (mean free paths). Under the single-mode-relaxation-time approximation via kinetic theory, the thermal conductivity κ of a 3D lattice is given by,

$$\kappa = \frac{1}{3}\sum_{\mathbf{q}} C_{\mathbf{q}} v_{\mathbf{q}}^2 \tau_{\mathbf{q}}, \tag{1.1}$$

where $C_{\mathbf{q}}$ and $v_{\mathbf{q}}$ are the specific heat per volume unit and the group velocity of the $\mathbf{q}$-th phonon mode. The phonon relaxation time (RT) τ measures the temporal response of a perturbed phonon mode to relax back to equilibrium due to the net effect of different phonon scattering mechanisms. The specific heat indicates the temperature derivative of the energy a certain mode $\mathbf{q}$ carries, the group velocity indicates how fast phonons of the mode propagate, and the

lifetime (mean free path) indicates how long (far) phonons of the mode $\mathbf{q}$ travel on average before being scattered. The phonon mean free path (MFP) $\Lambda_{\mathbf{q}}$ is defined as $\Lambda_{\mathbf{q}} = v_{\mathbf{q}}\tau_{\mathbf{q}}$.

Different phonon transport properties can be identified from Eq. (1.1) that are relevant to controlling heat conduction. Most common approaches to tailor the thermal conductivity focus on the phonon relaxation time, for example, by introducing point defects [Kim et al. (2006)] and internal or external surfaces that scatter phonons diffusely [Chiritescu et al. (2007); Toberer et al. (2012)]. The bulk normal phonon modes, more precisely their phonon spectrum and the group velocities, are not substantially modified in these defective structures and thermal conductivity is reduced by enhancing the phonon scattering rate $\tau_{\mathbf{q}}^{-1}$. This principle has been used widely to enhance the efficiency of thermoelectrics [Snyder and Toberer (2008); Bell (2008); Venkatasubramanian et al. (2001); Hsu et al. (2004); Hochbaum et al. (2008); Poudel et al. (2008); Biswas et al. (2012)]. On the other hand, the wave interference of thermal phonons allows for the control of heat flow and thermal conductivities in nanostructures by manipulating the phonon eigenfrequencies and phonon group velocities [Luckyanova et al. (2012); Ravichandran et al. (2014); Simkin and Mahan (2000); Zen et al. (2014); Maldovan (2013); Alaie et al. (2015)]. The wave interference-based approach controls the nanoscale heat conduction by modifying physical transport properties that cannot be influenced by classical approaches, which rely on diffuse phonon scattering.

The Bragg reflection of waves incident on a layered structure happens when the multiple reflections of waves are in phase: they interfere constructively and thus prevent the original wave from propagating within the structure, whereas the out-of-phase multiple reflected waves do not interfere constructively and they are permitted to propagate. The strong wave interference occurs when $n\lambda \approx 2a_0$ where λ is the wavelength and n is an integer, a_0 is the thickness of a unit layer. The range of frequencies for which the original wave is forbidden from propagating within the structure is known as the bandgap. The wave interference effects are not restricted to the propagation perpendicular to multilayer structures. Another basic condition for Bragg reflection to happen is that the interface roughness should be smaller than the principal wavelength of the incident phonons.

Coherent phonons in superlattices (SLs) have been observed with Raman and acoustic reflection and transmission experiments [Colvard et al. (1980); Wang et al. (2005); Narayanamurti et al. (1979)]. The term "coherent" in describing waves is used to characterize monochromatic waves and implies a measurable phase relationship for a given time interval during wave propagation [Luckyanova et al. (2012)]. Although this definition applies to a monochromatic wave, it is difficult to apply it to heat conduction, where a wide spectrum of

phonons are thermally excited in a structure. Taken the heat conduction in a thin film as an example, in the Casimir classical size effect regime, broadband phonons thermally excited at one boundary travel through the interior of the film ballistically. The phonon propagation inside the film then can be considered as coherent.

To observe the wave-like behaviour of thermal phonons, periodic structures with smooth interfaces are favorably chosen. Interfaces with very good quality favour the specular reflection and transmission of phonons. It was recently shown that thermal phonons travel coherently as they cross the many interfaces of such structures [Luckyanova et al. (2012)], since the superlattice thermal conductivity linearly depends on the number of layers. If diffusive scattering occurs at the interfaces, the MFP is defined by the constituent layer thickness. Therefore the layers can be considered as independent thermal resistors in series (parallel) to obtain the cross-plane (in-plane) thermal conductivity of the superlattice, which is independent of the layer number. In this case, the superlattice is considered as a compound in which each layer has it own phonon dispersion. On the other hand, if the phonons remain coherent when crossing the interfaces, the superlattice should be considered as a homogeneous material and the thermal conductivity will be linearly proportional to the total thickness.

In an experimental demonstration [Luckyanova et al. (2012)], five GaAs/AlAs superlattices were fabricated using metal organic chemical vapour deposition, with periods of 1, 3, 5, 7 and 9, where each period consisted of a 12 nm GaAs and a 12 nm AlAs layer as shown in Fig. 1.1(a). The thermal conductivities of the superlattices were measured using the time-domain thermal reflectance (TDTR) at temperatures of 30-300 K in Fig. 1.1(b). For temperatures from 30 to 150 K, the thermal conductivity shows a linear dependence with superlattice's total thickness, demonstrating that thermal phonons travel through the interfaces coherently. This linear dependence breaks down for thick samples at temperatures above 150 K, which suggests that the inelastic processes become important in the phonon transport. The authors also claim that most of the phonons that contributed to the measured thermal conductivity in superlattices travel through the structures ballistically and were also coherent. The coherence of high-frequency phonons was destroyed by interface roughness but not the low-frequency phonons. The large reduction in thermal conductivity resulted from the loss of coherence of high-frequency phonons, but the lower-frequency phonons that contribute to the thermal conductivity were mostly coherent during their transport through the structures.

Another experiment succeeded in achieving atomically smooth interfaces by

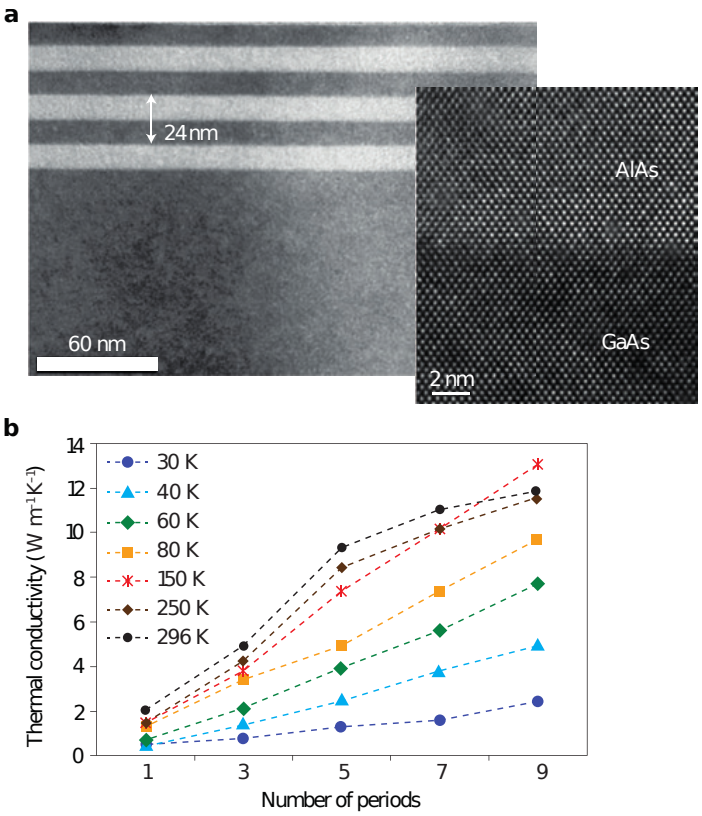

Figure 1.1: *Wave-like heat transport and wave interference in GaAs/AlAs superlattices. (a) Transmission electron microscopy (TEM) image of a 3-period GaAs/AlAs superlattice with periodicity a = 24 nm, where the inset shows a high-resolution image of one of the interfaces [Luckyanova et al. (2012)]. (b) Experimental thermal conductivity as a function of the number of periods at different temperatures. Thermal conductivity rises as the number of periods increases, which indicates that phonons cross the interfaces coherently.*

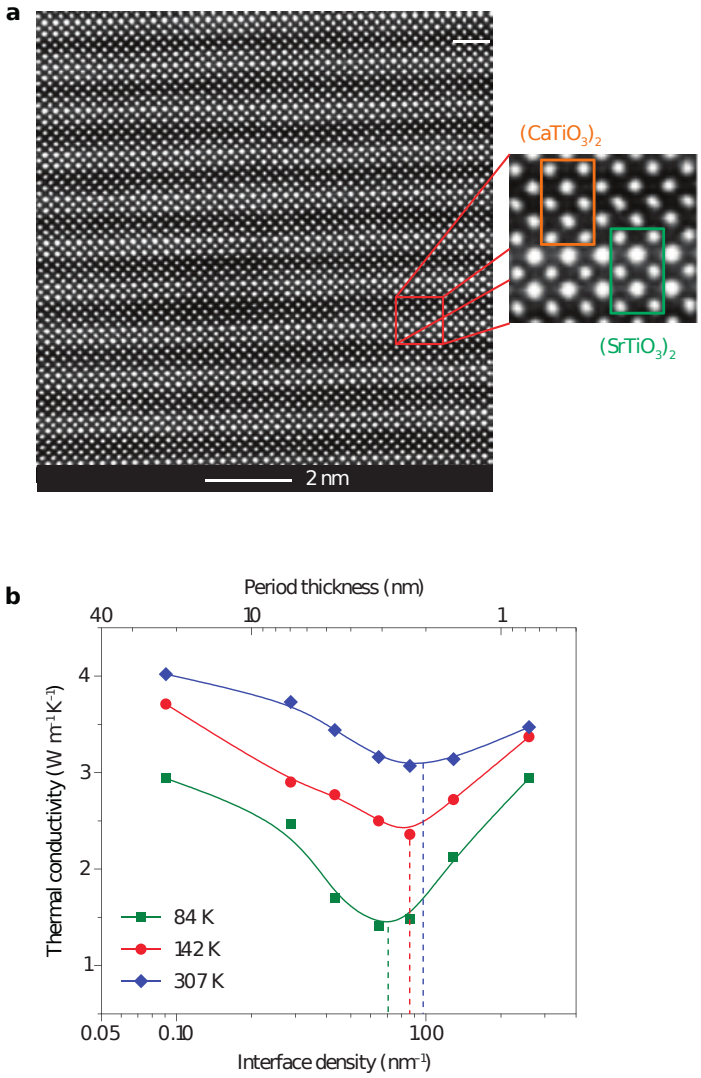

Figure 1.2: *Wave-like heat transport and wave interference in SrTiO3/CaTiO3 superlattices. (a) Transmission electron microscopy (TEM) image of a SrTiO3/CaTiO3 superlattice with atomically sharp interfaces [Ravichandran et al. (2014)]. (b) Measured thermal conductivity of the superlattice as a function of the period thickness (or interface density) at different temperatures. The solid lines are visual guides. The presence of a local minimum value (vertical dashed lines) for the thermal conductivity reveals wave interference effects for thermal vibrations within the superlattice. Wave effects become stronger as the temperature is decreased.*

using high-quality oxide superlattices grown through molecular beam epitaxy, shown in Fig. 1.2 [Ravichandran et al. (2014)]. The thermal conductivities of superlattices were measured as a function of periodicity using the TDTR technique. Fig. 1.2 shows the measured room temperature thermal conductivity of the superlattices κ_{SL}. In the low interface-density regime, κ_{SL} rises with increasing period, an indicator that phonon behaves primarily like particles that are scattered diffusely at the interfaces. The system can be modeled as a series of bulk thermal resistances with the resistance of the interfaces added in series with the bulk resistances. In this incoherent regime, the behaviour of the phonons is particle-like and hence the thermal resistance increases linearly with increasing interface density. On the other hand, for small periodicities, κ_{SL} decreases with increasing period. Because this behaviour is not compatible with the presence of only diffuse scattering, part of the phonons are more close to waves experiencing interference effects. The wave nature of phonons must be considered. The thermal conductivities in Fig. 1.2 can be divided into two regimes based on whether the thermal conductivity increases (coherent) or decreases (incoherent) with increasing interface density. Even at small periodicities, incoherent surface scattering effects remain due to interface imperfections. These data show the existence of a minimum thermal conductivity for superlattices as a function of period, revealing that interference effects of phonon considered as waves can be present at room temperature. It is important to note that the portion of heat carried by long-wavelength phonons increases if the temperature is lowered to levels well below its Debye temperature. The ratio between phonon wavelengths and interface roughness can thus be increased, which favours specular reflection and transmission. When the temperature was reduced from 307 K to 84 K, experiments showed a deeper and clearer minimum for the thermal conductivity (Fig. 1.2), which provides evidence for stronger interference effects at low temperatures.

Bragg phonon interference effects for thermal transport have also been demonstrated in two-dimensional periodic porous thin films [Zen et al. (2014); Alaie et al. (2015)]. Because porous structures do not generally have atomically sharp interfaces, such experiments are performed at very low temperatures ($T < 1$ K) to make the dominant phonon wavelength much longer than the roughness of the films. In this low temperature regime, the dominant phonon wavelengths are expected to increase by two orders of magnitude with respect to those at room temperature, which saves the need for high-quality interfaces. We note that at room temperature, the reduction of the thermal conductivity in porous silicon films is less likely to result from wave interference effects. Diffuse phonon scattering should dominate heat transport in porous silicon at room temperature due to the short wavelengths of heat-carrying phonons [Maldovan (2013)]. In [Zen et al. (2014)], a phononic crystal with square arrays of cylindrical holes was fabricated on single crystal (100) Si wafers with silicon nitride films grown

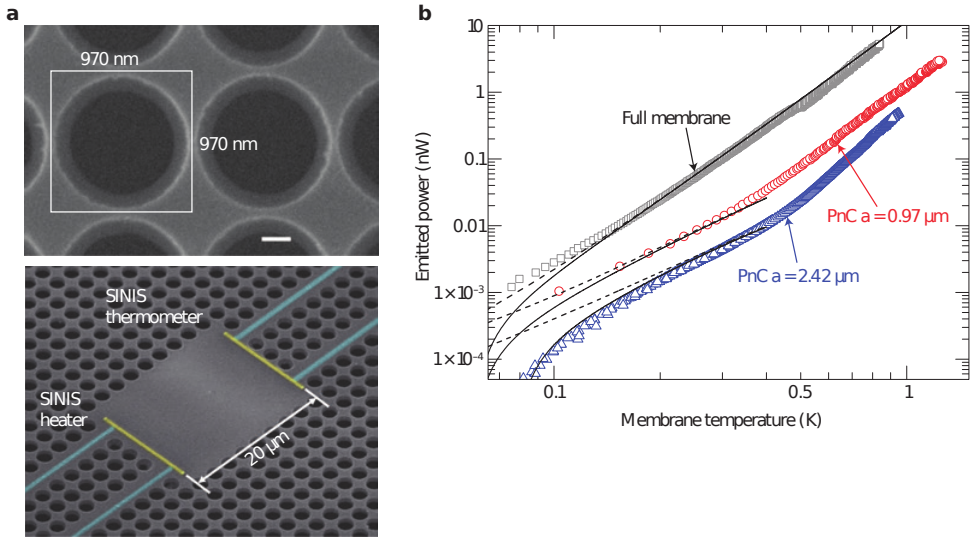

Figure 1.3: *Thermal phonon engineering in porous films. (a) Top: Scanning electron microscopy (SEM) image of a periodic porous thin-film made from a square array of air cylinders with periodicity a_0 = 970 nm on a silicon nitride matrix [Zen et al. (2014)]. Scale bar: 200 nm. Bottom: SEM image showing the Al (blue) and Cu (yellow) wires that form the heater and thermometer at the centre of the periodic porous film sample with a_0 = 2.42 Î¼m. SINIS: superconductor/insulator/normal metal/insulator/superconductor. (b) Emitted thermal power measured as a function of temperature. Phononic crystal (PnC) samples with a_0 = 0.97 µm and a_0 = 2.42 µm are shown. Uniform (unperforated) film is shown with grey squares. Theoretical calculations with and without back radiation from the substrate are shown by solid and dashed lines, respectively.*

by low-pressure chemical vapour deposition and electron-beam lithography and two-angle shadow mask technique was used to deposit the tunnel junction thermometer, see Fig. 1.3(a). With a periodicity of $a_0 \approx 1\mu$m, the phononic crystal shows a phononic bandgap around gigahertz frequencies, which corresponds to the dominant frequencies of heat carriers at such low temperatures. The dependence of the measured emitted power P versus measured membrane temperature for the PnC samples and the full membrane are shown in Fig. 1.3(b), up to about 1 K. The emitted power is remarkably reduced for both PnC at all temperatures, compared to the full membrane result. More importantly, the PnC which has the maximal band gap actually has a higher thermal conductance than the one whose bandgap is narrower. This demonstrates a counter-intuitive effect that the minimum thermal conductivity is not achieved with the largest bandgap. Such a fact is another demonstration of the intriguing role of phonon wave interference in nanostructured materials.

1.3 Basics of phonons

In solid crystals, atoms or molecules are regularly arranged in an array of sites in the real space, which is known as the *lattice*. A lattice describes a highly ordered structure, occurring due to the intrinsic nature of molecules to form symmetric patterns. The whole lattice can be constructed by suitable translations of the *unit cell*, which is the basic unit of the lattice. At any finite temperature, atoms vibrate about their equilibrium positions. Under the classical approximations, those atom motions can be mathematically described by the Newton's second law if the force applied on each atom and the atomic mass are known.

1.3.1 One-dimensional open system of coupled masses

To simplify the formulation, we consider here an mono-atomic chain with coupling constant and atomic mass denoted as γ and m, respectively. The dynamical equation of a 1D open system of masses coupled through springs writes,

$$\gamma\psi_1 - \gamma\psi_2 = E\psi_1, \tag{1.2a}$$
$$2\gamma\psi_j - \gamma\psi_{j+1} - \gamma\psi_{j-1} = E\psi_j, \text{ for } j \in [2, N-1] \tag{1.2b}$$
$$\gamma\psi_N - \gamma\psi_{N-1} = E\psi_N. \tag{1.2c}$$

where E is the energy and ψ_j denotes the wave function of atom j.

A general solution of Eq. (1.2) writes,

$$\psi_j = \mathrm{e}^{ikj} + C\mathrm{e}^{-ikj} \tag{1.3}$$

Replacing Eq. (1.3) into Eq. (1.2b), one gets

$$\epsilon_0 - \gamma(\mathrm{e}^{ik} + \mathrm{e}^{-ik}) = E$$

where ϵ_0 denotes the on-site energy. Thus the dispersion relation writes,

$$E = \epsilon_0 - 2\gamma \cos k \tag{1.4}$$

If one introduces the eigenfrequency ω, $E = m\omega^2$. Replacing the general solution Eq. (1.3) in to Eq. (1.2b), one recognizes the well-know phonon dispersion relation of a 1D mono-atomic lattice,

$$E = 4\gamma \sin^2 \frac{k}{2} \tag{1.5}$$

In the irreducible Brillouin Zone $k \in [0, \pi]$, the frequency can be expressed as

$$\omega = \omega_\Theta \sin \frac{k}{2} \tag{1.6}$$

where $\omega_\Theta = 2\sqrt{\gamma/m}$ is the Debye frequency of the lattice. Replacing Eq. (1.3) in to Eq. (1.2a), one gets

$$\psi_1 - \psi_2 = 2(1 - \cos k)\psi_1$$

considering $2\cos k = \mathrm{e}^{ik} + \mathrm{e}^{-ik}$, the boundary condition for the wave functions can be written as

$$\psi_1 - (\mathrm{e}^{ik} + \mathrm{e}^{-ik})\psi_1 + \psi_2 = 0$$

Then the constant C is defined as

$$C = \frac{1 - \mathrm{e}^{ik}}{\mathrm{e}^{-ik} - 1} = \mathrm{e}^{ik}$$

Replacing Eq. (1.3) in to Eq. (1.2c) yields,

$$\psi_N - (\mathrm{e}^{ik} + \mathrm{e}^{-ik})\psi_N + \psi_{N-1} = 0$$

considering $C = \mathrm{e}^{ik}$, the following new boundary condition arises

$$(1 - \mathrm{e}^{ik})(\mathrm{e}^{ikN} + \mathrm{e}^{-ikN}) = 0$$

which reduces to $\sin kN = 0$, and

$$k = \frac{n}{N}\pi \tag{1.7}$$

Hence the eigenvectors are

$$\psi_j(n) = \mathrm{e}^{ikj} + \mathrm{e}^{ik}\mathrm{e}^{-ikj} \tag{1.8}$$
$$= \mathrm{e}^{ik/2}\left(\mathrm{e}^{ik(j-1/2)} + \mathrm{e}^{-ik(j-1/2)}\right)$$
$$= 2\mathrm{e}^{ik/2}\cos\frac{n}{N}\pi\left(j-\frac{1}{2}\right) \tag{1.9}$$

We now evaluate the wave functions to establish the energy number n in the wave function of the phonons (Eq. (1.9)). $\psi_j(N) = 0$ which is not a physically admissible solution is therefore rejected. $\psi_j(-n) = \psi_j(n)$ which are linearly dependent. $\psi_j(N+m) = -\psi_j(N-m)$ which means that for $n > N$ the orbitals periodically repeat the interval $[0, N-1]$. For $n = 0$, the orbital $\psi_j(0) = 1$ which corresponds to the overall translation of the system, is kept as a possible solution for n.

Finally, for a open 1D mass-spring (MS) system of N orbitals, one has

$$n \in [0, 1, 2, \cdots N-1]. \tag{1.10}$$

1.3.2 Periodic Boundary Condition

For 1D tight-binding chain with periodic boundary conditions, the Schrödinger equation write,

$$\epsilon_0\psi_1 - \gamma\psi_2 - \gamma\psi_N = E\psi_1, \tag{1.11a}$$
$$\epsilon_0\psi_j - \gamma\psi_{j+1} - \gamma\psi_{j-1} = E\psi_j, \text{ for } j \in [2, N-1] \tag{1.11b}$$
$$\epsilon_0\psi_N - \gamma\psi_{N-1} - \gamma\psi_1 = E\psi_N. \tag{1.11c}$$

One can adopt an "easy alternative" to solve the Schrödinger equations (1.11).

Comparing Eq. (1.11b) for $j = 1$ and Eq. (1.11a),

$$\epsilon_0\psi_1 - \gamma\psi_2 - \gamma\psi_0 = E\psi_1$$
$$\epsilon_0\psi_1 - \gamma\psi_2 - \gamma\psi_0 - \gamma\psi_N + \gamma\psi_0 = E\psi_1$$

one gets $\psi_0 = \psi_N$.

Similarly, comparing Eq. (1.11b) for $j = N$ and Eq. (1.11c),

$$\epsilon_0\psi_N - \gamma\psi_{N+1} - \gamma\psi_{N-1} = E\psi_N$$
$$\epsilon_0\psi_N - \gamma\psi_{N+1} - \gamma\psi_{N-1} - \gamma\psi_1 + \gamma\psi_{N+1} = E\psi_N$$

one gets $\psi_1 = \psi_{N+1}$. Since $\psi_j(N) = \psi_j(0) \neq 0$ and $\psi_j(N+m) = \psi_j(m)$, it turns out that $n \in [0, 1, \cdots, N-1]$ or $n \in [-1, 0, 1, \cdots, N-2]$, etc. Conventionally,

one chooses an interval that is symmetric with respect to the origine. For example, if $N = 5$, then $n \in [-2, -1, 0, 1, 2]$. If $N = 6$, then $n \in [-2, -1, 0, 1, 2, 3]$. Note different order of degeneracy exists for an even or odd N. The wave functions here are the same as an open system discussed in Sec. 1.3.1.

1.3.3 Normal modes and phonon energy

The Hamiltonian of the system can be written as:

$$H = \frac{1}{2m}\sum_n p_n^2 + \frac{1}{2}\gamma\sum_n (2u_n^2 - u_n u_{n+1} - u_n u_{n-1}) \tag{1.12}$$

where u_n and p_n are the displacement and momentum of the n^{th} atom, respectively.

One can transform the displacements and the momenta into coordinates of the reciprocal space,

$$U_q = \frac{1}{\sqrt{N}}\sum_n u_n e^{iqn} \qquad P_q = \frac{1}{\sqrt{N}}\sum_n p_n e^{-iqn} \tag{1.13}$$

The corresponding inverse transform reads,

$$u_n = \frac{1}{\sqrt{N}}\sum_q U_q e^{-iqn} \qquad p_n = \frac{1}{\sqrt{N}}\sum_q P_n e^{iqn} \tag{1.14}$$

Substituting Eq. (1.14) into the Hamiltonian expression Eq. (1.12) and simplifying it, one obtains [Ziman (1960)]:

$$H = \frac{1}{2M}\sum_q P_q P_{-q} + K\sum_q U_q U_{-q}(1 - \cos q) \tag{1.15}$$

The states labelled with q and -q corresponding to running waves in the opposite directions. It can be easily find from the Fourier transform (Eq. (1.13)) that the pairs $P_q - P_{-q}$ and $U_q - U_{-q}$ are complex conjugate to each other, i.e., $P_q^* = P_{-q}, U_q^* = U_{-q}$. So Eq. (1.15) can be recasted as,

$$H = \frac{1}{2}\sum_q \{\frac{1}{M} P_q P_q^* + 2K(1 - \cos q) U_q U_q^*\} \tag{1.16}$$

Let's now introduce the second coordinate operators, a_q and a_q^*, which are defined in terms of P_q and U_q by the relations,

$$\begin{aligned} a_q &= \sqrt{\frac{1}{2m\hbar\omega}} P_q - i\sqrt{\frac{K(1 - \cos q)}{\hbar\omega}} U_q^* \\ a_q^* &= \sqrt{\frac{1}{2m\hbar\omega}} P_q^* + i\sqrt{\frac{K(1 - \cos q)}{\hbar\omega}} U_q \end{aligned} \tag{1.17}$$

It can be shown that the commutation of the above defined operators have the specially simple form,

$$[a_q, a_q^*] = (i/2\hbar)\{[P_q, U_q] + [P_q^*, U_q^*]\} = 1 \tag{1.18}$$

Consequently the Hamiltonian reduces to

$$H = \sum_q \hbar\omega(a_q^* a_q + \frac{1}{2}) \tag{1.19}$$

The operators defined in Eq. (1.17) are known as the *annihilation* and *creation operators*. And $n_q \equiv a_q^* a_q$ is called the number operator, whose eigenstates are characterized by sets of positive integers which tell us the number of 'particles' present in the field, or the number of *quanta* in the particular mode. So the total energy in the system is quantized with the quantum energy $\hbar\omega$. Having analysed the motion into quanta distributed over the various modes, it was found convenient to give to each of such quantum the name of *phonon*. Phonons bear exactly the same relation to the vibrations of the solid as do *photons* to the vibrations of the electromagnetic field. We sometimes talk of them as if they were particles ('phonon gas'), but this is only in the Pickwickian sense. Unlike the atoms which make up an ordinary gas, thermal phonons can be created and destroyed by random energy fluctuations. In the language of statistical mechanics this means that the chemical potential for adding a phonon is zero.

The phonon states comply to the Boltzmann definition of entropy and as those states exist within the canonical ensemble, the distribution of phonons are governed by the Bose-Einstein statistics, which reads,

$$n_{BE} = \frac{1}{\exp(\frac{\hbar\omega}{k_B T}) - 1} \tag{1.20}$$

where k_B is the Boltzmann constant, and T is the absolute temperature. At absolute zero temperature, there are no phonons in a crystal. At low temperatures $\hbar\omega \gg k_B T$, $n \approx \exp(-\hbar\omega/k_B T)$ and the probability of a phonon to be present is exponentially decreasing with frequency. At high temperatures $\hbar\omega \ll k_B T$, $n \approx k_B T/\hbar\omega$ and the phonon number increases linearly with temperature and the phonon mode energy is constant $E = k_B T$.

1.4 Organization of the Thesis

The thesis is started by studying a phonon mirror that perfectly reflects the phonons of the antiresonance modes due to interferences. Such a mirror allows for the study of a phonon capacitor that stores a single phonon mode and emits coherent phonons as a stress is applied. Finally, we reveal the role of phonon interference effects on the low lattice thermal conductivity of the crystals where

long range forces are present.

In Chapter 2, we briefly present the method of molecular dynamics simulations and different popular techniques to access the important thermal transport quantities, that is, phonon transmission function/probability, interface thermal conductance and lattice thermal conductivity.

In Chapter 3, we provide a new approach to demonstrate that heat in solids can be manipulated like light. While heat convection by fluids and heat radiation by light can be reasonably controlled by several means, the understanding of heat conduction through solids is less straightforward and has been an important challenge both in physics and engineering. Heat at room temperature is carried by lattice vibrations of ultra-high frequencies (10^{12} Hz), which are the abovementioned phonons, the quasi-particles that are analogous to the photons that carry light. In this chapter, we show how to precisely control the heat flow by *atomic-scale phononic metamaterial*, which contains deliberate flaws in the crystalline atomic lattice, channeling the heat through different phonon paths. Destructive interference between heat waves following different paths leads to the total reflection of the heat current and thus to the remarkable reduction in the material ability to conduct heat. By exploiting this destructive phonon interference, we model a very counter-intuitive possibility of thermal transport: more heat flow is blocked by the opening of the additional phonon channels. We provide an important further insight into the coherent control of phonons which can be applied both to sound and heat propagation.

In Chapter 4, we introduce a novel ultra-compact nanocapacitor of coherent phonons formed by high-finesse interference mirrors based on atomic-scale semiconductor metamaterials. Our molecular dynamics simulations show that the nanocapacitor stores monochromatic terahertz lattice waves, which can be used for phonon lasing - the emission of coherent phonons. Either one- or two-color phonon lasing can be realized depending on the geometry of the nanodevice. The two-color regime of the interference cavity originates from different incidence-angle dependence of phonon wave packet transmission for two wave polarizations at the respective antiresonances. Coherent phonon storage can be achieved by cooling the nanocapacitor initially thermalized at room temperature or by the pump-probe technique. The linewidth narrowing and the computed relative phonon participation number confirm strong phonon confinement in the interference cavity by an extremely small amount of resonance defects. The emission of coherent terahertz acoustic beams from the nanocapacitor can be realized by applying tunable reversible stress which shifts the antiresonance frequencies.

In Chapter 5, we investigate the role of two-path destructive phonon interference induced by long-range interatomic forces on the thermal conductance

and conductivity of a silicon-germanium alloy by atomistic calculations. The thermal conductance across a germanium atomic plane in the silicon lattice is substantially reduced by the destructive interference of the nearest-neighbour phonon path with a direct path bypassing the defect atoms. Such an interference causes a fivefold reduction in the lattice thermal conductivity in a SiGe alloy at room temperature. We demonstrate the predominant role of harmonic phonon interferences in governing the thermal conductivity of solids by suppressing the inelastic scattering processes at low temperature. Such interferences provide a "harmonic resistive" mechanism to explain and control heat conduction through the coherent behaviours of phonons in solids.

Finally, we conclude the thesis in Chapter 6.

Chapter 2

Atomistic Simulation of Phonon Transport

In this chapter, we briefly present the method of molecular dynamics simulations and different popular techniques to access the important thermal transport physical quantities, that is, phonon transmission function/probability, interface thermal conductance and lattice thermal conductivity.

2.1 Classical molecular dynamics

Molecular dynamics (MD) simulation is a numerical method to explicitly simulate the motions of particles, e.g. atoms, ions ... In classical MD simulations, these particles interact via relatively simple analytical interatomic potential functions, in which the interaction details of electrons are not considered. Newton's equations of motion are integrated for all particles simultaneously. Depending on the specific model, the particle number can reach one million using high performance computing facilities for a system time from picoseconds to microseconds.

2.1.1 Generality

Molecular dynamics simulations consist in the computation of the motions of individual atoms in order to model the behaviors of solids, liquids and gases. A MD simulation generates a sequence of points in phase space of a thermodynamic ensemble connected in time. The result tracks the trajectories of all particles in the system as a function of time. Transport and other properties can be calculated by taking the ensemble average of the trajectories.

In a classical MD simulation, the empirical potential energy of a system of particles can be expressed as a sum of terms involving single, pairs, triplets, and so forth, of atoms:

$$\mathrm{U} = \sum_i \mathrm{U}_1(\mathbf{r}_i) + \sum_i \sum_{j>i} \mathrm{U}_2(\mathbf{r}_i, \mathbf{r}_j) + \sum_i \sum_{j>i} \sum_{k>j>i} \mathrm{U}_3(\mathbf{r}_i, \mathbf{r}_j, \mathbf{r}_k) + \ldots \quad (2.1)$$

The first term in the potential energy function, $\mathrm{U}_1(\mathbf{r}_i)$, can be used to incorporate the effect of an external field acting on the system. All the remaining terms represent particle-particle interactions.

The motion of each atom is governed by Newton's second law, which is given by:

$$\frac{d^2\mathbf{r_i}}{dt^2} = \frac{\mathbf{F_i}}{m_i} \quad (2.2)$$

where t is time, m_i is the mass of atom i, $\mathbf{r_i}$ is its position vector, and $\mathbf{F_i}$ is the total force vector acting on the atom.

The force on a certain atom writes by using Taylor's expansion about the equilibrium positions,

$$F_i^\alpha = -\sum_{j,\beta} \Phi_{ij}^{\alpha\beta} u_j^\beta - \frac{1}{2!} \sum_{jk,\beta\gamma} \Psi_{ijk}^{\alpha\beta\gamma} u_j^\beta u_k^\gamma + \ldots \,, \quad (2.3)$$

where F_i^α is the total force applied on atom i in the α direction due to the atom displacements u. $i, j, k \in 1, ..., N$ represent atom indices and $\alpha, \beta, \gamma \in x, y, z$ refer to the Cartesian components.

$\Phi_{ij}^{\alpha\beta}$ is the harmonic (second-order) force constant involving the atom pair i, j and $\Psi_{ijk}^{\alpha\beta\gamma}$ is the third-order force constant involving atom triplets i, j, k and write

$$\Phi_{ij}^{\alpha\beta} = \left. \frac{\partial \mathrm{U}}{\partial u_i^\alpha \partial u_j^\beta} \right|_{\mathbf{r}_{i,j}=\mathbf{r}_{i,j}^0} \quad (2.4)$$

and

$$\Psi_{ijk}^{\alpha\beta\gamma} = \left. \frac{\partial \mathrm{U}}{\partial u_i^\alpha \partial u_j^\beta \partial u_k^\gamma} \right|_{\mathbf{r}_{i,j,k}=\mathbf{r}_{i,j,k}^0} \quad (2.5)$$

The harmonic (second-order) force constants $\Phi_{ij}^{\alpha\beta}$ determine the normal vibrational modes (eigenmodes) of the lattice and the related properties such as the phonon group velocities and density of states. The anharmonic (third-order and higher orders) force constants $\Psi_{ijk\ldots}^{\alpha\beta\gamma\ldots}$ representing the anharmonicity of

the lattice are important in the related Umklapp phonon scattering processes and determine the anharmonic phonon relaxation time.

In the current thesis, these force constants have been obtained either from the empirical potential energy using its analytical form, or from *ab initio* calculations by solving the Schrödinger equations with density-functional theory (DFT).

In a perfect insulating crystal, harmonic phonons would never be scattered and thus the phonon mean free path Λ would always be equal to the crystal size. Under the single-mode-relaxation time approximation, the thermal conductivity is defined by $\kappa = \frac{1}{3}\sum_{\mathbf{q}} C_{\mathbf{q}} v_{\mathbf{q}} \Lambda_{\mathbf{q}}$ for a 3D crystal where $C_{\mathbf{q}}$, $v_{\mathbf{q}}$ and $\Lambda_{\mathbf{q}}$ refer to the specific heat per volume unit, the group velocity and the mean free path of the phonon mode $\mathbf{q}$. Such a crystal would have anomalous, diverging with the crystal size, thermal conductivity at all temperatures. Scattering of phonons by lattice imperfections, e.g., by isotopic impurities, in a one-dimensional (1D) crystal also does not result in the normal, converging with the crystal length, thermal conductivity [Casher and Lebowitz (1971a); Rubin and Greer (1971a)]. Only anharmonic phonon-phonon interactions and scattering can result in the normal heat transport in low-dimensional crystals.

2.1.2 Limitation

Classical MD simulations technique has two intrinsic drawbacks:

- It is based upon empirical interatomic potentials and thus are less accurate than quantum-mechanical approaches, e.g. *ab initio* MD (AIMD) simulations.
- It is based on classical statistics and hence valid only in the classical limit of phonon distribution, i.e., for temperatures higher than the Debye temperature of the materials.

In AIMD simulations, the atomic interactions are described by first-principles formulations, where the electron exchange and correlation Hamiltonian is usually introduced into density-functional theory. However, the abrupt change in the electron density at surfaces of the system can result in deviation of surface/adsorbate bond strengths [Schimka et al. (2010)]. AIMD is highly demanding on computational ability and the runs are limited to the simulation of small systems (a few hundred atoms) and for short time intervals (a few nanoseconds). The limited system size is not able to represent phonons of long wavelengths. Such simulation time is far from sufficient for the low frequency phonons to relax and also prevent efficient ensemble averages. Despite their individual limitations, AIMD and classical MD simulations can be used in parallel to provide complementary information. When AIMD and classical

MD results are consistent, it is reasonable to assume that the agreement is not accidental, and that the theoretical predictions are realistic representations of actual physical phenomena.

In the high temperature limit $\hbar\omega_\Theta \ll k_\mathrm{B}T$, where ω_Θ is the Debye frequency of the solid $\omega_\Theta = k_\mathrm{B}T_\Theta/\hbar$, T refers to the mean temperature of the system, k_B and $\hbar$ represent the Boltzmann and the reduced Planck's constants, respectively, the phonon statistics reduce from the Bose-Einstein distribution

$$n_\mathrm{BE} = \frac{1}{\mathrm{e}^{\frac{\hbar\omega}{k_\mathrm{B}T}} - 1}, \tag{2.6}$$

to

$$n = \frac{k_\mathrm{B}T}{\hbar\omega},$$

thus all the phonon mode have the same energy $\hbar\omega \times n$, independent of the frequency. This means that all phonons modes are equally excited. Therefore, when the system has a temperature equal to or lower than the Debye temperature of the crystal, a MD simulation with classical thermostats

- overestimates the heat capacity
- brings in extra phonon-phonon scattering

This is the case when classical MD is used to simulate carbon nanotubes and graphene at room temperature since the Debye temperatures of these materials are between 1200 and 2000 K.

2.2 Phonon transmission coefficient

The detailed behaviour of phonons in the scattering events with defects, boundaries and interfaces is crucial to understand and predict the phonon transport at the nanoscale, when the phonon MFP is comparable to the characteristic size of the scatterers. A key quantity in this concern is the phonon transmission coefficient or probability.

In terms of phonon interface scattering, the acoustic mismatch model (AMM) and diffuse mismatch model (DMM) are often used for the calculation of phonon transmission [Swartz and Pohl (1989)]. The AMM, assuming a perfect interface, considers long-wavelength phonons and uses the acoustic impedances Z of the two adjacent materials 1 and 2 for the calculation of phonon transmission probability,

$$\alpha_{1,2} = \frac{4Z_1Z_2}{(Z_1 + Z_2)^2} \tag{2.7}$$

Where $Z = \rho v$ is the acoustic impedance, ρ is the mass density and v is the speed of sound, respectively.

Phonon scattering at interfaces is assumed to be completely diffusive in DMM. Hence, the probability of a phonon diffusely scattered across the interface is thus related only to the bulk density of states $g(\omega)$, the phonon group velocity, and the phonon energy on each side of the interface [Duda et al. (2009)],

$$\alpha_{1\to 2} = \frac{\sum_{\mathbf{q}_2} \hbar\omega_{2,\mathbf{q}_2} v_2 g_2(\omega_2) n_{\mathrm{BE}}}{\sum_{\mathbf{q}_1} \hbar\omega_{1,\mathbf{q}_1} v_1 g_1(\omega_1) n_{\mathrm{BE}} + \sum_{\mathbf{q}_2} \hbar\omega_{2,\mathbf{q}_2} v_2 g_2(\omega_2) n_{\mathrm{BE}}}, \tag{2.8}$$

Although AMM and DMM have been used exclusively as inputs for BTE solutions and for explaining experimental data of reduced thermal conductivity in nanostructured materials, neither of them can

- accurately capture the underlying physics of phonon transport across material interfaces. In addition to the differences in the intrinsic bulk properties of the contacting materials such as Z and $g(\omega)$, the atomic-scale interactions at the interface may contribute to the heat transfer in an unexpected manner.
- provide a spectral analysis clarifying the contribution of each phonon mode. The transmission probabilities obtained from AMM and DMM are overall/averaged values.

To address these important deficiencies, several advanced techniques have recently been developed for studying phonon transmission based on the atomistic simulations, including the phonon wave-packet (WP) method based on MD simulations [Schelling et al. (2002a); Schelling et al. (2004)], linear lattice dynamics [Zhao and Freund (2005)], and the atomic Green's function (AGF) approach [Mingo and Yang (2003)]. In the phonon WP method, a WP is initiated in one material and propagates across the interface. Plane wave functions for a well-defined phonon mode $\mathbf{q}$ with a Gaussian envelope are used to assign the initial displacement and velocity of the atoms. The transmission coefficient is calculated by the ratio of the atomic energy (both potential and kinetic) on the two sides of the interface. The simulation domain needs to be long enough in the direction perpendicular to the interface and only one phonon transmission data point corresponding to a specific phonon mode can be obtained in a single run of MD simulation. So this process is costly for obtaining the phonon transmission for all phonon modes with a desirable spectral resolution. Linear lattice dynamics by solving the lattice dynamical equation under the harmonic approximation for the atoms at the interface, has also been proposed to calculate phonon transmission. The method is restricted to the perfect lattice interfaces. The Green's function approach solves the response of the system under a small perturbation. In the AGF approach, a lattice system is divided into sub-systems. The Green's function of the decoupled sub-systems is ob-

tained first and the Green's function of the coupled system is then calculated by linking the Green's function of the decoupled sub-systems.

Before presenting the technical details of the phonon WP and Green's function method, it is important to clarify the definition of transmission coefficient/probability $\alpha(\omega_{\mathbf{q}})$, transmission function $\Xi(\omega)$ and their relation with the density of states $g(\omega)$ in the thermal conductance using the Landauer formalism. The scattering theory treats a system by dividing it into three coupled subsystems: two semi-infinite leads connected through the scattering region. The heat flux flowing from the hot lead to the cold lead in a 3D system writes

$$J = \int_{BZ} \hbar\omega_{\mathbf{q}} v^z_{g,\mathbf{q}} (n_L - n_R) \alpha_{\mathbf{q}} \frac{\mathrm{d}^3\mathbf{k}}{(2\pi)^3}, \tag{2.9}$$

where $\hbar\omega_{\mathbf{q}}$ is the energy quantum of the phonon mode $\mathbf{q}$ which is defined by the wave vector and the frequency $(\mathbf{k}, \omega)$ of the leads' normal modes, $v^z_{g,\mathbf{q}}$ is the phonon group velocity of the phonon mode $\mathbf{q}$ projected on the direction of the heat flow, $n_{L,R}$ is the phonon number on the left and right reservoir following the Bose-Einstein distribution $n_{L,R} = \left(\mathrm{e}^{\frac{\hbar\omega}{k_\mathrm{B} T_{L,R}}} - 1 \right)^{-1}$, $\alpha_{\mathbf{q}}$ is the normalized transmission probability of the phonon mode $\mathbf{q}$ and $\alpha_{\mathbf{q}} \in [\ 0, 1\ ]$. The integration goes through all the phonon modes in the irreducible Brillouin Zone (BZ).

In the linear regime, the phonon population undergoes small perturbations and the population difference can be Taylor expanded with respect to the average temperature,

$$n_L - n_R = \left. \frac{\partial n}{\partial T} \right|_{T_0 = (T_L + T_R)/2} (T_L - T_R),$$

Thus the thermal conductance writes

$$G = J/\Delta T = \int_{BZ} \hbar\omega_{\mathbf{q}} v^z_{g,\mathbf{q}} \left. \frac{\partial n}{\partial T} \right|_{T_0} \alpha(\omega_{\mathbf{q}}) \frac{\mathrm{d}^3\mathbf{k}}{(2\pi)^3}, \tag{2.10}$$

We note that $\mathrm{d}^3\mathbf{k} = \mathrm{d}k_x \mathrm{d}k_y \mathrm{d}k_z$ and $v^z_{g,\mathbf{q}} \mathrm{d}k_z = \partial\omega/\partial k_z \mathrm{d}k_z = \mathrm{d}\omega$. The Eq. (2.10) reduces to

$$G = J/\Delta T = \int_{BZ} \hbar\omega \ \left. \frac{\partial}{\partial T} \left(e^{\frac{\hbar\omega}{k_B T}} - 1 \right)^{-1} \right|_{T_0} [\alpha(\omega_{\mathbf{q}}) \mathrm{d}k_x \mathrm{d}k_y] \frac{\mathrm{d}\omega}{(2\pi)^3}, \tag{2.11}$$

Hence we identify the spectral phonon transmission function $\Xi(\omega) = \alpha(\omega_{\mathbf{q}}) g(\omega)$ where $g(\omega) = \mathrm{d}k_x \mathrm{d}k_y$ is the projected phonon density of states in the non-periodic directions of the system.

2.2.1 Phonon wave-packet technique

To probe the phonon transmission coefficient, MD with the phonon wave packet method has been used to provide the per-phonon-mode energy transmission coefficient $\alpha(\omega, l)$ [Schelling et al. (2002a); Schelling et al. (2004)]. This method has been limited to effective 1D systems since all the atoms obey the same atomic movement patterns in the plane normal to the wave vector.

In the present thesis, I extend this 1D method by exciting a realistic 3D Gaussian wave packet centered at the frequency ω and wave vector $\vec{k}$ in the reciprocal space and at $\vec{r}_0$ in the real space, with the spatial width (coherence length) $l_{\shortparallel}$ in the direction of $\vec{k}$. The spatial extent $l_{\perp}$ in the perpendicular directions to $\vec{k}$ can be different from that in the parallel direction. A 3D phonon WP has the displacement $\vec{u}_i$ for the atom i as:

$$\vec{u}_i = A\vec{e}_i(\vec{k}) \exp\left(\mathrm{i}\left[\vec{k}\cdot(\vec{r}_i - \vec{r}_0) - \omega t\right]\right) \exp\left(-\frac{|\vec{r}_i - \vec{r}_0 - \vec{v}_g t|^2}{4l^2}\right), \quad (2.12)$$

where A is the wave packet amplitude, $\vec{e}_i(\vec{k})$ is the eigenvector of the phonon mode $\mathbf{q} = (\omega, \vec{k})$, ω is the eigenfrequency for the wave vector $\vec{k}$ within a single branch of the phonon dispersion curve, $\vec{v}_g$ is the phonon group velocity along the wave vector $\vec{k}$ at the wave packet center frequency ω. Wave amplitude A of the generated phonon wave packets was taken sufficiently small such that the anharmonic coupling to other lattice modes is kept weak [Schelling et al. (2002a)]. Hence the wave packets propagate in an effective harmonic crystal without any perceptible spreading or scattering.

In Eq. (2.12), the coherence length in the direction parallel to the wave vector $l_{\shortparallel}$ is set to be equal to that in the perpendicular direction $l_{\perp}$, $l_{\shortparallel} = l_{\perp} = l$. A more general expression that independently controls the coherence lengths in different directions writes,

$$\vec{u}_i = A\vec{e}_i(\vec{k}) \exp\left(\mathrm{i}\left[\vec{k}\cdot(\vec{r}_i - \vec{r}_0) - \omega t\right]\right) \cdot \quad (2.13)$$

$$\exp\left(-\frac{(r_{i,\shortparallel} - r_{0,\shortparallel} - v_{g,\shortparallel} t)^2}{4l_{\shortparallel}^2}\right) \exp\left(-\frac{(r_{i,\perp} - r_{0,\perp} - v_{g,\perp} t)^2}{4l_{\perp}^2}\right), \quad (2.14)$$

It's evident that $v_{g,\perp} = 0$ if the wave packet does not collapse.

Practically, a WP is generated by assigning the atomic displacement following Eq. (2.12) and velocities by taking the time derivative at the initial state $t = 0$. The wave packet was set to propagate normally to the defect layer, where an elastic scattering results in transmitted and reflected waves. The

wave packet energy transmission coefficient $\alpha(\omega, l)$ is defined as the ratio between the energy carried by the transmitted and initial wave packets, centered at the given phonon mode $(\omega, \vec{k})$ with the spatial extent l. The plane-wave limit is reproduced by the wave packets with the spatial width l much larger than the wavelength λ_c of the wave packet central frequency.

A typical example of a phonon wave packet scattered at an internal interface is shown in Fig. 2.1. The system is bulk silicon modeled by Stillinger-Weber potential [Stillinger and Weber (1985a)]. A longitudinal acoustic phonon WP is generated by following the form in Eq. (2.12) and corresponds to the wave vector $\mathbf{k} = \frac{5}{20}\langle 001\rangle$ and the frequency $\omega = 5.1128$ THz. The corresponding central wavelength is $\lambda_c = 1.56$ nm and the coherence length is $l = 20$ nm. Since $l \gg \lambda_c$, no significant back scattering of the wave packet is observed in this case, where as a phonon WP of $l = 5nm$, as depicted in Fig. 2.2, experience perceptible back-scattering.

2.2.2 Green's function and phonon Green's Function

I. Generality

Phonon Green's function or atomistic Green's function is extended from the Green's function formalism for electron transport. The Green's function of a quantum-mechanical system corresponds to the wave-function of the same system slightly perturbed by a point source.

By definition, one compares the Green's Function (GF) $\mathbf{g}$ with wave functions $|\psi\rangle$ for a system with Hamiltonian $\mathbf{H}$ and energy E,

$$(E - \mathbf{H})|\psi\rangle = 0 \tag{2.15a}$$
$$(E - \mathbf{H})\mathbf{g} = \mathbf{I} \tag{2.15b}$$

The wave function satisfies the Schrödinger equation (2.15a) and the Green's Function $\mathbf{g}$ satisfies Eq. (2.15b), and they are very similar in the form. In fact, the wave function and the Green's Function are closely related, we will clarify this in the following sections.
In a different form, Eq. (2.15) writes

$$E|\psi\rangle = \mathbf{H}|\psi\rangle \tag{2.16a}$$
$$E\mathbf{g} - \mathbf{I} = \mathbf{H}\mathbf{g} \tag{2.16b}$$

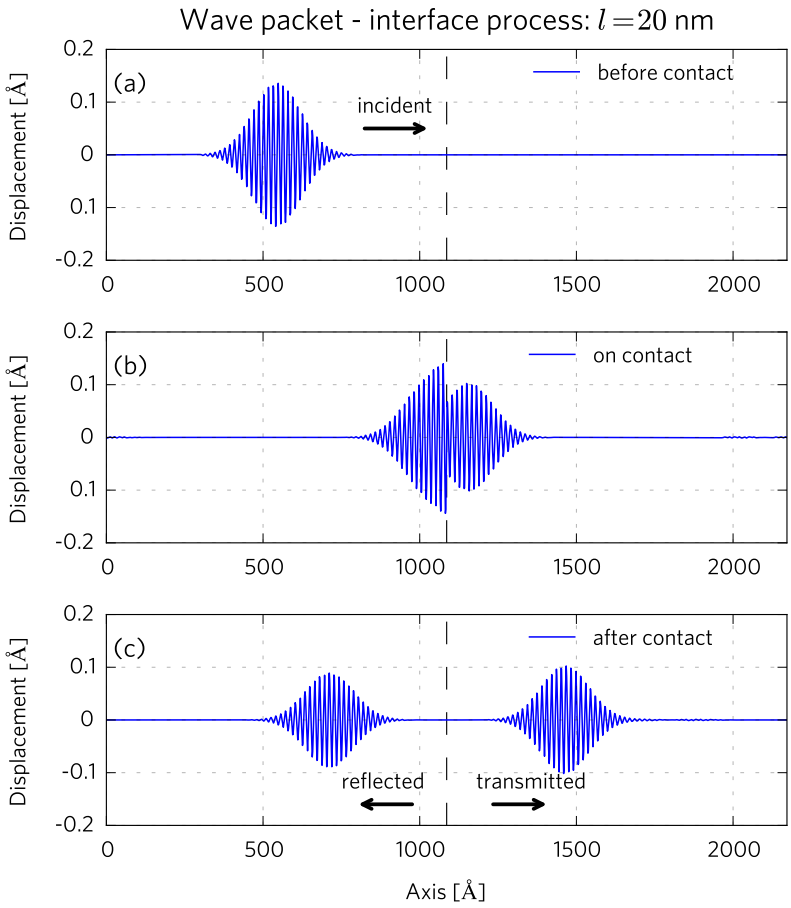

Figure 2.1: *Elastic scattering of a phonon wave-packet at an internal* $\langle 001 \rangle$ *interface of bulk Stillinger-Weber silicon. A longitudinal acoustic phonon WP is generated by following the form in Eq. (2.12) and corresponds to the wave vector* $\boldsymbol{k} = \frac{5}{20}\langle 001 \rangle$ *and the frequency* $\omega = 5.1128$ *THz. The corresponding central wavelength is* $\lambda_c = 1.56$ *nm and the coherence length is* $l = 20$ *nm.*

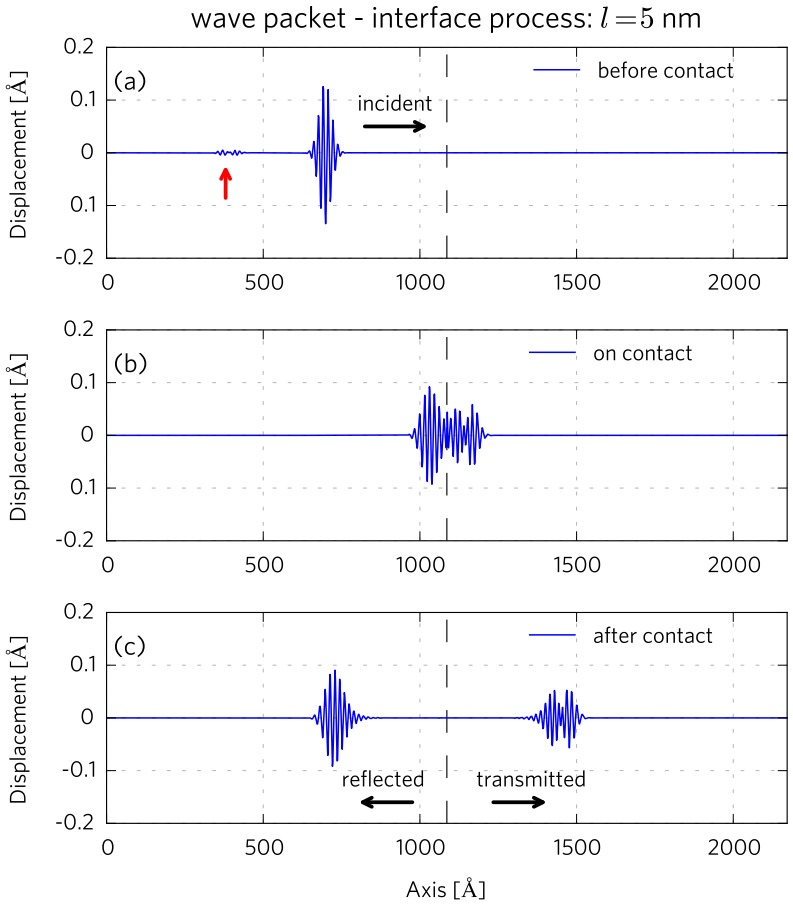

Figure 2.2: *Elastic scattering of a phonon wave-packet at an internal interface of bulk Stillinger-Weber silicon. The wave-packet corresponds to the same phonon mode as in Fig. 2.1 except that the coherence length is much shorter, $l = 5$ nm. The red arrow denotes the back scattering of the WP.*

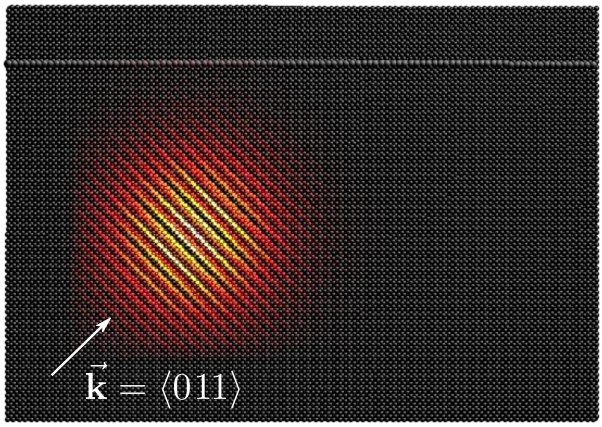

Figure 2.3: *Oblique phonon wave-packet of the same mode as in Fig. 2.1 in the* $\langle 011 \rangle$ *direction.*

One rewrites Eq. (2.16b) in the matrix representation writes

$$\begin{pmatrix} \epsilon_0, & -\gamma, & & \cdots & \\ & \ddots & & & \\ \cdots & -\gamma, & \epsilon_0, & -\gamma, & \cdots \\ & & & \ddots & \\ & \cdots & & -\gamma, & \epsilon_0 \end{pmatrix} \begin{pmatrix} \mathrm{g}_{11} & \mathrm{g}_{12} & \cdots & \mathrm{g}_{1l} & \cdots \\ \mathrm{g}_{21} & \mathrm{g}_{22} & \cdots & \mathrm{g}_{2l} & \cdots \\ \vdots & \vdots & & \vdots & \\ \mathrm{g}_{\mathrm{j}1} & \mathrm{g}_{\mathrm{j}2} & \cdots & \mathrm{g}_{jl} & \cdots \\ \vdots & \vdots & & \vdots & \end{pmatrix} = E\mathbf{g} - \mathbf{I}$$

The l^{th} column of $\mathbf{g}$ is $|\phi\rangle = (\mathrm{g}_{1l}, \mathrm{g}_{2l}, \cdots, \mathrm{g}_{jl}, \cdots)^T$. Therefore, in the index representation, Eq. (2.15) rewrites as

$$\epsilon_0 \psi_j - \gamma \psi_{j+1} - \gamma \psi_{j-1} = E\psi_j, \tag{2.17a}$$

$$\epsilon_0 \mathrm{g}_{jl} - \gamma \mathrm{g}_{j+1,l} - \gamma \mathrm{g}_{j-1,l} = E\mathrm{g}_{jl} - \delta_{jl} \tag{2.17b}$$

where δ_{jl} is the Kronecker delta.

Theorem I. The sum of any Green's Function $|\phi\rangle$ and an eigenstate $|\psi\rangle$ is also a Green's Function .

Suppose $|f\rangle = |\phi\rangle + |\psi\rangle$, one has

$$\begin{aligned} \mathbf{H}|f\rangle &= \mathbf{H}|\phi\rangle + \mathbf{H}|\psi\rangle = E|\phi\rangle - \mathbf{I}_l + E|\psi\rangle \\ &= E|f\rangle - \mathbf{I}_l \end{aligned}$$

where $\mathbf{I}_l$ is a vector with its l^{th} element equates unity and other elements zero. Hence by definition of Eq. (2.17b), $|f\rangle$ is also a Green's Function .

Accrording to Theorem. I, the general form of a Green's Function writes

$$f_j = \mathrm{g}_{jl} + \psi_j \tag{2.18}$$

with $\psi_j = A\mathrm{e}^{ikj} + B\mathrm{e}^{-ikj}$ and ψ_j is any eigenstate that satisfies the Schrödinger equation.

In a 1D chain, one defines the general Green's Function as,

$$\mathrm{g}_{jl} = \begin{cases} A\mathrm{e}^{ikj} + B\mathrm{e}^{-ikj} & \text{for } j \leq l \\ C\mathrm{e}^{ikj} + D\mathrm{e}^{-ikj} & \text{for } j \geq l \end{cases} \tag{2.19}$$

Given $A = 0, D = 0$, Eq. (2.19) rewrites as

$$\mathrm{g}_{jl} = \begin{cases} B\mathrm{e}^{-ikj} & \text{for } j \leq l \\ D\mathrm{e}^{-ikj} & \text{for } j \geq l \end{cases}$$

At $j = l$, one has $B\mathrm{e}^{-ikl} = D\mathrm{e}^{-ikl}$, one can choose

$$B = A\mathrm{e}^{ikl}$$
$$C = A\mathrm{e}^{-ikl}$$

One arrives at

$$\mathrm{g}_{jl} = \begin{cases} A\mathrm{e}^{-ik(j-l)} & \text{for } j \leq l \\ A\mathrm{e}^{ik(j-l)} & \text{for } j \geq l \end{cases}$$

At $j = l$, one has

$$\epsilon_0 \mathrm{g}_{ll} - \gamma \mathrm{g}_{l+1,l} - \gamma \mathrm{g}_{l-1,l} = E\mathrm{g}_{ll} - 1 \tag{2.21}$$

given $E = \epsilon_0 - 2\gamma \cos k$, one obtains

$$A = \frac{1}{i2\gamma \sin k}$$

therefore, the Green's Function for an infinite 1D system writes

$$\mathrm{g}_{jl} = \frac{\mathrm{e}^{ik|j-l|}}{i\hbar v} \tag{2.22}$$

where $\hbar v = \mathrm{d}E/\mathrm{d}k = 2\gamma \sin k$.

One reminds the definition of the Green's Function given in Eq. (2.17b),

$$\epsilon_0 \mathrm{g}_{jl} - \gamma \mathrm{g}_{j+1,l} - \gamma \mathrm{g}_{j-1,l} = E\mathrm{g}_{jl} - \delta_{jl}$$

which means that the Green's Function satisfies the Schrödinger equation of an infinite chain for $j \neq l$,

$$\epsilon_0 \mathrm{g}_{jl} - \gamma \mathrm{g}_{j+1,l} - \gamma \mathrm{g}_{j-1,l} = E\mathrm{g}_{jl}$$

whereas at $j = l$, Green's Function satisfies Eq. (2.21)

$$\epsilon_0 g_{ll} - \gamma g_{l+1,l} - \gamma g_{l-1,l} = E g_{ll} - 1$$

Suppose a wave function $|\phi_1\rangle$ satisfies $\alpha|\phi_1\rangle = -1$, thus the Green's Function can be considered as the eigenstates that satisfy the Schrödinger equation below,

$$\begin{aligned} \epsilon_0|\psi_j\rangle - \gamma|\psi_{j-1}\rangle - \gamma|\psi_{j+1}\rangle &= E|\psi_j\rangle \\ \epsilon_0|\psi_l\rangle - \gamma|\psi_{l-1}\rangle - \gamma|\psi_{l+1}\rangle - \alpha|\phi_1\rangle &= E|\psi_l\rangle \end{aligned}$$

This Schrödinger equation describes a "T-shaped" infinite chain: an infinite system whose site l is connected to a side chain with a coupling constant α. The Green's Function g_{jl} of an infinite system is exactly the eigenstate ψ_j of the "T-shaped" system with a side chain at site l. Physically, the Green's Function is the response (wave) function of the "T-shaped" chain with an incoming (plane wave) excitation along the side chain. The transmitted wave to the section $j > l$ is $\psi_j = g_{jl} = \frac{e^{ik(j-l)}}{i\hbar v}$ which corresponds to a plane wave propagating towards the "+" direction, and the other transmitted wave to the other half section $j < l$ is $\psi_j = g_{jl} = \frac{e^{-ik(j-l)}}{i\hbar v}$ which corresponds to a plane wave propagating towards the "-" direction.

II. Phonon Green's function

A system of coupled harmonic oscillators is divided into three regions: two thermal reservoirs and a scattering region. Under the harmonic approximation, the phonon waves in the system are described by the dynamical equation, similar to a tight-binding system described by Eq. (2.15a)

$$(\omega^2 \mathbf{I} - \mathbf{H})\Psi = 0, \tag{2.23}$$

where ω is the angular phonon frequency, $\mathbf{I}$ is the identity matrix, $\mathbf{H}$ is the harmonic matrix or the Hamiltonian and Ψ is the magnitude of the vibrational normal modes. The elements of $\mathbf{H}$ are the second-order (harmonic) force constants in Eq. (2.4) normalized by the atomic masses,

$$H_{3i+\alpha,3j+\beta} = \frac{1}{\sqrt{m_i m_j}} \Phi_{ij}^{\alpha\beta}, \tag{2.24}$$

The harmonic matrix $\mathbf{H}$ can be divided into submatrices corresponding to different couplings,

$$\mathbf{H} = \begin{pmatrix} \mathbf{K}_L & \mathbf{V}_{LC} & 0 \\ \mathbf{V}_{CL} & \mathbf{K}_C & \mathbf{V}_{CR} \\ 0 & \mathbf{V}_{RC} & \mathbf{K}_R \end{pmatrix} \tag{2.25}$$

where $\mathbf{K}_L, \mathbf{K}_R$ and $\mathbf{K}_C$ are the Hamiltonians of the left (L), right (R) leads and the central (C) scattering region, respectively. $\mathbf{V}_{CL}$ and $\mathbf{V}_{CR}$ describe the coupling between the scattering region with the left and right leads, respectively. It is evident that symmetries below are valid, $\mathbf{K}_{L,R,C} = (\mathbf{K}_{L,R,C})^\dagger$ and $\mathbf{V}_{CL,CR} = (\mathbf{V}_{LC,RC})^\dagger$, where "†" denotes the complex conjugate. The lower left and upper right corners of $\mathbf{H}$ are zero because there is no direct coupling between the leads.

The Green's Function $\mathbf{G}$ of the system writes, similar to Eq. (2.15b),

$$(\omega^2\mathbf{I} - \mathbf{H})\mathbf{G} = \mathbf{I}, \tag{2.26}$$

where $\mathbf{G}$ can also be divided into submatrices,

$$\mathbf{G} = \begin{pmatrix} \mathbf{G}_L & \mathbf{G}_{LC} & 0 \\ \mathbf{G}_{CL} & \mathbf{G}_C & \mathbf{G}_{CR} \\ 0 & \mathbf{G}_{RC} & \mathbf{G}_R \end{pmatrix} \tag{2.27}$$

By developing Eq. (2.26) with Eq. (2.27), the Green's Function of the scattering region can be solved as,

$$G_s = \left[\omega^2 I - K_C - \Sigma_L - \Sigma_R\right]^{-1}, \tag{2.28}$$

where $\Sigma_L = \mathbf{V}_{CL}\mathbf{g}_L\mathbf{V}_{CL}^\dagger$, $\Sigma_R = \mathbf{V}_{CR}\mathbf{g}_R\mathbf{V}_{CR}^\dagger$ are the self-energies of the left and right leads, which describe the perturbation of the scattering region when connected to the leads. $\mathbf{g}_L$ and $\mathbf{g}_R$ refer to the surface Green's functions of the unperturbed left and the right leads,

Heat current from the right lead to the scattering region writes,

$$J(\omega) = \frac{\hbar}{2}\mathrm{Tr}\left(\Psi_R^\dagger \mathbf{K}_{RC}\Psi_C - \Psi_C^\dagger \mathbf{K}_{CR}\Psi_R\right) \tag{2.29}$$

By taking the Lippmann-Schwinger equation, the heat current per phonon mode writes,

$$J(\omega) = \frac{\hbar}{4\pi}\mathrm{Tr}\left[\Gamma_L \mathbf{G}_C \Gamma_R G_s^\dagger\right] \tag{2.30}$$

where $\Gamma_L = i(\Sigma_L - \Sigma_L^\dagger)$ and $\Gamma_R = i(\Sigma_R - \Sigma_R^\dagger)$.

Thus the phonon transmission function $\Xi(\omega)$ writes,

$$\Xi(\omega) = \mathrm{Tr}\left[\Gamma_L \mathbf{G}_C \Gamma_R G_s^\dagger\right] \tag{2.31}$$

2.3 Interface thermal conductance

Phonon wave-packet technique based on MD and atomistic Green's Function allows us to precisely determine the key quantity that characterizes the phonon transport and scattering across an interface: the phonon transmission coefficient $\alpha_{\mathbf{q}}$ and transmission function $\Xi(\omega)$. The interface thermal conductance can thereby be determined by following the Landauer's formalism for phonon-wave scattering as an analogy to electron-wave scattering. Apart from the Landauer's formalism that treats phonons as coherent waves, other approaches can be used to determine the interface thermal conductance. Two major approaches are commonly used: a direct non-equilibrium MD method by fitting the Fourier's law and an indirect equilibrium MD method by using the fluctuation-dissipation theorem.

2.3.1 Landauer's formalism

The determination of thermal conductance by Landauer's formalism was already presented in Section. 2.2. For a system with transverse confinement perpendicular to the transport direction, the thermal conductance is reformulated from Eq. (2.11) as,

$$G = \int_{BZ} \hbar\omega \ \frac{\partial}{\partial T}\left(e^{\frac{\hbar\omega}{k_B T}} - 1\right)^{-1}\Bigg|_{T_0} \Xi(\omega)\frac{\mathrm{d}\omega}{(2\pi)^3}, \tag{2.32}$$

where the phonon transmission function $\Xi(\omega) = \alpha(\omega)\mathrm{d}k_x\mathrm{d}k_y$ can be rewriten as,

$$\Xi(\omega) = \alpha(\omega)\mathcal{M}(\omega), \tag{2.33}$$

$\mathcal{M}(\omega)$ is an integer number that refers to the number of open phonon channels in the thermal reservoir and it is an intrinsic property of the reservoir and does not depend on the scattering region. $\mathcal{M}(\omega)$ can be calculated by counting the number of phonon bands at frequency ω in the phonon dispersion relation from lattice dynamics. The elastic scattering of the phonon wave is characterized by the transmission probability $\alpha(\omega)$.

An example of the number of open channels in a nanosystem is shown in Fig. 2.4. The system is a pristine silicon nanowire with a cross section of 21.72 $\times$ 21.72 nm^2 along $\langle 001 \rangle$ crystallographic direction. Since no scatterer is present in the nanowire, the transmission function $\Xi(\omega)$ displays a clear stepwise structure that gives the number of phonon channels, i.e. $\Xi(\omega) = \mathcal{M}(\omega)$ since $\alpha = 1$. In the low-energy region below 1.04 THz, being the energy gap of the lowest optical modes, the transmission function $\Xi = 4$, indicating the number of acoustic branches corresponding to longitudinal, twisting, and doubly degenerated flexural modes and reflecting the perfect transmission for all acoustic modes.

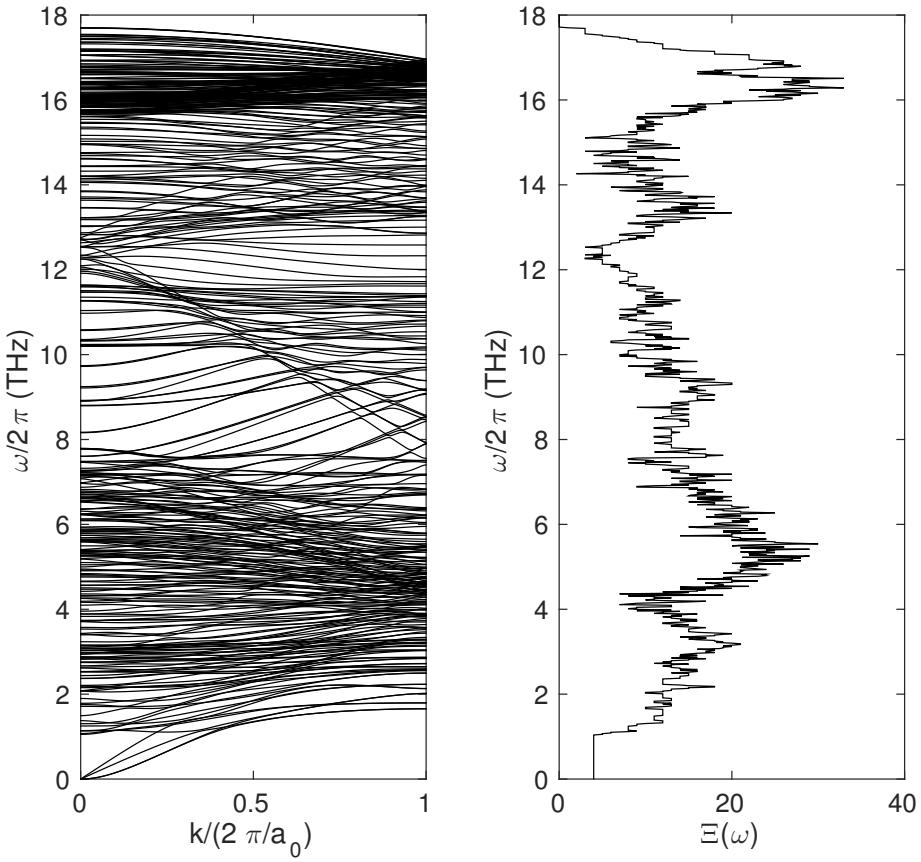

(a) Phonon dispersion ω-k

(b) Transmission function $\Xi(\omega)$

Figure 2.4: *Phonon dispersion relation and transmission function $\Xi(\omega)$ along the axial direction of a $\langle 001 \rangle$ Stillinger-Weber silicon nanowire with a cross section of 21.72×21.72 nm^2.*

2.3.2 Molecular dynamics

I. Steady-state non-equilibrium MD

Steady-state non-equilibrium MD is largely used to predict the interface thermal resistance/conductance. A 1D temperature gradient is imposed across the interface and the resulting heat flux is measured. Or the other way round, a constant heat flux is imposed and the resulting temperature gradient is measured at steady-state. The interface thermal conductance G can be obtained according to the Fourier's law,

$$\mathbf{J} = G\Delta T \tag{2.34}$$

where $\mathbf{J}$ is the steady-state heat flux in W m^{-2} and G is in W m^{-2} K^{-1}, which is defined as the amount of thermal energy transfer rate per unit area perpendicular to the direction of the heat flux and ΔT is the temperature difference at the interface. The thermal contact resistance is the inverse of conductance.

NEMD approach requires fitting the temperature profile at the interface and determines directly the thermal conductance through the Fourier's law. That's why it is also called a "direct method". In spite of its technical simplicity, one should be careful using it because artifacts can be introduced easily due to

- multiple reflections of ballistic phonons between the thermal reservoirs. If the distance between the reservoirs are not long enough that the phonons are not sufficiently scattered over their trajectories, multiple reflections of ballistic phonons could lead to unphysical phonon transmission.
- improper parameters in setting up the reservoirs. Constant rescaling of the atomic velocities in the thermostats introduces artificial scattering and performance can depend on the characteristic time of the thermostats as a critical parameter.
- erroneous definition of temperature. Temperature profile needs to be established in order to get the temperature drop at the interface ΔT whereas it is hard to define the temperature of a small number of atoms from the thermodynamic point of view.

II. Equilibrium MD

To avoid the disadvantages of NEMD method, EMD recovers the intrisic fluctuations of the system within the microcanonical ensemble without introducing perturbations.

For a system at thermal equilibrium, the system temperature fluctuates around its average equilibrium value. According to energy conservation and the linear response theory, the thermal resistance R between two interacting subsystems at the two sides of the interface with a temperature difference ΔT could be

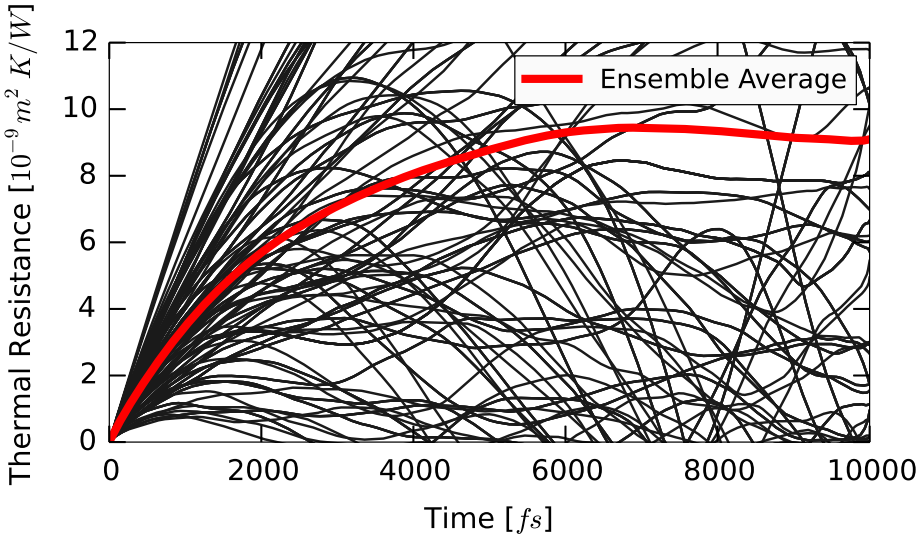

Figure 2.5: *Thermal resistance proportional to the time integrals of the normalized autocorrelation functions of the temperature difference from Eq. (2.35). The black curves are from different trajectories and the red curve is the ensemble average.*

calculated by the following equation [Rajabpour and Volz (2010)]:

$$Rk_B = \int_0^\infty \frac{\langle \Delta T(0) \Delta T(t) \rangle}{\langle \Delta T(0)^2 \rangle} dt \left(\frac{1}{N_1} + \frac{1}{N_2} \right), \tag{2.35}$$

where k_B is the Boltzmann constant, N_1 and N_2 refer to the number of degrees of freedom of the two subsystems. The time integral of the normalized temperature-difference autocorrelation corresponds to the relaxation time required by the total decay of the temperature jump across the interface,

$$\tau = \int_0^\infty \frac{\langle \Delta T(0) \Delta T(t) \rangle}{\langle \Delta T(0)^2 \rangle} dt.$$

A typical process to obtain the thermal resistance by following such approach is to first equilibrate the system in the canonical ensemble with thermostats and barostats, then put the system into the microcanonical ensemble to reach ergodicity and finally record the temperature fluctuations of the subsystems. The final thermal resistance needs a number of different trajectories to converge. Fig. 2.5 shows the ensemble average of the autocorrelation functions and finally converges to a plateau.

2.4 Lattice thermal conductivity

Under the single-mode-relaxation-time approximation via kinetic theory, the thermal conductivity κ of a 3D lattice is given by,

$$\kappa = \frac{1}{3}\sum_{\mathbf{q}} C_{\mathbf{q}} v_{\mathbf{q}}^2 \tau_{\mathbf{q}}, \tag{2.36}$$

where $C_{\mathbf{q}}$ and $v_{\mathbf{q}}$ are the specific heat per volume unit and the group velocity of the $\mathbf{q}$-th phonon mode. The phonon RT τ measures the temporal response of a perturbed phonon mode to relax back to equilibrium due to the net effect of different phonon scattering mechanisms. The specific heat indicates how much energy a certain mode $\mathbf{q}$ carries, the group velocity indicates how fast phonons of the mode propagate, and the lifetime (mean free path) indicates how long (far) phonons of the mode $\mathbf{q}$ travel on average before being scattered. τ can be defined as [Ziman (1960)]

$$\frac{\partial n}{\partial \tau} = \frac{n - n_0}{\tau}, \tag{2.37}$$

where n and n_0 are the phonon occupation numbers out of and at thermal equilibrium. The phonon mean free path (MFP) $\Lambda_{\mathbf{q}}$ is defined as $\Lambda_{\mathbf{q}} = v_{\mathbf{q}}\tau_{\mathbf{q}}$.

Analytical models derived for the phonon dispersion and lifetimes were used in solving the Boltzmann-transport equation (BTE) for predicting thermal conductivity [Klemens (1955); Callaway (1959); Holland (1963)]. The phonon relaxation times were often obtained by fitting the thermal conductivity with the experimental results. The requirement of fitting parameters prevent these models from exploring the underlying physics. Therefore, techniques based on an atomistic description are necessary to predict the thermal properties without taking fitting parameters.

With the harmonic force constants, the phonon eigenmodes (dispersion relation) can be easily obtained and thus the specific heat and group velocity are derived. Nevertheless, the phonon relaxation times require higher-order force constants from empirical interatomic potential or *ab initio* calculations.

In this section, the calculation of the key ingredients, i.e. $v_{\mathbf{q}}$ and $\tau_{\mathbf{q}}$ in the lattice thermal conductivity by using equilibrium MD and anharmonic LD will be discussed.

2.4.1 Phonon group velocity

The group velocity could be obtained from the phonon dispersion $\omega - \mathbf{k}$. In a lattice with periodic potential, the wave function can be expressed as Bloch

waves. In a vibrational system, the wave function Ψ in Eq. (2.23) is also the displacement function $\mathbf{u}$, which writes as the Bloch form,

$$\mathbf{u} = \mathbf{e}_i e^{\mathrm{i}(\omega t - \mathbf{kr})}, \tag{2.38}$$

where $\mathbf{r}$ is the atomic position. Eq. (2.23) then rewrites as,

$$\omega^2 \begin{pmatrix} \mathbf{e}_1 e^{i\mathbf{kr}_1} \\ \mathbf{e}_2 e^{i\mathbf{kr}_2} \\ \vdots \\ \mathbf{e}_n e^{i\mathbf{kr}_n} \\ \vdots \end{pmatrix} = \begin{pmatrix} \Phi_{11} & \Phi_{12} & \dots & \Phi_{1m} & \dots \\ \Phi_{21} & \Phi_{22} & \dots & \Phi_{2m} & \dots \\ \vdots & \vdots & \ddots & \dots & \\ \Phi_{n1} & \Phi_{n2} & \dots & \Phi_{nm} & \dots \\ \vdots & \vdots & \vdots & \vdots & \ddots \end{pmatrix} \begin{pmatrix} \mathbf{e}_1 e^{i\mathbf{kr}_1} \\ \mathbf{e}_0 e^{i\mathbf{kr}_2} \\ \vdots \\ \mathbf{e}_m e^{i\mathbf{kr}_m} \\ \vdots \end{pmatrix}, \tag{2.39}$$

where Φ_{nm} is a matrix of dimension 3×3 when the three degrees of freedom are considered. The n-th element of $\omega^2\mathbf{u}$ writes,

$$\omega^2 \mathbf{e}_n = \sum_m \Phi_{nm} e^{i\mathbf{kr}_{nm}} \mathbf{e}_m, \tag{2.40}$$

where $\mathbf{r}_{nm} = \mathbf{r}_m - \mathbf{r}_n$ that is the phase factor.

The dynamical matrix writes $\mathbf{D}(\mathbf{k}) = \sum_m \Phi_{nm} e^{i\mathbf{kr}_{nm}}$ and therefore Eq. (2.39) rewrites as the eigenvalue problem,

$$\omega^2 \mathbf{e}(\mathbf{q}) = \mathbf{D}(\mathbf{k}) \cdot \mathbf{e}(\mathbf{q}), \tag{2.41}$$

which is the dynamical equation in the reciprocal space. $\mathbf{D}(\mathbf{k})$ is a matrix of dimension 3N $\times$ 3N and $\mathbf{e}(\mathbf{q})$ is the eigenvector of dimension 3N for the phonon mode $\mathbf{q}$. By diagonalizing $\mathbf{D}(\mathbf{k})$, one can obtain the relation between the wave vector $\mathbf{k}$ and the frequencies ω, which is the phonon dispersion relation. From the frequencies, one can calculate mode specific heat capacity by using either Bose-Einstein or Boltzmann statistics and build phonon dispersion curves and the density of states $D(\omega)$,

$$D(\omega) = \sum_{\mathbf{q}} \delta\left(\omega - \omega_{\mathbf{q}}\right), \tag{2.42}$$

The phonon group velocity can thereby be obtained by its definition,

$$\mathbf{v}_g(\mathbf{q}) = \frac{\partial \omega_{\mathbf{q}}}{\partial \mathbf{k}}, \tag{2.43}$$

The components in the α-th Cartesian direction writes,

$$v_{g,\alpha}(\mathbf{q}) = \frac{1}{\omega_{\mathbf{q}}} \left[\mathbf{e}^{\dagger}(\mathbf{q}) \frac{\partial \mathbf{D}(\mathbf{k})}{\partial k_\alpha} \mathbf{e}(\mathbf{q}) \right], \tag{2.44}$$

Eq. (2.43) requires performing a finite difference using closely space separated wave vectors. This technique is simple and concise as only the solution of the eigenvalue problem is needed. The disadvantage is that there is ambiguity when performing the central difference near where two dispersion branches cross. This ambiguity exists because eigenvalue solvers typically do not sort the phonon branches. This difficulty can be overcome by using very small changes in the wave vector when performing the central difference and using the mode shapes to differentiate branches. Care must also be taken near local minima or maxima, where the group velocity is zero. In this sense, Eq. (2.44) is more practical to calculate the group velocity.

2.4.2 Phonon relaxation time

To extract the phonon relaxation time for Umklapp phonon processes, two major technique categories exist: equilibrium MD-based spectral energy density method (SED) [Turney et al. (2009); Thomas et al. (2010)] and anharmonic lattice dynamics (LD)-based third-order Hamiltonian method [Srivastava (1990)].

Equilibrium MD simulation employs empirical interatomic potentials that incorporate full anharmonicity, which reproduces inelastic phonon scatterings of all orders. Whereas the existing theoretical formalism of anharmonic LD for predicting phonon lifetimes only includes three-phonon processes since the cubic force constants are required). Higher-order phonon processes are not included and will become important as temperature is further increased. The anharmonic LD method apply for systems at the temperature lower than the Debye temperature.

I. Equilibrium MD-based spectral energy density method

The phonon liftetime $\tau(\mathbf{q})$ can be evaluated by using the normal mode decomposition technique. In the equilibrium molecular dynamics, the atomic positions and velocities are projected onto the normal (eigen-) mode coordinates of the system. The normal mode coordinates are then used to calculate the normal mode potential and kinetic energies.

The normal mode coordinate $q(\mathbf{k},t)$ writes as a spatial Fourier Transform of the atomic displacements $\mathbf{u}_j(t)$ [Dove (1993)],

$$q(\mathbf{k},t) = \sum_j (m_j/N)^{1/2} e^{\mathbf{i}\mathbf{k}\mathbf{r}_j^0} \mathbf{e}_j(\mathbf{k}) \mathbf{u}_j(t), \tag{2.45}$$

and its time derivative $\dot{q}(\mathbf{k},t)$

$$\dot{q}(\mathbf{k},t) = \sum_j (m_j/N)^{1/2} e^{\mathbf{i}\mathbf{k}\mathbf{r}_j^0} \mathbf{e}_j(\mathbf{k}) \dot{\mathbf{u}}_j(t), \tag{2.46}$$

where j is the atom index, m_j, $\mathbf{r}_j^0$ and $\mathbf{e}_j(\mathbf{k})$ refer to the mass, the equilibrium position and the corresponding eigenvector of the atom j.

The potential and kinetic energies of the normal mode $\mathbf{q}$ are

$$U(\mathbf{q},t) = \frac{1}{2}\omega(\mathbf{k})^2 q^\dagger(\mathbf{k},t)q(\mathbf{k},t), \tag{2.47}$$

and

$$T(\mathbf{q},t) = \frac{1}{2}\dot{q}^\dagger(\mathbf{k},t)\dot{q}(\mathbf{k},t), \tag{2.48}$$

The total energy of the normal mode is

$$E(\mathbf{q},t) = U(\mathbf{k},t) + T(\mathbf{k},t), \tag{2.49}$$

One can demonstrate that

$$\frac{< E(\mathbf{q},t)E(\mathbf{q},0) >}{< E(\mathbf{q},0)^2 >} = e^{-2\Gamma(\mathbf{q})t}, \tag{2.50}$$

where $\Gamma(\mathbf{q})$ is the linewidth, equal to $1/[2\tau(\mathbf{q})]$. Thus, the lifetime can be approximated as

$$\tau(\mathbf{q}) = \int_0^\infty \frac{< E(\mathbf{q},t)E(\mathbf{q},0) >}{< E(\mathbf{q},0)^2 >}, \mathrm{d}t \tag{2.51}$$

The spectral energy density of the mode $\mathbf{q}$ which correponds to a double Fourier Transform of the atomic velocities in Eq. (2.46) to the reciprocal space of frequency and wave vector,

$$E_{\mathrm{SED}}(\mathbf{q} = (\mathbf{k},\omega)) = \left| \int_{-\infty}^{\infty} \dot{q}(\mathbf{k},t)\exp(-i\omega t)\mathrm{d}t \right|^2, \tag{2.52}$$

In an infinite harmonic system, phonons do not scatter. Therefore their $E_{\mathrm{SED}}(\mathbf{q})$ exhibit delta-function type peaks in the vibrational spectrum. In real material systems, phonons scatter and thus have finite lifetime due to the anharmonic interactions, leading to the linewidth broadening and thus giving Lorentzian peak shapes, as shown in Figure 2.6.

The spectral energy density evaluated at the normal modes has the Lorentzian form,

$$E_{\mathrm{SED}}(\mathbf{q}) \propto \frac{\Gamma(\mathbf{q})}{(\omega_{\mathbf{q}} - \omega)^2 + \Gamma(\mathbf{q})^2}, \tag{2.53}$$

The relaxation time can be thereby evaluated.

II. Anharmonic lattice dynamics (LD)-based third-order Hamiltonian method

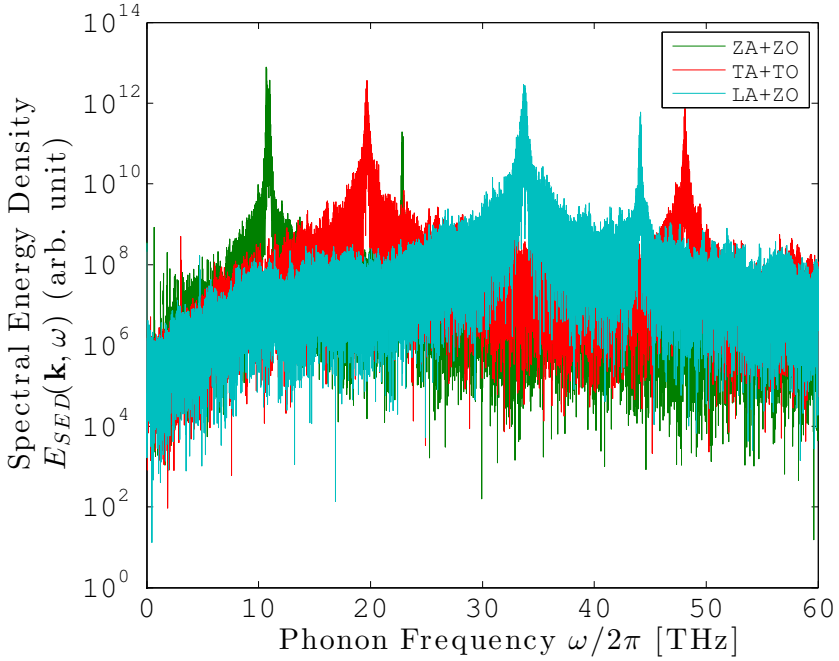

Figure 2.6: *Semilogarithmic plot of the spectral energy density function* $E_{SED}(\boldsymbol{k},\omega)$ *along the* Γ-K *direction with* $\boldsymbol{k} = \frac{4}{5}\frac{2\pi}{a_0}[100]$ *of a supported graphene sheet. Different colors stand for the corresponding phonon branches.*

The lifetime due to phonon-phonon scattering is related to the imaginary part of the phonon self-energy [Debernardi et al. (1995); Wallace (1998); Lindsay et al. (2012)], $1/\tau_{\mathbf{q}} = 2\Gamma_{\mathbf{q}}$ where

$$\begin{aligned}\Gamma_{\mathbf{q}} = \sum_{\mathbf{q}'\mathbf{q}''} \frac{\hbar\pi}{16} \iint_{BZ} \left|\Psi_{\mathbf{q}\mathbf{q}'\mathbf{q}''}\right| \Delta_{\mathbf{q}\mathbf{q}'\mathbf{q}''} \\ \times [(n_{\mathbf{q}'} + n_{\mathbf{q}''} + 1)\delta(\omega_{\mathbf{q}} - \omega_{\mathbf{q}'} - \omega_{\mathbf{q}''}) \\ + 2(n_{\mathbf{q}'} - n_{\mathbf{q}''})\delta(\omega_{\mathbf{q}} - \omega_{\mathbf{q}'} + \omega_{\mathbf{q}''})\mathrm{d}\mathbf{q}'\mathrm{d}\mathbf{q}'']\end{aligned} \tag{2.54}$$

where $\Psi_{\mathbf{q}\mathbf{q}'\mathbf{q}''}$ is the three-phonon matrix. $n_{\mathbf{q}}$ is the equilibrium occupation number for mode $\mathbf{q}$. The delta functions in wave vectors and in frequency ensure the momentum selection rules $\mathbf{k} + \mathbf{k}' = \mathbf{k}'' + \mathbf{G}$ for the fusion processes and the energy conservation $\Delta = \omega_{\mathbf{q}} - \omega_{\mathbf{q}'} \pm \omega_{\mathbf{q}''}$.

The three-phonon matrix $\Psi_{\mathbf{q}\mathbf{q}'\mathbf{q}''}$ is given by

$$\begin{aligned}\Psi_{\mathbf{q}\mathbf{q}'\mathbf{q}''} = \sum_{ijk} \sum_{\alpha\beta\gamma} \frac{\epsilon^{\mathbf{q}}_{i\alpha} \epsilon^{\mathbf{q}'}_{j\beta} \epsilon^{\mathbf{q}''}_{k\gamma}}{\sqrt{M_i M_j M_k}\sqrt{\omega_{\mathbf{q}}\omega_{\mathbf{q}'}\omega_{\mathbf{q}''}}} \\ \times \Psi^{\alpha\beta\gamma}_{ijk} \mathrm{e}^{\mathrm{i}\mathbf{k}\cdot\mathbf{r}_i + \mathrm{i}\mathbf{k}'\cdot\mathbf{r}_j \mathrm{i}\mathbf{k}''\cdot\mathbf{r}_k}\end{aligned} \tag{2.55}$$

where $\Psi^{\alpha\beta\gamma}_{ijk}$ is the third-order force constant as in Eq. (2.5) and $\epsilon^{\mathbf{q}}_{i\alpha}$ is the component α associated eigenvector ϵ for atom i. M_i is the mass of atom i, and $\mathbf{r}_i$ is the vector locating its position.

2.4.3 Thermal conductivity from Green-Kubo formulation

In equilibrium molecular dynamics simulations, the fluctuation-dissipation theorem from linear response theory provides the connection between the energy dissipation in irreversible processes and the thermal fluctuations in equilibrium [Kubo et al. (2012)]. The net flow of heat, given by the heat current vector $\mathbf{J}$, fluctuates around zero at equilibrium. In the Green-Kubo (GK) method, the thermal conductivity is related to how long it takes to these fluctuations to relax to equilibrium. The thermal conductivity κ in Eq. (2.36) expressed in the Green-Kubo formulation writes,

$$\kappa_{\alpha\beta} = \frac{V}{k_B T^2} \int_0^{\infty} \langle J_\alpha(0) J_\beta(t) \rangle dt, \tag{2.56}$$

where V is the system volume, T refer to the equilibrium temperature of the system and $\mathbf{J}(t)$ is the time-dependent heat current vector in W m^{-2}, as in Eq. (2.34) and J_α is its α-th component. $\langle J_\alpha(0) J_\beta(t) \rangle$ denotes the heat current cross correlation function.

In the case of an isotropic material, the thermal conductivity is denoted by,

$$\kappa = \frac{V}{3k_B T^2} \int_0^\infty \langle \mathbf{J}(0) \cdot \mathbf{J}(t) \rangle dt, \tag{2.57}$$

where the factor $1/3$ refers to the directional average.

When applying the Green-Kubo method in MD simulations, one needs to keep in mind several points:

- The microcanonical ensemble, often denoted as NVE (fixed atom number, volume, energy), is required to sample the heat current in the equilibrium MD simulations. This is an intrinsic requirement of the linear response theory that supposes that the thermodynamic system only undergoes small perturbations.
- The system size has to be large enough to allow the long wavelength phonons to be represented in the system. If the size is too small, long wavelength phonons that usually contribute the most to the thermal conductivity cannot be formed and thus the thermal conductivity could be underestimated.
- The simulation time needs to be longer than the longest phonon relaxation time so that all the phonon modes could experience complete relaxation. This is especially important for systems at low temperatures when the relaxation times can be very long.
- The heat autocorrelation function $\langle \mathbf{J}(0) \cdot \mathbf{J}(t) \rangle$ needs to be sufficiently ensemble-averaged using many different trajectories. Different trajectories are often achieved by running the simulation with different initial conditions.

As an example of our computational procedure of the thermal conductivity and the convergence of the MD simulations, Figure 2.7 presents the time integrals of heat flux autocorrelation function (ACF) from Eq. (2.57). A data point of the thermal conductivity is usually obtained by averaging independent simulation trajectories (black curves in Figure 2.7) until the ensemble average converged (red curves in Figure 2.7). More than fifty independent simulations were performed. The error bars of the thermal conductivity can be defined based on the standard deviation of the averaged values.

2.5 Conclusions

In this chapter, we briefly present the method of molecular dynamics simulations and different popular techniques to access the important thermal trans-

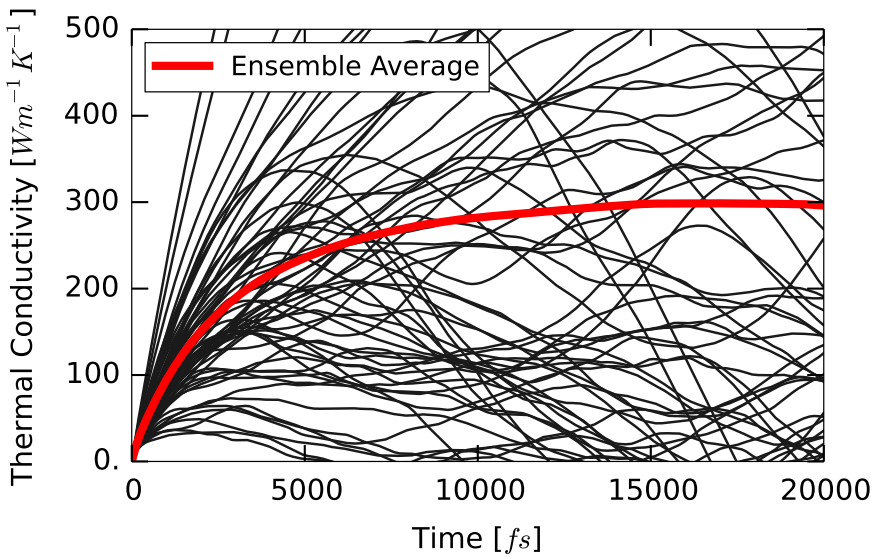

Figure 2.7: *Thermal conductivity proportional to the time integrals of the heat flux autocorrelation functions from Eq. (2.57). Black curves are the running integral of a single trajectory and the red curve refers to the ensemble average of different trajectories.*

port physical quantities, that is, the phonon transmission function/probability, interface thermal conductance and lattice thermal conductivity.

Classical molecular dynamics is compared with *ab initio* MD simulations. It is based upon empirical interatomic potentials and thus are less accurate than quantum-mechanical approaches, whereas it is cost-efficient in terms of computing resource and can be applied to realistic mesosystems. It uses classical statistics that may overestimates the heat capacity at high temperatures while brings in extra phonon-phonon scattering at low temperatures.

Phonon transmission coefficient is introduced and clarified with respect to the phonon transmission function in the atomistic Green's function formalism. The atomistic Green's Function technique to probe phonon transmission and compute thermal conductance is briefly reviewed and benchmarked. It is especially suitable for studying the phonon transport at interfaces within a wave framework. An equilibrium MD approch is also presented to calculate the interface thermal conductance without assuming the nature of phonons.

Finally, lattice thermal conductivity is introduced in the form of kinetic theory. To have access to the key ingredients of thermal conductivity, that is phonon group velocity and relaxation time, harmonic and anharmonic lattice dynamics methods were presented. An alternative method of phonon spectral energy

density based on equilibrium MD simulations is also presented to extract the normal modes and the relaxation time.

In the following chapters, we will use these powerful techniques to investigate the phonon interference effects in various systems.

Chapter 3

Phonon Interference and Energy Transport in Nonlinear Lattices with Resonance Defects

In this Chapter, we provide a new approach to demonstrate that heat in solids can be manipulated like light. While heat convection by fluids and heat radiation by light can be reasonably controlled, the conduction of heat through solids is less straightforward and has been an important challenge both in physics and engineering. Heat at room temperature is carried by lattice vibrations of ultra-high frequencies (10^{12} Hz), which are also called phonons, the quasi-particles that are analogous to the photons that carry light. In this work, we precisely control the heat flow by the atomic-scale phononic metamaterial, which contains deliberate flaws in the crystalline atomic lattice, channeling the heat through different phonon paths. Destructive interference between heat waves following different paths leads to the total reflection of the heat current and thus to the remarkable reduction in the material ability to conduct heat. By exploiting this destructive phonon interference, we model a very counter-intuitive possibility of thermal transport: more heat flow is blocked by the opening of the additional phonon channels. We provide an important further insight into the coherent control of phonons which can be applied both to sound and heat propagation.

3.1 Introduction

Destructive interference between waves traversing laterally-inhomogeneous interface can result in their total reflection. For instance, the strong resonance electromagnetic reflection found in metafilms filled with asymmetrical split-ring arrays [Fedotov et al. (2007)], in flexible metasurfaces [Walia et al. (2015)] and in stereometamaterials [Liu et al. (2009)] has offered the prospect of a multitude of applications as quantum optics [Altewischer et al. (2002)] and negative

refraction [García-Meca et al. (2009)]. As another example of destructive interference in optics, two-photon interference can result in a total cancellation of the photon output because of the coalescence of the two single photons, which was first observed by Hong et al. [Hong et al. (1987)]. This interference effect occurs because two possible photon paths interfere destructively, which produces the famous Hong-Ou-Mandel (HOM) dip in the detection probability of the output photons. The HOM dip has since been demonstrated both in optical [Santori et al. (2002); Beugnon et al. (2006)] and microwave [Wang et al. (2012)] regimes. Recently the two-photon destructive interference was demonstrated in a three-dimensional (3D) optical metamaterial [Lang et al. (2013)].

Similar destructive interference effect which results in the total reflection can be also realized in a phonon system. For sound waves, the enhanced phonon reflection was first described in Refs. [Kosevich (1997)] and [Fellay et al. (1997)] independently. Reference [Kosevich (1997)] interpreted the anomalous reflection of a long acoustic wave by a two-dimensional (2D) crystal defect as the *destructive interference between two phonon paths*: through the nearest-neighbor bonds and through the non-nearest-neighbor bonds which couple directly atomic layers adjacent to the defect plane. Reference [Fellay et al. (1997)] drew an analogy between electron scattering and phonon scattering and calculated numerically the phonon transmission with an asymmetric profile through a strip of oscillator chains connected in parallel.

Constant endeavor has been devoted to the precise control of heat conduction. Recent efforts have been concentrated on reducing the thermal conductivity κ via nanostructured materials with superlattices [Chen and Shakouri (2002); Chowdhury et al. (2009); Kim et al. (2006)] and with embedded nanoparticles [Mingo et al. (2009); Pernot et al. (2010); Chen et al. (2013)]. Most works have attributed the reduction in κ to the increased phonon scattering rate and the decreased phonon mean free path (MFP), which corresponds to the particle description of thermal transport in a lattice. However, the role of the destructive phonon interference is not well understood in the tailoring of thermal transport in the wave picture.

Thermal conductivity is a physical phenomenon that requires phonon anharmonicity as a key ingredient. In a perfect insulating crystal, harmonic phonons would never be scattered and such a crystal would have anomalous, diverging with the crystal size, thermal conductivity at all temperatures. Scattering of phonons by lattice imperfections, e.g., by isotopic impurities, in a one-dimensional (1D) crystal also does not result in the normal, converging with the crystal length, thermal conductivity [Rubin and Greer (1971b); Casher and Lebowitz (1971b)]. Only anharmonic phonon-phonon interactions and scattering can result in the normal heat transport in low-dimensional crystals, and

there is a great variety of nonlinear interatomic potentials which lead either to the normal or anomalous heat transport in one-dimensional chains [Savin and Kosevich (2014)]. Here we implement large-scale molecular dynamics (MD) simulations of phonon wave packet propagation in 3D lattices that incorporate realistic lattice potentials, which properly account for the nonlinearities in the interatomic interactions. Our MD simulations of anomalous phonon reflection (interference antiresonances) of short-wavelength phonons from internal crystal plane with embedded defects in a 3D lattice confirm previous analytical results for anomalous reflection of long-wavelength phonons in a 3D crystal with planar distribution of resonance defects (with 2D planar resonance defect) [Kosevich and Syrkin (1991); Kosevich (1997)] and of finite-wavelength phonons in 1D atomic chain with resonance defects [Kosevich (2008); Kosevich et al. (2008)]. In addition to the results on anomalous phonon scattering in harmonic lattices with resonance defects, we also show that the two-path interference antiresonances remain pronounced even when the interaction nonlinearity becomes fairly strong in a real 3D lattice. Therefore the two-path phonon interference in the proposed phononic metamaterial makes it possible to control thermal energy transport even in the case of large-amplitude lattice vibrations, for instance at room and higher temperature.

3.2 Atomistic model and Methodology

Here we introduce and model a realistic 3D atomic-scale phononic metamaterial which can be used for the storage and lasing of coherent terahertz phonons and for manipulating the flow of thermal energy [Han et al. (2014); Han et al. (2015)]. Phonon reflection is generated by exploiting the two-path phonon interference on internal crystal planes with embedded defects. The 2D planar defects force phonons to propagate through two paths: through unperturbed (matrix) and perturbed (defect) interatomic bonds [Kosevich (1997); Kosevich (2008); Kosevich et al. (2008)]. The resulting phonon interference gives antiresonances (zero-transmission resonances) in the phonon transmission spectra that can be controlled by the masses, force constants and 2D concentration of the defect atoms. Such patterned atomic planes can be considered as high-finesse atomic-scale *interference phonon metamirrors*. Our results show that the patterning of the defect-atom arrays with the formation of phonon metamirrors can lead to a new departure in thermal energy management [Maldovan (2013)], offering potential applications in thermal filters [Zhang et al. (2011)], thermal diodes [Li et al. (2012b)] and thermal cloaking [Narayana and Sato (2012); Xu et al. (2014); Han et al. (2014)].

3.2.1 Model Structure

Atomic distribution in the 3D phononic metamaterial with a face-centered cubic

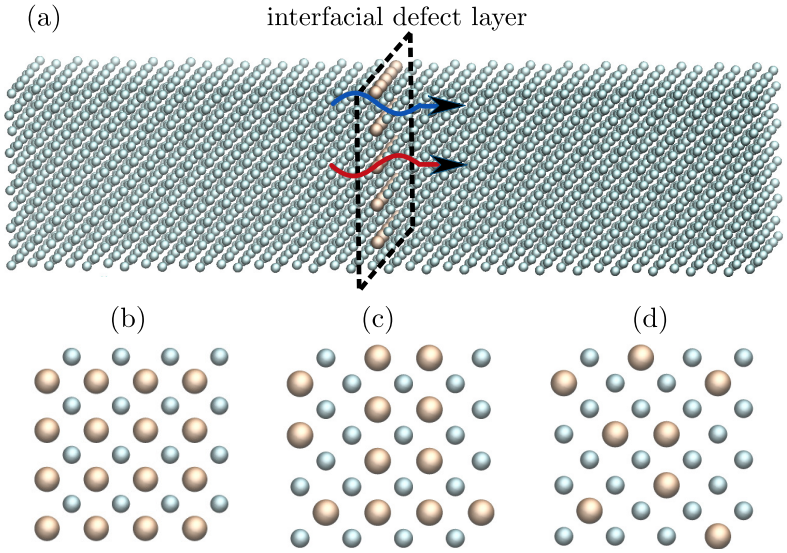

Figure 3.1: *(a) Interference Phonon Metamirror: 3D face-centered cubic lattice containing an internal (001) crystal plane in which an impurity-atom array is embedded. The brown atoms are the defect atoms and the green ones are the atoms of the host lattice. The red and blue curves refer to the phonon paths through the impurity atom bonds and through the host atom bonds, respectively. The presence of the two possible phonon paths can result in the two-path destructive-interference transmission antiresonance. (b) Periodic distribution of defect atoms with filling fraction* $f_d = 50\%$*. Randomly distributed defect atoms with (c)* $f_d = 37.5\%$ *and (d)* $f_d = 25\%$

(FCC) lattice with a 2D array of heavy defect atoms is depicted in Fig. 3.1(a). Each interference phonon metamirror consists of an atomic-scale metafilm: an internal (001) crystal plane in a cubic silicon (Si) lattice partially filled with germanium (Ge) impurity atoms, as shown in Fig. 3.1(a). The defect atoms can be distributed periodically or randomly in the defect crystal plane with different filling fractions f_d. When the defects do not fill completely the defect plane, phonons have two paths to cross such an atom array as shown in Fig. 3.1(a), whereas the phonon path through the host atoms is blocked when the defect layer is constituted by a uniform impurity-atom array, 100% packed with the impurity atoms. Two types of atomic-scale metamaterials were studied using realistic interatomic potentials: a FCC lattice of argon (Ar), in which the defects are heavy Ar isotopes, and a diamond lattice of silicon with germanium atoms as the heavy-mass and atomic-bonds defects.

3.2.2 Methodology

The interactions between Ar atoms are described by the Lennard-Jones potential [Kaburaki et al. (2007)]. The covalent Si:Si/Ge:Ge/Si:Ge interactions are modeled by the Stillinger-Weber potential [Stillinger and Weber (1985b)]. To probe the phonon transmission, MD with the phonon wave packet method [Schelling

et al. (2002b)] was used to provide the per-phonon-mode energy transmission coefficient $\alpha(\omega, l)$. We excited a realistic 3D Gaussian wave packet centered at the frequency ω and wave vector $\vec{k}$ in the reciprocal space and at $\vec{r}_0$ in the real space, with the spatial width (coherence length) l in the direction of $\vec{k}$. The wave packet generation was performed by assigning the displacement $\vec{u}_i$ for the atom i as presented in Section (2.2.1),

$$\vec{u}_i = A\vec{e}_i(\vec{k}) \exp\left(\mathrm{i}\left[\vec{k}\cdot(\vec{r}_i - \vec{r}_0) - \omega t\right]\right) \exp\left(-\frac{\left[\vec{r}_i - \vec{r}_0 - \vec{v}_g t\right]^2}{4l^2}\right),$$

where A is the wave packet amplitude, $\vec{e}_i(\vec{k})$ is the phonon polarization vector, ω is the eigenfrequency for the wave vector $\vec{k}$ within a single branch of the phonon dispersion curve, $\vec{v}_g$ is the phonon group velocity along the wave vector $\vec{k}$ at the wave packet center frequency ω. Wave amplitude A of the generated phonon wave packets was taken sufficiently small such that the anharmonic coupling to other lattice modes is kept weak. Hence the wave packets propagate in an effectively harmonic crystal without any perceptible spreading or scattering. The wave packet was set to propagate normally to the defect layer, where an elastic scattering results in transmitted and reflected waves. The wave packet energy transmission coefficient $\alpha(\omega, l)$ is defined as the ratio between the energy carried by the transmitted and initial wave packets, centered at the given phonon mode $(\omega, \vec{k})$ with the spatial extent l. The plane-wave limit is reproduced by the wave packets with the spatial width l much larger than the wavelength λ_c of the wave packet central frequency. All the MD simulations were performed with the LAMMPS code package [Plimpton (1995)].

3.3 Results and Discussions

In this section we consider separately the interference resonance profile in the phonon transmission coefficient, the isotopic shift of the resonance reflection versus the defect masses, and the phonon screening effect in the thermal conductance. Then we report the two-path phonon interference in a silicon crystal with germanium impurities. We show that the random distribution of the defects in the crystal plane and the nonlinearity of the potential do not deteriorate the interference resonances. Finally we show that the width of the interference antiresonance dip can provide a measure for the coherence length of the phonon wave packet.

3.3.1 Interference Resonance Profile

The transmission coefficient $\alpha(\omega)$ of the wave packet with $l = 20\lambda_c$, retrieved from MD simulations of an Ar metamaterial, is presented in Fig. 3.2. The incident phonons undergo a total reflection from the defect layer at the antiresonance frequency ω_R. Phonon transmission spectra displays an interference

antiresonance profile since the two phonon paths interfere destructively at ω_R. A total transmission at ω_T follows the interference antiresonance, which is reminiscent of the Fano resonances Fano (1961). For a uniform heavy-defect-atom array, the zero-transmission antiresonance profile will be totally suppressed and replaced by a monotonous decay of the transmission with frequency. In the later case, only the phonon path through the defect atoms is accessible.

We emphasize that the second phonon path is indispensable to the emergence of the zero-transmission dip, which cannot be sufficiently described by the Fano resonance. We clarify this by studying the phonon transmission through two successive internal crystal planes completely filled with resonance defect atoms, when a local resonant transmission maximum is observed instead of a zero-transmission dip, see Fig. 2 in Ref. [Han et al. (2014)]. This transmission maximum satisfies well the Fano-resonance condition [Fano (1961)] of a discrete state resonating with its continuum background, but no zero-transmission dip occurs because of the absence of the second phonon path [Kosevich and Syrkin (1991); Kosevich (1997)]. This transmission maximum can be considered as a phonon analogue of the Fabry-Pérot resonance in optics, which requires only a single phonon (or photon) path. Therefore this observation clearly corroborates the two-path destructive phonon interference nature of the zero-transmission dip (antiresonance) in the phonon transmission coefficient $\alpha(\omega)$.
To understand further the phonon antiresonances caused by the interference between two phonon channels, we use an equivalent model of monatomic quasi-1D lattice of coupled harmonic oscillators [Kosevich (2008)], depicted in the inset in Fig. 3.2. In model (a), phonons propagate through two paths: through the host atom bonds, and through those of the impurity atoms, whereas in model (b) only the second channel remains open. The model (a) gives the energy transmission coefficient for the plane wave:

$$\alpha(\omega) = \frac{(\omega^2 - \omega_R^2)^2(\omega_{\max}^2 - \omega^2)}{(\omega^2 - \omega_R^2)^2(\omega_{\max}^2 - \omega^2) + C\omega^2(\omega^2 - \omega_T^2)^2}\,, \tag{3.1}$$

where $\omega_{R,T}$ are the frequencies of the reflection and transmission resonances, $\omega_{\max}$ is the maximal phonon frequency for a given polarization, $\omega_R < \omega_T < \omega_{\max}$. C is a real positive coefficient given by the atomic masses, force constants and f_d, $C = 0$ for $f_d = 0$. The ω_R frequency exists only in the presence of the additional channel, which is open for wave propagation through the bypath around the defect atom, see inset (a) in Fig. 3.2. As follows from Eq. (3.1) and Fig. 3.2, $\alpha(\omega_R) = \alpha(\omega_{\max}) = 0$ and $\alpha(0) = \alpha(\omega_T) = 1$.
The energy transmission coefficient $\alpha(\omega, l)$ of the wave packet with the given central frequency ω and spatial width l is determined by the convolution of the transmission coefficient for the plane wave $\alpha(\omega) = \alpha(\omega, \infty)$, given by Eq. (2), with a Gaussian wave packet in frequency domain with the width $\Delta\omega = v_g/(2l)$:

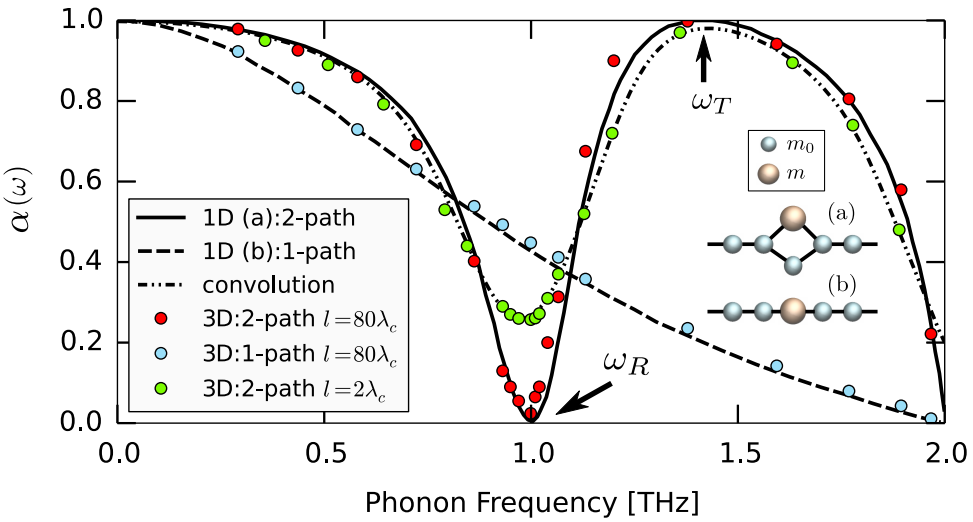

Figure 3.2: *Spectra of the energy transmission coefficient $\alpha(\omega, l)$ predicted by equivalent quasi-1D model (solid and dashed lines) and by MD simulations (symbols) for a 3D Ar metamaterial with defect crystal plane containing heavy isotope impurities, with mass $m = 3m_0$. Dashed-dotted line is the convolution Eq. (3.2) of the plane-wave transmission coefficient $\alpha(\omega)$ from Eq. (3.1) with a Gaussian wave packet in frequency domain with $l = 2\lambda_c$. Red and blue symbols present transmission of the wave packet with $l = 20\lambda_c$ through the two paths and through one path in the Ar metamaterial with planar defect, respectively; green symbols present transmission of the wave packet with $l = 2\lambda_c$ through the two paths. (Inset) Two possible quasi-1D lattice models describing phonon propagation through the lattice region containing the local defect: (a) phonons can propagate through the defect and host atoms bonds; (b) phonons can propagate only through the defect atom bonds. Black sticks between the atoms present atom bonds. In the case of Ar lattice, the coefficients in Eq. (3.1) are $\omega_R = 1.0$, $\omega_T = 1.4$, $\omega_{max} = 2.0$ and $C = 0.25$. The quasi-1D model (a) is equivalent to a 2D crystal plane partially filled with periodically alternating isotopes with different masses, with $f_d = 50\%$, in a 3D Ar lattice. The 1D model (b) is equivalent to a 2D crystal plane completely filled with heavy isotopes, with $f_d = 100\%$, in a 3D Ar lattice.*

$$\alpha(\omega, l) = \int_{-\omega_{max}}^{\omega_{max}} \alpha(\omega') \exp\left(-\frac{(\omega - \omega')^2}{2\Delta\omega^2}\right) \frac{d\omega'}{\Delta\omega\sqrt{2\pi}}\,. \tag{3.2}$$

It is noteworthy that the Gaussian phonon wave packets minimize the product of the frequency, $\Delta\omega$, and time, $\Delta t = l/v_g$, uncertainties: $\Delta\omega \cdot \Delta t = 1/2$, as well as the product of the wave number component, $\Delta k_x = \Delta\omega/v_g = 1/(2l)$, and coordinate, $\Delta x = l$, uncertainties: $\Delta k_x \cdot \Delta x = 1/2$, see also Section 3.7 below. This property of the Gaussian phonon wave packets is similar to the property of the Gaussian wave packets of coherent states in quantum mechanics, which minimize the product of the momentum component, Δp_x, and coordinate

uncertainties: $\Delta p_x \cdot \Delta x = \hbar/2$ [Landau and Lifshitz (1991)], see also Ref. [Kosevich and Gann (2013)] for a similar property of the Gaussian wave packets of magnon coherent states in spin chains.

In the transmission of a narrow wave packet with $l = 2\lambda_c$, the interference effect is weakened by a large number of frequency components, when the plane-wave approximation ($l \gg \lambda_c$) is broken and the transmission at ω_R is not zero any more, i.e. $\alpha(\omega_R, l) > 0$, which is the case also in Ref. [Hong et al. (1987)]. As one can see in Fig. 3.2, an excellent agreement in transmission coefficients is demonstrated between the equivalent quasi-1D model provided by Eqs. (3.1) and (3.2) and the MD simulations of the 3D atomic-scale phononic metamaterial with the use of realistic interatomic potentials.

3.3.2 Isotopic Shift of Resonances

In a lattice with atomic impurities, the substituent atoms scatter phonons due to the difference in mass and/or bond stiffness. Since no bond defect was introduced, the loci of the resonances are determined only by the mass ratio (MR) of the isotope defects and host atoms. As the isotope defects become heavier, the two-path phonon interference antiresonance becomes more pronounced in terms of the depth and width of the phonon-transmission dip and demonstrates a red-shift of the dip, thus impeding the long-wavelength phonons, as shown in Fig. 3.3(a) and (c) for longitudinal and transverse phonons, respectively. The equivalent quasi-1D lattice model gives the following expression for the frequency of the transmission dip:

$$\omega_R = \omega_{max}/\sqrt{m/m_0 + 1}\ , \tag{3.3}$$

where m and m_0 refer to the atomic mass of the isotope defect and host atom, with MR$=m/m_0 > 1$. The transmission resonance at $\omega = \omega_T$ is much less sensitive to the defect mass since it is largely determined by the mass of the host atom. As depicted in Fig. 3.3(b) and (d), the spectral positions of the interference resonances ω_R are again in an excellent agreement with the analytical prediction of the equivalent quasi-1D lattice model given by Eq. (3.3) for both longitudinal and transverse phonons.

3.3.3 Phonon Screening Effect

In Fig. 3.2, the transmission spectra for longitudinal phonons across the uniform defect-atom array is plotted to be compared with that of the 50%-filled defect-atom array. At the frequency of the two-path interference antiresonance ω_R, an array of 50% defect atoms has a transmittance two orders of magnitude smaller than that of a uniform defect-atom array. The difference between the very strong phonon reflection on a 50%-filled defect array and the high phonon transmission across a uniform defect array can result in a counter-intuitive

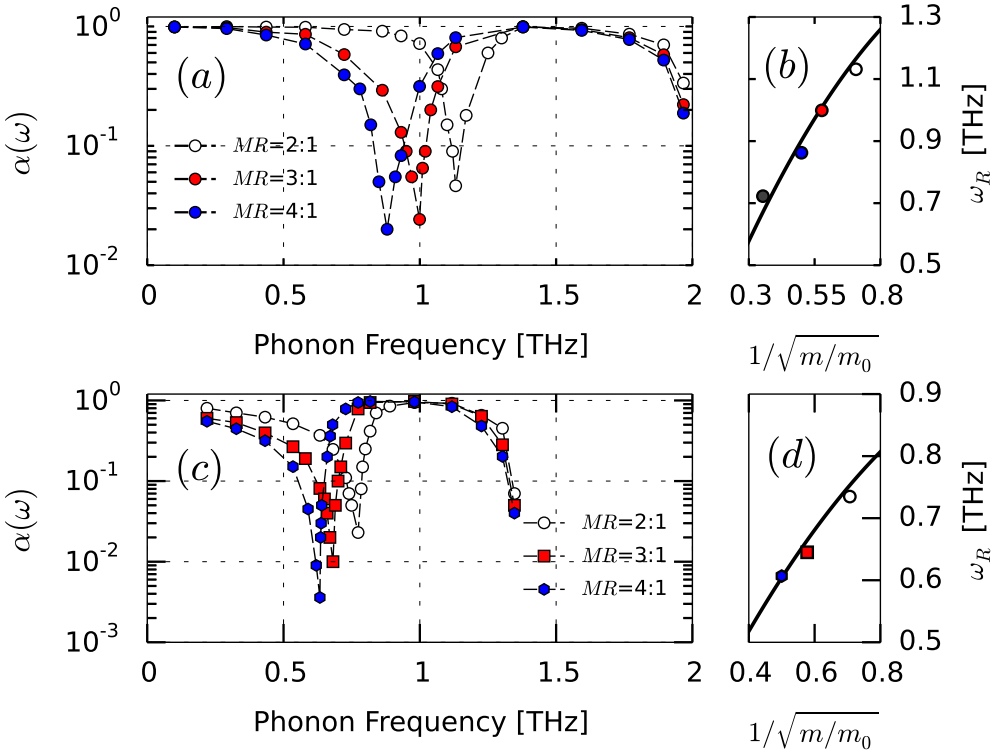

Figure 3.3: *(a) and (c): Spectra of phonon transmission coefficient $\alpha(\omega)$ of longitudinal (a) and transverse (c) acoustic waves through the phononic metamaterial, which consists of 2D crystal plane filled with periodically alternating isotopes with different mass ratio (MR) m/m_0 with $f_d = 50\%$ in a 3D Ar lattice. Dashed lines are the guides to the eye. (b) and (d): Isotopic shift of the two-path phonon interference antiresonance versus the inverse square root of the mass ratio for longitudinal (b) and transverse (d) acoustic waves. Symbols present the resonances predicted by MD simulations for a 3D lattice, solid line shows the analytical prediction of the equivalent quasi-1D lattice model given by Eq. (4)*

effect: an array of randomly alternating host and impurity atoms can scatter more phonons than an array with a uniform distribution of heavy isotopes. This anomalous phonon reflection phenomenon in molecular systems can find its acoustic counterpart in macroscopic structures [Kosevich (2008); Estrada et al. (2008); Liu et al. (2000)]. In Ref. [Estrada et al. (2008)], perforated plates were proved to shield ultrasonic acoustic waves in water much more effectively than uniform plates. Liu *et al.* [Liu et al. (2000)] managed to break the mass-density law for sonic transmission by embedding high-density spheres coated with a soft material in a single layer of a stiff matrix.

We calculate the interfacial thermal conductance G by following the Landauer-

like formalism Khalatnikov (2000):

$$G = \int \sum_{\nu} \hbar\omega(\vec{k},\nu) v_{g,z}(\vec{k},\nu) \alpha \frac{\partial}{\partial T} n_{\mathrm{BE}}(\omega,T) \frac{\mathrm{d}\vec{k}}{(2\pi)^3}\,, \tag{3.4}$$

where $\hbar$ is the reduced Planck constant, $v_{g,z}$the phonon group velocity in the cross-plane direction, $n_{\mathrm{BE}}(\omega,T)$ is the Bose-Einstein distribution of phonons at temperature T, $n_{\mathrm{BE}}(\omega,T) = [\exp(\hbar\omega/k_BT) - 1]^{-1}$, k_B is the Boltzmann constant. The integral is carried out over the Brillouin zone and the sum is over the phonon branches. By embedding defect atoms in a crystal plane monolayer, we manage to reduce the thermal conductance by 30% with respect to the case of pristine lattice, with no defects, as shown in Fig. 3.4(a). This destructive-interference-induced effect can be used for the explanation of the remarkable decrease of κ of SiGe alloy with very small amount of Ge atoms, with respect to the pristine Si lattice [Garg et al. (2011)]. G is further reduced by considering the (second) non-nearest-neighbor (NNN) bonds C_2 between the host atoms on the two sides of the uniform defect layer in addition to the nearest-neighbor (NN) bond C_1 linking the host and adjacent defect atoms. This reduction comes from the suppression of phonon transmission at high frequencies, shown in Fig. 3.4(b), which is due to the opening of the second phonon path through the host atom bonds destructively interfering with the first path through the defects. The occurrence of the second phonon path substantially reduces G by 16% even if it is weak: $C_2 = 0.08C_1$. G is reduced by 16% Although C_2 is only 8% of C_1, This provides another evidence of the control of heat transport by the two-path destructive phonon interference: more heat flux is blocked despite the opening of the additional phonon paths, even in the absence of phonon resonances.

It is also interesting that antiresonance dips in the transmission do not necessarily yield minimal thermal conductance.

3.3.4 Two-Path Phonon Interference in Si crystal with Ge impurities

Figure 3.5 illustrates the two-path interference phonon antiresonances in the metamaterial fabricated as follows: 2D planar distribution of Ge atoms is embedded in a Si crystal. Ge and Si atoms have mass ratio of 2.57 and thus the Ge-atom array introduces both the heavy-mass and atomic-bond defects due to a weaker Si:Ge coupling than the Si:Si interaction Stillinger and Weber (1985b). Phonons from transverse and longitudinal acoustic branches experience strong resonant reflections at the defect crystal plane, 50%-filled with Ge atoms, while the short-wavelength phonons near the edge of the Brillouin zone are strongly reflected by the defect crystal plane, completely filled with Ge atoms.

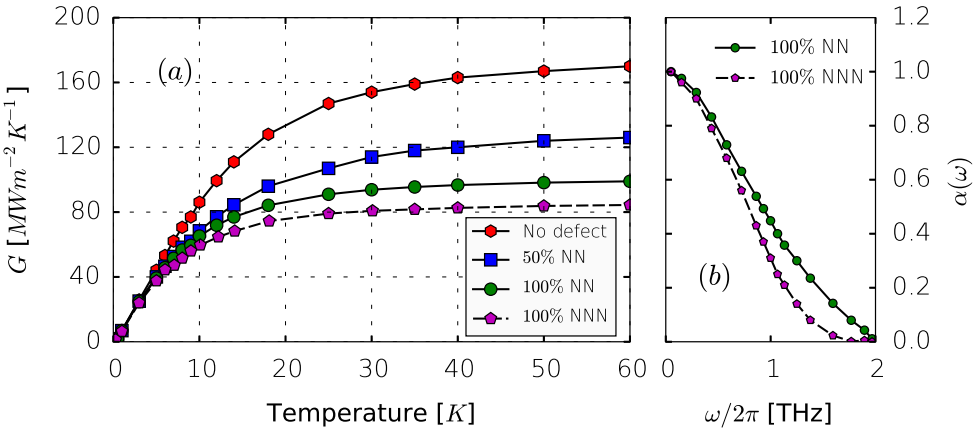

Figure 3.4: *(a) Temperature dependence of interfacial thermal conductance across a crystal plane, 50%-filled with periodic array of heavy isotope defects (rectangles), and across a uniform defect crystal plane with (pentagons) and without (circles) the second phonon path induced by the non-nearest-neighbor (NNN) bonds in addition to the nearest-neighbor (NN) bonds, in comparison with that across an atomic crystal plane without defects (hexagons). (b) Transmission coefficient $\alpha(\omega)$ for a uniform defect crystal plane with (pentagons) and without (circles) the second phonon path induced by the NNN bonds*

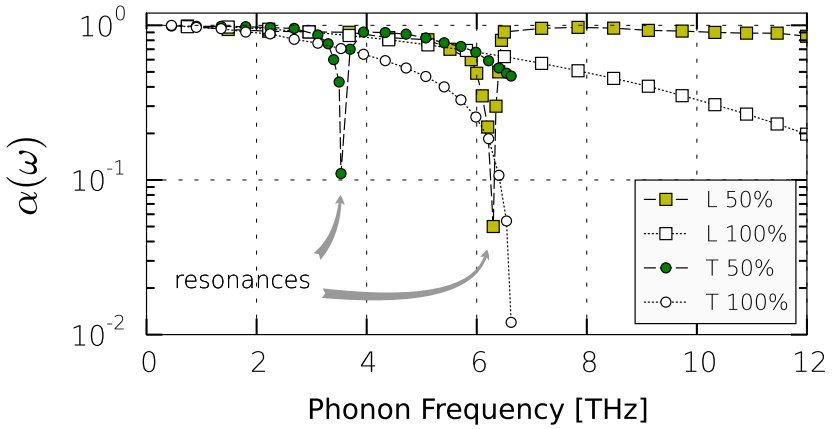

Figure 3.5: *Two-path interference phonon antiresonances for transverse and longitudinal phonons across a partially-Ge-filled defect crystal plane (green circles and yellow squares) plotted along with the non-resonant transmission across a completely-Ge-filled defect crystal plane (open squares and circles) in a Si crystal as phononic metamaterial*

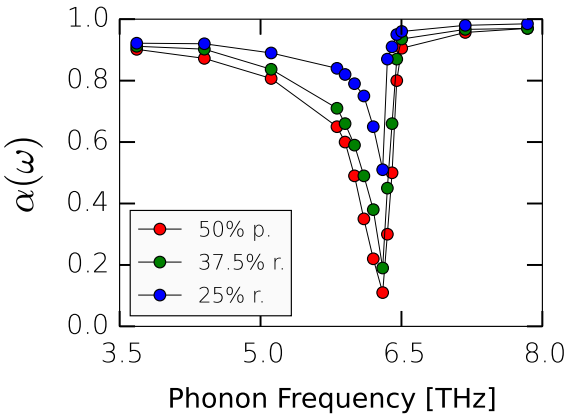

Figure 3.6: *Transmission coefficient $\alpha(\omega)$ for longitudinal phonons through the planar defect in a Si crystal, which contains randomly (r) distributed embedded Ge atoms with $f_d = 37.5\%$ and 25%, compared with $\alpha(\omega)$ through the planar defect, which contains periodically (p) distributed embedded Ge atoms with $f_d = 50\%$. The computed $\alpha(\omega)$ was averaged over different random distributions*

3.3.5 Random Distribution of Atoms

In contrast to light [Mitrofanov et al. (2001); Degiron et al. (2004)], even a single defect atom in a crystal plane produces interference reflection antiresonances for Gaussian beams of (longitudinal or transverse) phonons because of the presence of the two phonon paths. Therefore, phonon reflection antiresonances should exist even in the absence of the periodicity in the defect-atom distribution in the crystal plane because of the localized nature of the resonances. This argument is supported by further study of phonon transmission through the arrays of Ge atoms in a crystal plane in Si-crystal-based phononic metamaterial, distributed with different filling fractions f_d and randomness. Strong transmission dip, similar to that produced by periodic Ge atoms arrays, remains pronounced in both cases, as shown in Fig. 3.6. This was shown experimentally to be equally valid in macroscopic acoustic metamaterials [Liu et al. (2000)].

Chen *et al.* reduced the thermal conductivity κ below the alloy limit by the partial intermixing (segregation) of Ge atoms in Si superlattices [Chen et al. (2013)]. Their *ab initio* calculations showed that phonon mean free path was substantially reduced in the low frequencies [Chen et al. (2013)]. We note that the clusters of Ge atoms can be considered as randomly dispersed heavy-mass oscillators, which scatter low-frequency phonons at the interference antiresonances whose frequencies are given by the isotopic-shift law Eq. (3.3). With this destructive interference, we can also relate the extremely low κ found in the $In_{0.53}Ga_{0.47}As$ alloy, randomly filled with heavy ErAs nanoparticles [Kim

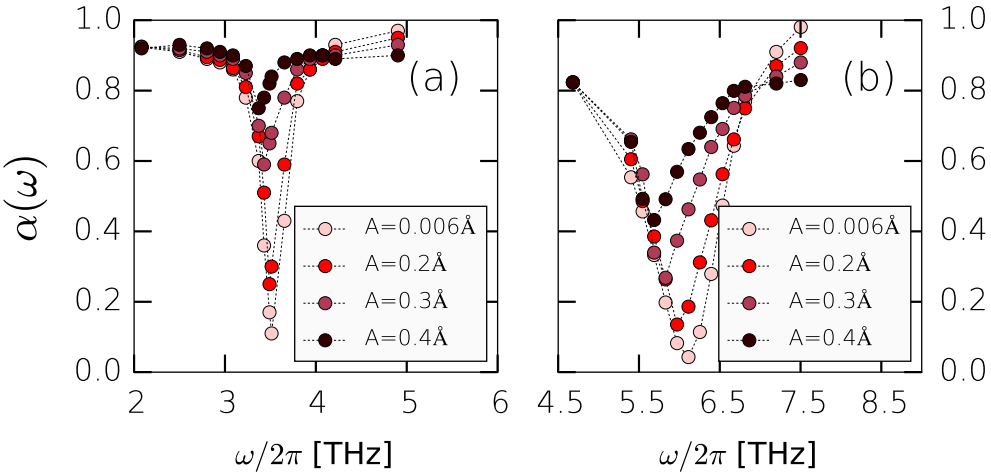

Figure 3.7: *Evolution of the interference antiresonance in the phonon transmission coefficient $\alpha(\omega)$ through the partially-Ge-filled, with $f_d = 50\%$, internal crystal plane in Si lattice versus the increasing wave amplitude for (a) transverse and (b) longitudinal phonons*

et al. (2006)].

3.3.6 Nonlinear Effects

The nonlinear effects in the two-path interference phonon antiresonances were investigated by increasing the amplitude A of the incident phonon wave packet, as shown in Fig. 3.7 for the phonon transmission coefficient through the partially-Ge-filled, with $f_d = 50\%$, internal crystal plane in Si lattice. As A increases, the reflection becomes less pronounced with more heat flux passing through, which provides direct evidence of inelastic phonon scattering at the defect plane. The antiresonances demonstrate the red shifts in frequency due to the anharmonic (cubic first of all) terms in the interatomic potential. We also note in this connection that our computation of a quasi-1D atomic chain, containing an impurity atom characterized by non-parabolic (nonlinear) interaction potential with the neighboring host atoms, agrees well with our MD results for 3D lattice. The interference antiresonances remain pronounced even when the interaction nonlinearity becomes fairly strong. Therefore the two-path interference phonon antiresonances in the proposed phononic metamaterial make it possible to control thermal energy transport even in the case of large-amplitude lattice vibrations, for instance at room and higher temperature.

3.3.7 Wave Packet Coherence Length Determination

The decrease in 2D defect filling fraction f_d narrows the width of the antiresonance dip because of the weakening of the relative strength of the “defect-bond"

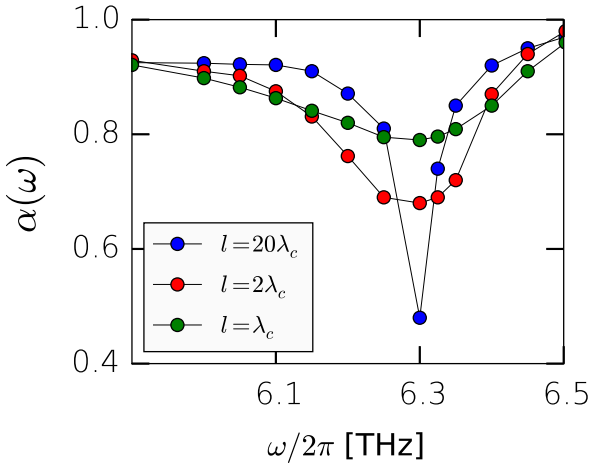

Figure 3.8: *Broadening of the antiresonance dip in the energy transmission coefficient* $\alpha(\omega, l)$ *in the limit of small filling fraction* $f_d = 5\%$ *for the wave packets with short coherence lengths* ($l = \lambda_c$ *and* $l = 2\lambda_c$*, green and red circles), in comparison with that for an almost plane-wave wave packet* ($l = 20\lambda_c$*, blue circles)*

phonon paths through the crystal plane, see Fig. 3.1 and Eq. (3.1). In general, the width $\Delta\omega$ of the antiresonance dip for the two-path phonon interference is determined by both the f_d and finite coherence length l of the phonon wave packet. As follows from Fig. 3.2, for the large $f_d = 50\%$ $\Delta\omega$ is not sensitive to l. In the limit of small f_d and for $l \gg \lambda_c$, $\Delta\omega$ is narrow and proportional to f_d, as shown in Figs. 3.6 and 3.8. In this limit, for the wave packet with a short width l, $l \sim \lambda_c$, $\Delta\omega$ will be determined mainly by l. From Fig. 3.8, the width $\Delta\omega$ of the antiresonance dip for the wave packet with $l = 2\lambda_c$ is $\Delta\omega/(2\pi) = 0.19$ THz. Then from the minimal value of the product $\Delta\omega \cdot \Delta t = 1/2$, which is realized for the Gaussian wave packets, we get the wave packet width in time domain $\Delta t = 0.42$ps and the wave packet spatial width (coherence length) $l = v_g \Delta t \approx 3.1$nm, where $v_g \approx 7.5$km/s is the longitudinal phonon group velocity in Si at $\omega = \omega_R$, see Ref. [Schelling and Phillpot (2003)]. This length coincides with the wave packet coherence length $l \approx 3.2$nm, which was used in the MD simulations shown in Fig. 3.8. The width $\Delta\omega$ of the antiresonance dip for the wave packet with a shorter coherence length $l = \lambda_c$ is larger than that of the wave packet with $l = 2\lambda_c$, see Fig. 3.8. Therefore the width of the two-path phonon interference antiresonance dip in the transmission spectrum can provide a measure of the coherence length of the phonon wave packet.

3.4 Conclusions

In conclusion, we provide a comprehensive modeling of atomic-scale phononic metamaterial for the control of heat conduction by exploiting the two-path

interference phonon antiresonances. Thermal phonons crossing crystal plane partially filled with resonance defect atoms can undergo complete reflection caused by destructive phonon interference. Such patterned atomic planes can be considered as high-finesse atomic-scale *interference phonon metamirrors*. Interference phonon antiresonances are not deteriorated by the aperiodicity in the defect-atom distribution and the anharmonicity of interatomic bonds. The width of the antiresonance dip provides a measure of the coherence length of the phonon wave packet. And, finally, we would like to emphasize that strong resonance reflection of electromagnetic waves, which has been observed in metafilms partially filled with asymmetrical split-ring arrays [Fedotov et al. (2007)], in stereometamaterials [Liu et al. (2009)], in flexible metasurfaces [Walia et al. (2015)] and in microwave metamirrors [Asadchy et al. (2015)], can also be interpreted as interference photon antiresonance in an optically transparent plane, partially filled with subwavelength plasmonic or microwave resonating structures [Kosevich (2008); Han et al. (2014)].

Chapter 4

Ultra-compact Interference Phonon Nanocapacitor for Storage and Lasing of Terahertz Lattice Waves

In this Chapter, We introduce a novel ultra-compact nanocapacitor of coherent phonons formed by high-finesse interference mirrors based on atomic-scale semiconductor metamaterials. Our molecular dynamics simulations show that the nanocapacitor stores monochromatic terahertz lattice waves, which can be used for phonon lasing - the emission of coherent phonons. Either one- or two-color phonon lasing can be realized depending on the geometry of the nanodevice. The two-color regime of the interference cavity originates from different incidence-angle dependence of phonon wave packet transmission for two wave polarizations at the respective antiresonances. Coherent phonon storage can be achieved by cooling the nanocapacitor initially thermalized at room temperature or by the pump-probe technique. The linewidth narrowing and the computed relative phonon participation number confirm strong phonon confinement in the interference cavity by an extremely small amount of resonance defects. The emission of coherent terahertz acoustic beams from the nanocapacitor can be realized by applying tunable reversible stress which shifts the antiresonance frequencies.

4.1 Introduction

Phonons, quanta of lattice waves, having significantly shorter wavelengths than photons at the same frequency, may allow to pursue improved resolution in to-

mographic, ultrasonic and other imaging techniques using focused sound waves. In particular, the terahertz (THz) phonons that have wavelengths comparable to the lattice constants would allow to detect microscopic subsurface structure up to the atomic scale, also in opaque materials, with the precision higher than that optical microscopes can provide. To this end, ultrahigh-frequency coherent phonon source are urgently desired. Coherent lattice phonon emission has been studied in a single-traped ion [Vahala et al. (2009)] and an ultracold atomic gas [Mendonca et al. (2010)], semiconductor superlattices [Trigo et al. (2002); Huynh et al. (2006); Lanzillotti-Kimura et al. (2007); Beardsley et al. (2010); Maryam et al. (2013)], optomechanical systems [Kippenberg and Vahala (2008); Grudinin et al. (2010); Khurgin et al. (2012)] and electromechanical resonators [Mahboob et al. (2012)]. Coherent phonon manipulations for energy transport in dynamical nanosystems have been an emerging focus of research [Li et al. (2012a)]. Various functional components of nanophononic devices, such as thermal diodes, thermal transistors and thermal memory, have been investigated theoretically and experimentally.

The development of nanophononic devices which enable controllabe generation and coherent emission of phonons has recently emerged as the subject of intense interest [Trigo et al. (2002); Huynh et al. (2006); Lanzillotti-Kimura et al. (2007); Beardsley et al. (2010); Grudinin et al. (2010); Mahboob et al. (2013); Fainstein et al. (2013); Kippenberg and Vahala (2008); Khurgin et al. (2012)]. Conventional sources of sound waves, such as piezoelectric transducers, fail to operate efficiently above a few tens of gigahertz (GHz). The highest emitted-phonon frequency was achieved in a semiconductor superlattice under electrical bias in which half-THz Coherent phonons were released during electrons tunneling through the coupled quantum wells [Beardsley et al. (2010)]. Similar coherent phonon emission was also observed in hybrid optomechanical schemes in which optically pumped microcavities produce stimulated acoustic emission in the range of MHz [Grudinin et al. (2010)] and GHz [Fainstein et al. (2013)] frequencies. An entirely mechanical phonon laser at sub-MHz frequencies was achieved in an electromechanical resonator [Mahboob et al. (2012); Okamoto et al. (2013)], in analogy with a three-level laser scheme [Mahboob et al. (2013)]. For these systems, the need for strong optical pumping or complex actuator tuning may limit the development of phonon lasers because unavoidable compromises have to be made in the design scheme.

We introduce a three-dimensional (3D) interference phonon nanocapacitor based on atomic-scale semiconductor metamaterials. The nanocapacitor allows the confinement and storage of THz coherent phonons with an ultra-high monochromatic quality by an adiabatic cooling of the nanodevice or by the pump-probe optical technique [Huynh et al. (2006); Lanzillotti-Kimura et al. (2007)]. We show that the nanocavity structure, formed by high-finesse interference phonon mirrors (IPMs) [Kosevich (1997); Han et al. (2014)], can efficiently

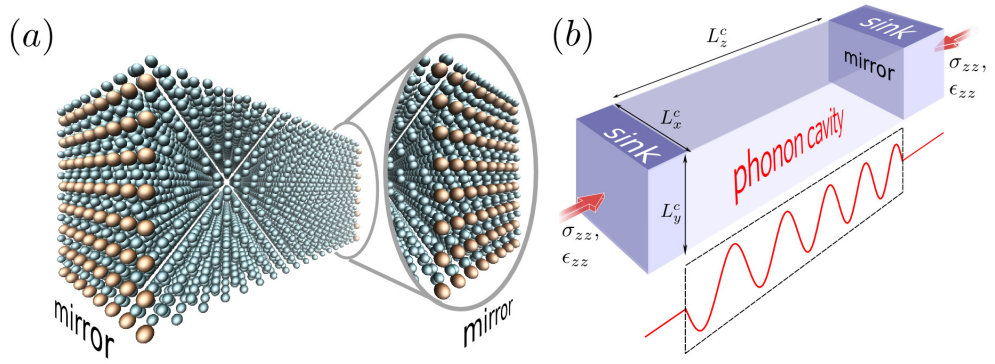

Figure 4.1: *Silicon interference phonon capacitor composed of two interference phonon mirrors separated by a spacer. a) The atomistic view of the phonon capacitor and mirrors. The atoms in brown are Ge impurity atoms and the green ones are Si atoms of the host lattice. b) Phonon capacitor coupled to two heat sinks under the applied uniaxial stress σ_{zz}. The dimensions of the capacitor are $L_x^c = L_y^c = 8$ nm and $L_z^c = 35$ nm.*

store a large number of coherent nonequilibrium phonons. The nanocapacitor can emit coherent THz phonon beams upon application of tunable reversible stress. Such emission can be considered as "phonon lasing". Either one- or two-color phonon lasing can be realized depending on the geometry of the nanodevice, in contrast to the usual one-color photon lasing. The achievement of generation and emission of coherent THz lattice waves phonons will provide an essential step towards active hypersound devices and nanophononic applications of THz acoustics, including surgery with focused ultra- and hyper-sound in medicine[Khokhlova et al. (2014)]. On the other hand, high sensitivity of phonon interference antiresonance to the applied stresses and strains makes it possible to use the ultra-compact capacitor also as a nano-detector of atomic-scale displacements and strains in the surrounding material, like single molecule can be used as a detector of nanomechanical motion[Puller et al. (2013); Tian et al. (2014)].

4.2 Atomistic Model

A detailed atomistic presentation of the phonon capacitor is depicted in Fig. 4.1(a). The nanocapacitor consists of two IPMs separated by a spacer made of bulk silicon (Si). Each IPM is composed of an atomic-scale metafilm: an internal crystal plane in Si lattice partially embedded with segregated germanium (Ge) impurities atoms, as shown in Fig. 4.1(a). The confinement of phonon modes in the cavity results from the two-path destructive phonon interference in the mirrors [Kosevich (1997); Han et al. (2014)]. Ge atoms in a crystal plane of the IPM force phonons to propagate through two paths: through unperturbed (matrix) and perturbed (defect) interatomic bonds. The resulting destructive

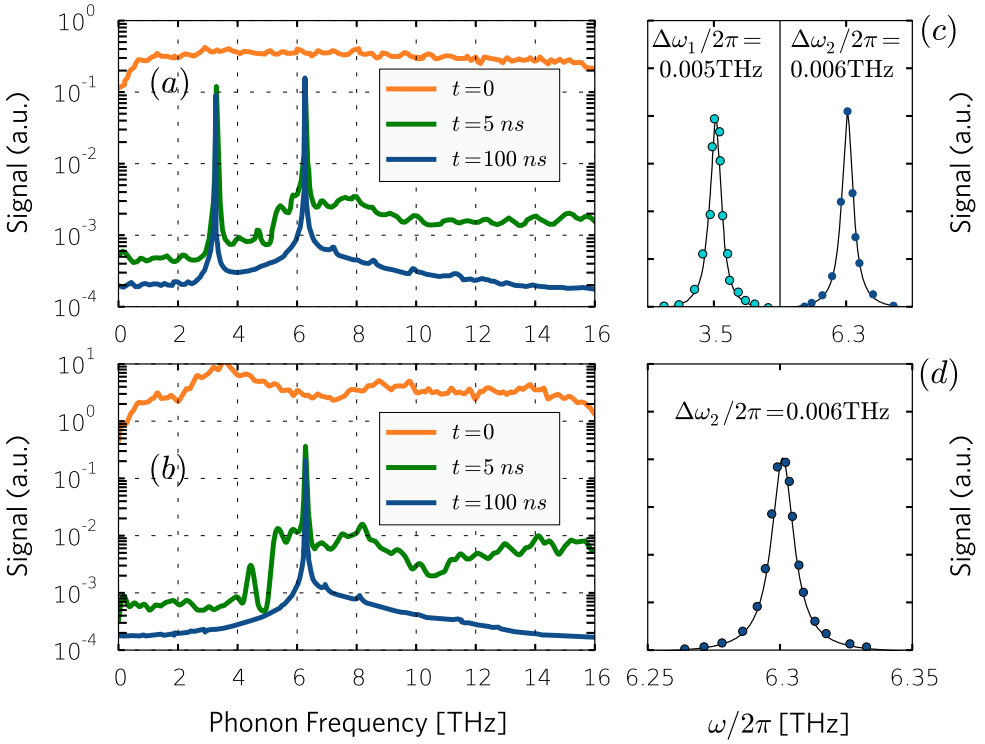

Figure 4.2: *Power spectral density of atomic kinetic energy in the nanocapacitor initially thermalized at $T = 300K$ as a function of time delay t after the cooling onset. Nanocapacitor dimensions are $L_x^c = L_y^c = 8$ nm and $L_z^c = 35$ nm (a), and $L_x^c = L_y^c = 33$ nm and $L_z^c = 35$ nm (b). (c) and (d): Gaussian fit of the capacitor phonon peaks to measure FWHM $\Delta\omega$ at $t = 100ns$ for the peaks in (a) and (b), respectively.*

phonon interference yields transmission antiresonance (zero-transmission dip) for THz phonons, traversing IPM. The random distribution of the defects in the IPM plane and the anharmonicity of atom bonds do not deteriorate the antiresonance [Han et al. (2014)]. The assisted laser Molecular Beam Epitaxy (MBE) have achieved atomically sharp interfaces in a superlattice [Ravichandran et al. (2014)] and can hence provide a possible experimental implementation for the proposed nanocapacitor since this technique can reach the resolution of a single unit cell in the lattice. In the molecular dynamics (MD) simulations, we model the covalent Si:Si/Ge:Ge/Si:Ge interactions by the Stillinger-Weber (SW) potentialStillinger and Weber (1985b). which includes both the two- and three-body potential terms. All our MD simulations were performed with the LAMMPS code packagePlimpton (1995).

4.3 Results and Discussions

4.3.1 Linewidth narrowing by adiabatic cooling

We first study the storage of coherent phonons by cooling the nanocapacitor initially thermalized at room temperature, implemented by MD simulations. Two heat sinks are coupled to the capacitor on the two facets of the mirrors, as shown in Fig. 4.1(b). The phonons, leaving the capacitor, are dissipated once entering the sinks, which are modeled by the Langevin heat bath, providing the effects of inelastic scattering on phonon transport. The capacitor was initially thermalized homogeneously at $T = 300$K to ensure that the material approaches the state of energy equipartition. The classical approximation remains relevant for Si at $T = 300\text{K} \approx 1/2\Theta_D$, where $\Theta_D = 645$K is the Debye temperature of Si. In Fig. 4.2(a) and (b), the power spectral density of atomic kinetic energy in the capacitor is shown, which was calculated from the windowed Fourier transform to demonstrate that all phonon modes were excited. Then the temperature of the heat sinks was set below 40 K to cool down the capacitor. The switch on of the heat sinks takes only a few pico- seconds, during which the phonons present in the capacitor have no time to escape, which corresponds to an "adiabatic cooling" process. Note that the switch-on of the heat sinks takes only few picoseconds, during which the phonons present in the capacitor have no time to escape, which corresponds to an “adiabatic cooling” process. In Fig. 4.2, the linewidth narrowing at zero temperature of the heat sinks is shown to clarify the physical mechanism.

In order to realize the phonon confinement in our interference capacitor under realistic conditions, we use heat sinks with low temperature close to or higher than the temperature of liquid helium to cool the capacitor. We follow the same protocol to pump the phonons into the capacitor as in the paper: the capacitor was first thermalized homogeneously at $T_R = 300$K to ensure that the material approaches the state of energy equipartition. Then the thermalization was stopped and the heat sinks with temperature T_s =10K, 20K, 30K or 40K were used to cool the capacitor. After $100ns$ of cooling, we can still observe a pronounced phonon confinement at the resonant mode for T_s =10K and 20K, as shown in Fig. 4.3. The localized phonons have an equivalent temperature of $T_c = \hbar\omega/k_B = 303$K, where $\hbar$ is the reduced Planck constant and k_B is the Boltzmann constant. When the heat sink temperature T_s is much lower than T_R, the phonon-phonon interaction between the confined phonons and the incoming sink phonons is weak enough so that the phonon confinement in the capacitor remains pronounced. At higher temperatures such as 30K and 40K, the phonon confinement starts to be smeared out. This is probably due to stronger anharmonic phonon interactions between the localized mode and the phonons from the heat sink. In practice, liquid helium (at ~ 4 K) can be used for the heat sinks and Dewar flasks can be considered to prevent heat conduction

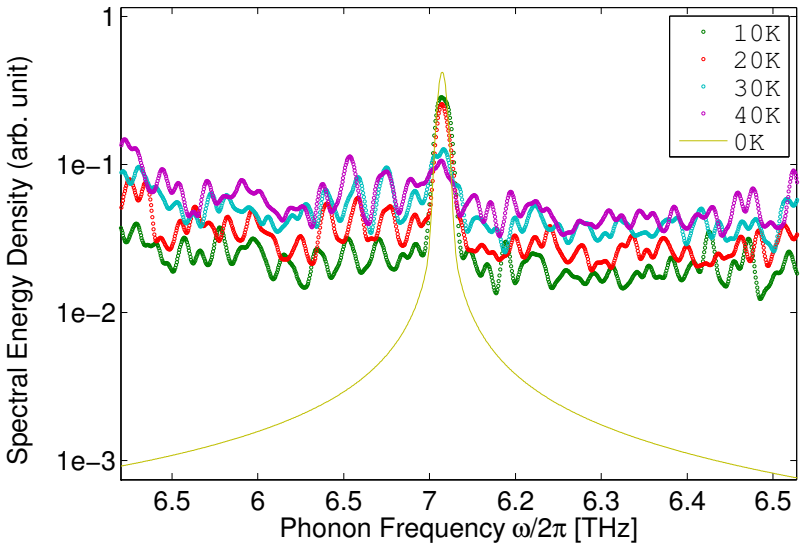

Figure 4.3: *Power spectral density of the phonon energy in the capacitor initially thermalized at $T = 300K$ after 100 ns from the cooling onset by using heat sinks with temperatures T_s =10K, 20K, 30K or 40K. For comparison, the power spectral density of the capacitor coupled to a heat sink at absolute zero temperature is also plotted.*

and radiation from the free side surfaces in experimental implementations of the interference phonon cavity.

We have found that the nanocapacitor can function in two regimes: in a dual-mode regime and in a single-mode regime, depending on the aspect ratio of the capacitor p defined as $p = L_x/L_z = L_y/L_z$. For a quasi-one-dimensional capacitor with small aspect ratio $p \approx 1/4$, after $t = 5$ns of cooling we notice the linewidth narrowing at the frequencies $\omega_1/2\pi = 3.5$THz and $\omega_2/2\pi = 6.31$THz, which corresponds to the dual-mode regime with the storage of both transverse and longitudinal coherent lattice waves. The power spectral density for all phonon modes in the capacitor has decayed during the cooling process by over two orders of magnitude except for the two modes, as shown in Fig. 4.2(a) and (c). With a cooling duration of $t = 100$ns, which is very long for an atomic system, the coherent phonon peaks at $\omega_{1,2}$ show the decrease of only 10% as $t = 5$ns while all the other phonon modes have practically escaped the capacitor. This high monochromatic quality makes the interference cavity an ideal candidate for a coherent phonon source - the phonon laser[Grudinin et al. (2010); Beardsley et al. (2010); Maryam et al. (2013); Fainstein et al. (2013)]. The single-mode regime was achieved in a 3D capacitor with $p \approx 1$: after the same cooling process, only the longitudinal mode at $\omega_2/2\pi = 6.31$THz is stored, as shown in Fig. 4.2(b) and (d). Since the capacitor phonons are in a

single-mode state at low temperature of the heat sinks, the phonon number n_C and total elastic lattice energy E_{el} are related as $E_{el} = \hbar\omega_2(n_C + \frac{1}{2})$. We thus obtain the phonon number $n_C \approx 57,000$ for $E_{el} = 77.8$eV stored in the present nanocapacitor. For a large phonon number $n_C \gg 1$, the classical equations of motion are valid for ensemble averaging in the semiclassical limit.

4.3.2 Phonon reflection on the mirror

By MD-based phonon wave-packet (WP) method [Han et al. (2014)], we computed the energy transmission coefficient $\alpha(\omega, \xi)$ for the Si:Ge interference mirror, for transverse and longitudinal waves. To compute $\alpha(\omega, \xi)$, we excited a 3D Gaussian wave packet centered at the frequency ω and wave vector $\mathbf{k}$ in the reciprocal space and at $\mathbf{r}_0$ in the real space, with the spatial width (coherence length) ξ. The WP generation was performed by assigning the displacement for the atom i:

$$\mathbf{u}_i = A\mathbf{e}_i(\mathbf{k})e^{i[\mathbf{k}\cdot(\mathbf{r}_i-\mathbf{r}_0)-\omega t]}e^{-[\mathbf{r}_i-\mathbf{r}_0-v_g t]^2/4\xi^2}, \tag{4.1}$$

where A is the wave amplitude, $\mathbf{e}_i(\mathbf{k})$ is the phonon polarization vector, v_g is the phonon group velocity at the WP center frequency ω. The WP energy transmission coefficient $\alpha(\omega, \xi)$ is defined as the ratio between the energy carried by the transmitted and initial wave packets, which are centered at the given phonon mode $(\omega, \mathbf{k})$ with the spatial extent ξ. It is determined by the convolution of the transmission coefficient for the plane wave $\alpha_{\text{pw}} = \alpha(\omega, \infty)$, described in Ref. [Han et al. (2014)], with a Gaussian WP in frequency domain with the full width at half maximum (FWHM) $\Delta\omega = v_g/(2\xi)$:

$$\alpha(\omega, \xi) = \int_{-\omega_{\max}}^{\omega_{\max}} \alpha_{\text{pw}}(\omega')e^{-\frac{(\omega-\omega')^2}{2\Delta\omega^2}} \frac{\mathrm{d}\omega'}{\Delta\omega\sqrt{2\pi}}. \tag{4.2}$$

We have confirmed that the phonon modes, trapped in the capacitor after the cooling, correspond to the antiresonance modes of the IPM, as shown in Fig. 4.4(a) and (b). Therefore the capacitor phonons, initially excited by the external thermal or optical pumping, will experience linewidth narrowing during the cooling and concentrate at the transverse and longitudinal modes, with ω_1 and ω_2 eigenfrequencies respectively, since the interference mirrors totally reflect the antiresonance-mode phonons but allow the other phonons to transmit.

4.3.3 Phonon localization

The interference cavity carries out significant phonon confinement through the two-path interference in the IPMs. For a quantitative measure of phonon confinement, we introduce the Relative Phonon Participation Number (RPPN) $\mathcal{N}$:

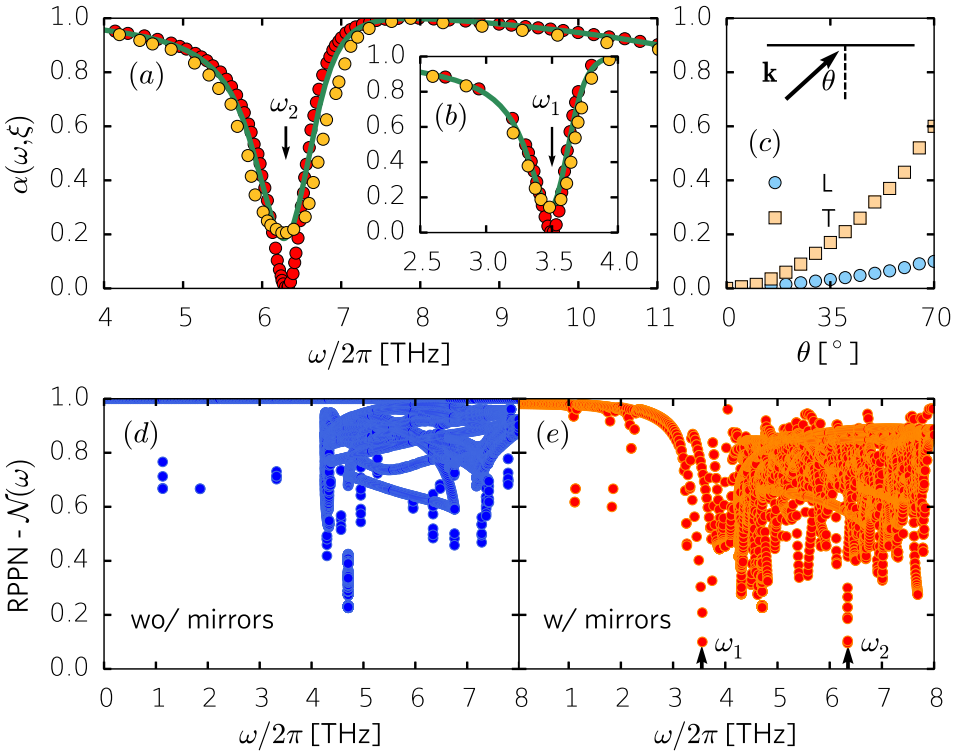

Figure 4.4: *(a) and (b): Spectra of the energy transmission coefficient $\alpha(\omega,\xi)$ through interference mirror obtained by MD simulations for phonon WPs with different coherence lengths ξ in Eq. (4.1) and incidence angles θ. Transmission of normally incident WP ($\theta = \frac{\pi}{2}$) with long coherence length $\xi = 100\lambda_c$ (plane-wave approximation, red circles) and with short coherence length $\xi = 8\lambda_c$ (yellow circles) in comparison with the convolution of the plane-wave transmission spectrum $\alpha_{pw}(\omega)$ with a frequency-domain Gaussian WP (green curve) with longitudinal (a) and transverse (b) polarization. (c): Transmission of the oblique-incident WP ($\theta < \frac{\pi}{2}$) at the antiresonances $\omega = \omega_{1,2}$ for transverse (T) and longitudinal (L) polarizations. Relative phonon participation number (RPPN) $\mathcal{N}(\omega)$, Eq. (2), in a mirror-free Si sample (d) and in a capacitor formed by two IPMs (e).*

$$\mathcal{N}\left(\begin{smallmatrix}\mathbf{k}\\ \omega\end{smallmatrix}\right) = \left(\sum_{i=1}^{N}\mathcal{E}_i\left(\begin{smallmatrix}\mathbf{k}\\ \omega\end{smallmatrix}\right)\right)^2 / N\sum_{i=1}^{N}\left[\mathcal{E}_i\left(\begin{smallmatrix}\mathbf{k}\\ \omega\end{smallmatrix}\right)\right]^2, \tag{4.3}$$

where $\mathcal{E}_i\left(\begin{smallmatrix}\mathbf{k}\\ \omega\end{smallmatrix}\right)$, the mean kinetic energy of atom i for a normal mode $\left(\begin{smallmatrix}\mathbf{k}\\ \omega\end{smallmatrix}\right)$ defined by the wave vector $\mathbf{k}$ and the frequency ω, can be found from the corresponding eigenvector $\boldsymbol{\epsilon}_i(\mathbf{k})$, N is the total atom number in the system. $\mathcal{N} \in [0,1]$ measures the fraction of atoms participating in the normal vibration mode $\left(\begin{smallmatrix}\mathbf{k}\\ \omega\end{smallmatrix}\right)$, cf. Ref. [Bell and Dean (1970)]. Figs. 4.4(d) and (e) present a comparison between the computed $\mathcal{N}(\omega)$ in a mirror-free Si sample and in a capacitor formed by two IPMs. Most of the modes in the spectral range $\omega/2\pi \in [0,8]$THz are propagative since $\mathcal{N} \gtrsim 0.5$ is characteristic for the typical extended phonon modes in a perfect crystal [Bell and Dean (1970)]. But in the the sample with two atomic-scale interference mirrors, confined modes with very low $\mathcal{N}(\omega)$ (< 0.1) are observed at $\omega_1/2\pi = 3.51$ THz and $\omega_2/2\pi = 6.3$ THz, which correspond exactly to the transverse and longitudinal antiresonance frequencies of the mirrors. These plots demonstrate the strong effect of an extremely small amount of Ge atoms, $\sim 0.7\%$, on the phonon confinement and explains the origin of the ultra-compactness of the proposed interference phonon cavity. We note that $\mathcal{N}\left(\begin{smallmatrix}\mathbf{k}\\ \omega\end{smallmatrix}\right)$ also describes phonon correlations in the system: It is the frequency-domain classical counterpart of the inverse time-domain second order phonon-phonon correlation function $1/g_{ph}^{(2)} = \langle b^\dagger b\rangle^2/\langle b^\dagger b^\dagger bb\rangle$ [Kabuss et al. (2012); Kepesidis et al. (2013)], where $b^\dagger$ and b are the creation and annihilation operators of the vibrational modes, in the quantum-mechanical description of phonon confinement and correlations in the considered interference cavity.

The two-color regime of the capacitor originates from the different dependence of the transmission coefficient $\alpha(\omega,\xi,\theta)$ on the WP incidence angle θ for the transverse and longitudinal phonons at their respective antiresonances $\omega = \omega_1, \omega_2$, as shown in Fig. 4.4(c). By modeling the oblique incidence of the WP (with $\theta < \frac{\pi}{2}$), we found that $\alpha_T(\omega_2,\xi,\theta) > \alpha_L(\omega_1,\xi,\theta)$ for the same θ, indicating that the resonant transverse phonon has a higher transmittance through the mirror than the longitudinal counterpart. Therefore, for a relatively large aspect ratio ($p \approx 1$), the transverse modes with relatively large incident angles are more susceptible to transmit through the mirrors. Hence after the cooling process, only the longitudinal modes remain in the capacitor, cf. Fig. 2(a) and 2(c). While for a small aspect ratio, $p \ll 1$, when the system becomes effectively one-dimensional, both the transverse and longitudinal resonance vibrational modes are confined in the nanocapacitor, cf. Fig. 2(b) and 2(d). The two-color operation may pave the stage for the (double-) single phonon source, which is crucial for quantum phonon computing.

The confining effect of acoustic modes could also be found in the sub-THz

acoustic nanocavity [Trigo et al. (2002); Huynh et al. (2006)] placed between two Bragg reflectors (BRs). The nanocavity mode corresponds to the Fabry-Pérot (FP) resonance in the inhibited bandgap background of the surrounding BR's [Trigo et al. (2002); Lanzillotti-Kimura et al. (2007)]. Such FP mode gives rise to the total transmission peak lying inside the wide phonon bandgap, which can be identified as a "resonance tunneling". In the present paper, the proposed interference phononic capacitor has several major differences and thus novelties in comparison with the acoustic nanocavity placed between two Bragg reflectors:

- BRs are made of a stack of semiconductor layers of several dozens of nm of total thickness, while the proposed interference mirrors in the interference capacitor require only single atomic planes. The strong phonon-confining capability of such interference phonon mirrors, as demonstrated in Fig. 4.4(c) and (d) in the paper, enables potential realization of the ultra-compact nanophononic devices.
- While the frequency of the FP mode inside the bandgap is well defined, its wavevector $\mathbf{k}$ is a complex number, making it difficult to define the wavelength λ of the evanescent cavity mode. The interference cavity phonons are, in contrast, lattice vibrational eigenmodes with well defined wave vector $\mathbf{k}$ and group velocity $v_g(\mathbf{k}, \omega)$ in the phonon passband thus enabling coherent phonon emission (phonon lasing) from the interference cavity.
- The FP mode in the acoustic cavity has a relatively short lifetime ($\sim$ a few nanoseconds) due to its evanescent-wave nature, while the interference cavity phonons can be stored for more than hundreds of nanoseconds. Thus the proposed interference cavity can be considered as a mono- or duo-chromatic phonon reservoir.

To understand better the generation mechanism of the capacitor phonons, we studied the evolution of lattice dynamics in the nanocapacitor after its excitation in the form of phonon WP. We demonstrate through the mapping of the power spectral density of atomic kinetic energy in the capacitor, shown in Fig. 4.5, that the Gaussian phonon WP, initially centered at $(\omega, \mathbf{k})$, finally transforms into *monochromatic* standing wave composed of the two plane waves with the same frequency ω and opposite wave vectors $\pm\mathbf{k}$ along the normal to the mirrors. Between the free side surfaces of the capacitor, a standing wave with the wavelength $\lambda = 2L_x^c$ of the sinusoidal envelope is formed. All the other frequency components leak out from the capacitor and are absorbed by viscous material at the two ends of the capacitor. In practice, the pump-probe optical technique [Huynh et al. (2006); Lanzillotti-Kimura et al. (2007)] can be used to excite the capacitor phonons, and the considered WP excitation mimics this

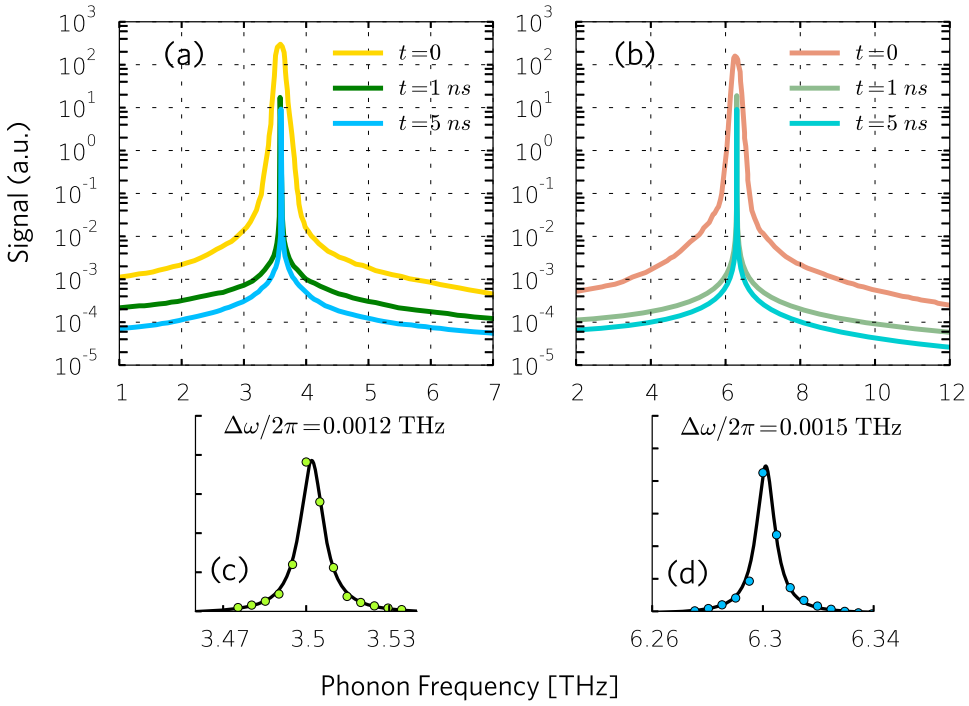

Figure 4.5: *Power spectral density of atomic kinetic energy in the capacitor after excitation of the transverse (a) and longitudinal (b) phonon WP as a function of time delay t. The peaks centered at $\omega_{1,2}$ demonstrate a continuous linewidth narrowing as a function of t. At $t = 5ns$, the widths narrow down to $\Delta\omega_1/2\pi = 1.2\times10^{-3}$ THz and $\Delta\omega_2/2\pi = 1.5\times10^{-3}$ THz, which correspond to the cavity Q factors of $Q_1 = 2916$ and $Q_2 = 4208$, respectively. Gaussian fit of the capacitor phonon peaks to measure FWHM $\Delta\omega$ at $t = 5ns$ for the transverse (c) and longitudinal (d) modes.*

technique.

Another possibility to store coherent phonos in the interference capacitor is to implement a local excitation of the capacitor in the form of phonon wave packet. Atomic kinetic energy E_k in the initial 3D phonon WP is shown in Fig. 4.6 in a cutting plane (a) and in nanocapacitor (b). The final coherent standing-wave phonons with well defined wave-vectors $\pm\mathbf{k}$ and wavelength λ_c confined in the capacitor are shown in a cutting plane in Fig. 4.6(c) and in 3D structure in Fig. 4.6(d). Here several cutting planes in the capacitor are shown to allow for an internal view of phonon energy distribution. Lighter areas present higher E_k.

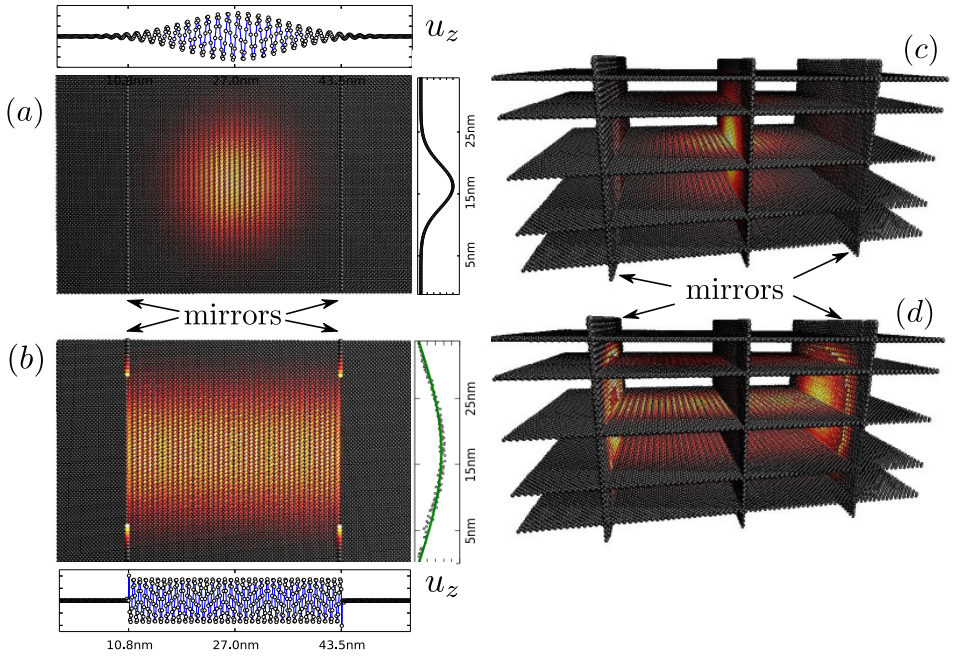

Figure 4.6: *Atomic kinetic energy E_k in the nanocapacitor. Initial 3D phonon wave packet in a cutting plane (a) and in nanocapacitor (b). The final coherent standing-wave phonons with well defined wave-vectors $\pm\boldsymbol{k}$ and wavelength λ_c confined in the capacitor in a cutting plane (c) and in 3D structure (d). Panels show the atomic displacements along the x and z directions in the initial WP (a) and in final standing wave (c).*

4.3.4 Controllabe phonon emission

We now turn to the controllable emission of the coherent phonons from the capacitor, which can also be considered as discharging of the phonon reservoir. Figure 4.7 shows the shift of the interference antiresonance spectral loci for transverse and longitudinal phonons caused by the uniaxial stress σ_{zz}, applied in the $\langle 001 \rangle$ direction to the interference cavity as shown in Fig. 4.1(b). The resulting strain ϵ produces the change in the local force constants between Ge and Si atoms in the mirrors, which shifts the antiresonance frequencies $\omega_{1,2}$ of the capacitor, according to the value of the Grüneisen parameter of Si. Through such a mechanism, we are able to emit coherent phonons by applying tunable reversible uniaxial stress at the tips of the device The stored coherent phonons are emitted from the capacitor with the group velocity $v_{gz}(\omega, k_z) = \partial\omega/\partial k_z$ of the phonon mode. Once the external stress is released, the phonon emission is switched off due to the recovery of the interference mirrors back to the original antiresonance frequencies. Therefore, the directional and coherent phonon emission from the interference cavity, which can be considered as phonon lasing [Vahala et al. (2009); Mahboob et al. (2013)], is flexibly switched by the

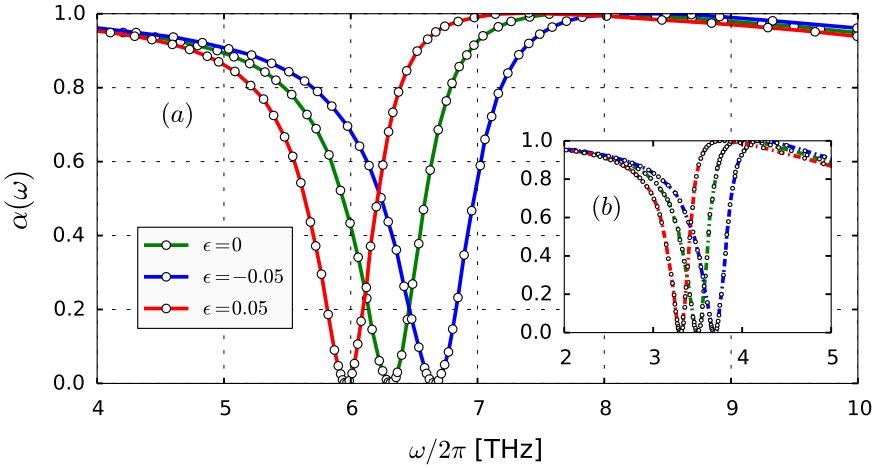

Figure 4.7: *Shift of interference antiresonance spectral loci caused by tunable strain ϵ in the capacitor. Antiresonance frequency shifts for longitudinal (a) and transverse (b) plane waves, normally incident on interference mirror. Interference cavity is exposed to the uniaxial strain ϵ in the $\langle 001 \rangle$ direction. Negative strain $\epsilon < 0$, corresponding to a compression of the cavity, results in a blue shift of mirror's antiresonance frequencies in accordance with positiveness of the Grüneisen parameter. In a similar manner, positive strain red-shifts antiresonance frequencies.*

external stress. According to Fig. 4.2, the *two-color* phonon lasing of both transverse and longitudinal coherent lattice waves can be realized from the dual-mode nanocapacitor. The swift discharging of the nanocapacitor enables promising applications in phonon computing and nanoscale memories.
The phonon capacitor may be a new component for constructing and controlling macroscopic artificial quantum systems based on sound. The swift discharging of the nanocapacitor and the two-color phonon emission may also be relevant for quantum computing applications: to inhibit decoherence and to yield single phonons. Moreover, phonons from the nanocapacitor are easily coupled with optical and electronic systems, which enables the phonon capacitor to play a potential role in a hybrid quantum computing architecture. It is noteworthy in this connection that high sensitivity of phonon interference antiresonance to the applied forces and deformations makes it possible to use the nanocavity also as a nano-detector of atomic-scale displacements and strains in the surrounding material, like single molecule can be used as a detector of nanomechanical motion [Puller et al. (2013); Tian et al. (2014)].

4.4 Conclusions

In conclusion, we introduce a novel ultra-compact interference cavity for coherent phonons formed by high-finesse interference mirrors based on atomic-scale semiconductor metamaterials. Through MD simulations We show that the

nanocavity stores monochromatic THz lattice waves, which can be used for the phonon lasing - the emission of coherent phonons. Either one- or two-color phonon lasing can be realized depending on the geometry of the nanodevice. Coherent phonon storage can be achieved by cooling the nanocavity initially thermalized at room temperature or by the pump-probe technique. The confined modes can be released from the nanocavity by applying tunable reversible stress which results in the emission of coherent THz acoustic beams.

Chapter 5

Harmonic Phonon Interferences Reduce Heat Conduction

We investigate the role of two-path destructive phonon interference induced by long-range interatomic forces on the thermal conductance and conductivity of a silicon-germanium alloy by atomistic calculations. The thermal conductance across a germanium atomic plane in the silicon lattice is substantially reduced by the destructive interference of the nearest-neighbour phonon path with a direct path bypassing the defect atoms. Such an interference causes a fivefold reduction in the lattice thermal conductivity in a SiGe alloy at room temperature. We demonstrate the predominant role of harmonic phonon interferences in governing the thermal conductivity of solids by suppressing the inelastic scattering processes at low temperature. Such interferences provide a "harmonic resistive" mechanism to explain and control heat conduction through the coherent behaviours of phonons in solids.

5.1 Introduction

Destructive interference between waves traversing laterally-inhomogeneous interface can result in their total reflection. For instance, the enhanced electromagnetic reflection found in metafilms embedded with asymmetrical split-ring arrays [Fedotov et al. (2007)] and in stereometamaterials [Liu et al. (2009)] has offered the prospect of a multitude of applications as quantum optics [Altewischer et al. (2002)] and negative refraction [García-Meca et al. (2009)]. As another example of destructive interference in optics, two-photon interference can result in a total cancellation of the photon output because of the coalescence of the two single photons, which was first observed by Hong et al. [Hong et al. (1987)]. This interference effect occurs because two possible photon paths interfere destructively, which produces the famous Hong-Ou-Mandel

(HOM) dip in the detection probability of the output photons. The HOM dip has since been demonstrated in both the optical [Beugnon et al. (2006); Santori et al. (2002)] and microwave [Wang et al. (2012)] regime. Similar destructive interference effect which results in the total reflection can be also realized in an acoustic system [Fellay et al. (1997); Kosevich (1997)].

For sound waves, the enhanced acoustic reflection was first described in Ref.Fellay, Gagel, Maschke, Virlouvet, and Khater (1997) and Ref.Kosevich (1997) independently. Ref.Fellay, Gagel, Maschke, Virlouvet, and Khater (1997) drew an analogy between electron and phonon scattering and calculated the phonon transmission with an asymmetric profile through a one-dimensional oscillator chains connected in parallel. Ref.Kosevich (1997) interpreted the anomalous reflection of an acoustic wave by a two-dimensional crystal defect. as the destructive interference between two phonon paths: through the nearest-neighbour bonds and through the non-nearest-neighbour bonds which couple directly atomic layers adjacent to the defect plane. Phonon interference antiresonances can be advantageous in manipulating the thermal transport in nanomaterials. A better understanding of phonon dynamics is crucial in improving the thermoelectric efficiency. The figure of merit zT for thermoelectric conversion efficiency can be expressed as $zT = \sigma S^2 T/\kappa$, where S, T, σ, and κ are the Seebeck coefficient, temperature, electrical, and thermal conductivities, respectively. Thus, a low thermal conductivity is favorable for good thermoelectric performance. Recent efforts concentrated on reducing the thermal conductivity κ via nanostructured materials with superlattices [Chowdhury et al. (2009); Kim et al. (2006)] and embedded nanoparticles [Mingo et al. (2009); Pernot et al. (2010); Chen et al. (2013)]. Reducing κ is often achieved by enhancing phonon scattering rate and thus diminishing the mean free path (MFP), which belongs to a particle description. Nevertheless, the role of destructive phonon-wave interferences remains to be well understood in the tailoring of thermal transport in a wave picture. Recently, coherent phonon scattering has been observed in semiconductor superlattices with high interface qualities [Luckyanova et al. (2012); Ravichandran et al. (2014)]. A phononic metamaterial that allows for manipulating and confining the flow of thermal energy at the atomic scale was proposed by exploiting the two-path phonon interference on the internal interfaces embedded with defect-atom arrays [Han et al. (2014); Han et al. (2015)].

Here, we investigate the role of two-path destructive phonon interference induced by long-range interatomic forces on the thermal conductance and thermal conductivity of a SiGe alloy by atomistic calculations. The thermal conductance across a Si atomic metaplane entirely substituted with Ge atoms is strongly reduced due to the destructive interference of the nearest-neighbour Si-Ge phonon path with a direct Si-Si path bypassing the Ge atoms. Such a destructive interference causes a fivefold reduction of the lattice thermal con-

ductivity of a $Si_{0.5}Ge_{0.5}$ alloy. The thermal conductivity is overcompensated by the increase of the Grüneisen parameters at the Brillouin zone center, in spite of the enhanced acoustic phonon group velocities. Lattice dynamics analysis shows a strong localization due to the phonon interference. The harmonic phonon interferences persist to dominate the behaviour of the thermal conductivity of the alloy at the low temperature of 100 K where the inelastic scattering processes are substantially suppressed.

5.2 Atomistic Scheme

The atomistic scheme of two-path phonon interference is illustrated in the insets of Fig. 5.1. In most lattices where the atoms are mainly coupled to each other through the nearest-neighbour bonds, the propagation path of phonon is restricted to the host-guest atom bonds when encountering an impurity atom. An additional phonon path becomes available when considering the second-nearest-neighbor bonds between the host atoms on the two sides of the impurity atom in addition to the first path through the nearest-neighbor bonds linking the host and adjacent impurity atoms, as shown in Fig. 5.1. Destructive interferences will emerge due to the opening of the second phonon path that couples directly crystal layers adjacent to the defect atoms. We first investigate the intriguing role of such phonon interferences in the interfacial thermal conductance by using molecular dynamics (MD) modeling of the transmission of phonon wave-packets (WP) propagating in a silicon (Si) host lattice through a defect atomic plane of germanium (Ge), as shown in inset (**i**) of Fig. 5.1. Such WP modeling provide the per-phonon-mode energy transmission coefficient [Han et al. (2015)]. The spatial width l (coherence length) of the WP is taken much larger than the wavelength λ_c of the WP central frequency, corresponding to the plane-wave approximation [Han et al. (2014)]. The MD simulations were performed with the LAMMPS code package [Plimpton (1995)]. The covalent Si:Si/Ge:Ge/Si:Ge interactions are modeled by the Stillinger-Weber (SW) potential [Stillinger and Weber (1985b)].

5.3 Results and Discussions

5.3.1 Harmonic force constants determination from density functional perturbation theory (DFPT) calculations

We calculate the harmonic interatomic force constants (IFCs) of silicon and silicon-germanium alloy from density functional perturbation theory (DFPT) calculations. DFPT calculations were carried out using the quantum chemistry DFT code Quantum ESPRESSO [Giannozzi et al. (2009)]. The calculation was conducted for a $2 \times 2 \times 2$ supercells of bulk silicon, germanium and a $Si_{0.5}Ge_{0.5}$

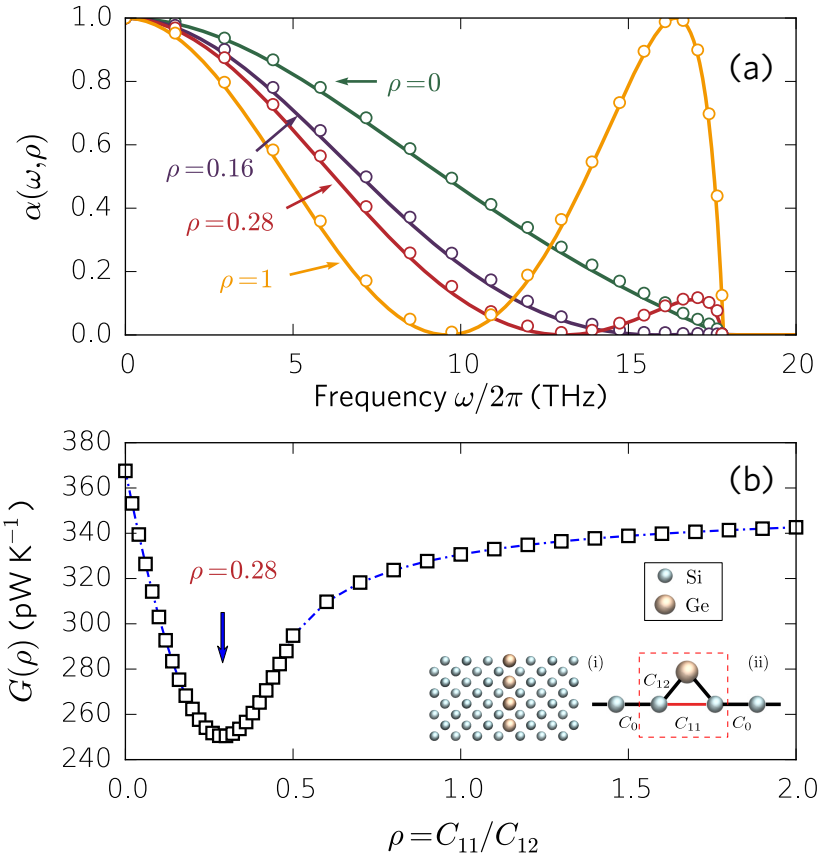

Figure 5.1: *(a) Spectral transmission coefficients $\alpha(\omega,\rho)$ predicted by MD simulations (open circles) of a Si host crystal with a single atomic layer of Ge atoms and by Green's Function calculations of an equivalent quasi-1D model (solid lines). Only the longitudinal polarization is shown for the MD prediction. (b) Thermal conductance $G(\rho)$ versus the relative strength of the second nearest-neighbour bond ρ at $T = 300$ K. Inset (**i**): host silicon lattice with a single $\langle 001\rangle$ atomic layer of guest Ge atoms. Inset (**ii**): quasi-1D tight-binding model which incorporates the second nearest-neighbour bonds C_{11} bypassing the nearest-neighbour bonds C_{12} between the host atom with mass m_1 and the guest atom with mass m_2. The host atoms are coupled through the nearest-neighbour bonds C_0. Black (red) sticks represent the NN (second NN) bonds. The region inside the red dashed rectangle is the scattering region.*

containing 64 atoms by the plane-wave basis method implemented in the Quantum Espresso package. We adopted both generalized gradient approximation (GGA) for the exchange-correlation functional to study pseudopotential-dependent phonon properties. The parameterizations of Perdew-Burke-Ernzerhof were selected for GGA. The cutoff energies for plane-wave expansion was set to 60 Rydberg ($\approx$ 816 eV) for GGA. A Monkhorst-Pack k-point grid of 4 $\times$ 4 $\times$ 4 was used to achieve the desired accuracy. Constraints due to translational invariance and other symmetries were employed to identify the minimum number of independent IFCs that needed to be computed. We have set the range of harmonic IFCs to fice nearest neighbor shells. This results in 17 independent harmonic IFCs. The IFCs were fitted with the ALAMODE package [Tadano et al. (2014)].

5.3.2 Phonon transmission

The spectral transmission coefficients $\alpha(\omega, \rho)$ retrieved from MD simulations of a Si host crystal with a single atomic layer of Ge atoms are illustrated in Fig. 5.1(a). ρ is defined as the ratio of the second nearest-neighbour (NN) force constant C_{11} of Si atoms and the first-NN force constant C_{12} between Si and Ge atoms, $\rho = C_{11}/C_{12}$. ρ measures the relative strength of the second NN interaction versus the NN force. Our Density Functional Perturbation Theory (DFPT) calculations show that $\rho \approx 5.7\%$ in natural SiGe alloys where the nearest neighbour (NN) bond is $C_{12} = 3.21$ eV/Å^2 (3.51 eV/Å^2) for the Si-Si (Si-Ge) atom pair, and the second-NN bond strength is $C_{11} = 0.187$ eV/Å^2 (0.192 eV/Å^2) for the Si-Si (Ge-Ge) pair. Empirical SW potential reproduces relatively precise NN bonds but its second NN bonds are negligible. When a single phonon path is available for phonons crossing the Ge atomic plane, i.e. $\rho = 0$, the transmission coefficient $\alpha(\omega, \rho = 0)$ monotonously decays as frequency increases with $\alpha(\omega = 0) = 1$ and $\alpha(\omega = \omega_{\max}) = 0$. A relatively weak second NN interaction $\rho = 0.16$ reduces the transmission on the whole spectrum but the effect is especially strong at short wavelengths $\alpha(\omega \geq 15$ THz$) \approx 0$. Such a remarkable drop in the transmission coefficient is due to the destructive interference between the two phonon paths: through the nearest-neighbor Si-Ge bonds and through the non-nearest-neighbor Si-Si bonds which couple directly atomic layers adjacent to the defect plane. For a larger $\rho = 0.28$, a total reflection antiresonance emerges $\alpha(\omega = 13$ THz$) = 0$ followed by a local transmission maximum. When ρ further strengthens, the total reflection shifts to longer wavelengths and the local maximum finally becomes a total transmission.

Fig. 5.1(b) shows the thermal conductance G versus ρ at $T = 300$ K. $G(\rho)$ is

calculated by following the Landauer-like formalism

$$G(\rho) = \int \sum_{\nu} \hbar\omega_{\mathbf{q}} v_{\mathbf{q}}^{g,\perp} \alpha(\omega,\rho) \frac{\partial}{\partial T} n_{\mathrm{BE}}(\mathbf{q},T) \frac{\mathrm{d}\mathbf{k}}{(2\pi)^3}, \tag{5.1}$$

$\mathbf{q}$ denotes the phonon mode $(\mathbf{k},\nu)$ where $\mathbf{k}$ is the wave vector and ν is the phonon polarization. $v_{\mathbf{q}}^{g,\perp}$ is the group velocity component perpendicular to the Ge atomic plane. $n_{\mathrm{BE}} = [\exp(\hbar\omega_{\mathbf{q}}/k_{\mathrm{B}}T)-1]^{-1}$ is the Bose-Einstein distribution of phonons, where T refers to the mean temperature of the system, k_B and $\hbar$ represent the Boltzmann and the reduced Planck's constants, respectively. The thermal conductance G first decreases as the second phonon path strengthens, since the opening of the second phonon path through the second NN bonds C_{11} interferes destructively with the first path through the NN bonds C_{12}, which induces a maximum reduction in G of 33% at $\rho = 0.28$. G then starts to increase as the second NN bond further strengthens, due to the raised phonon transmission at high frequencies, c.f. Fig. 5.1(a). The destructive interference is compensated by the very strong second phonon path at large ρ. To further understand the phonon antiresonances caused by the interference between two phonon channels, we use an equivalent tight-binding model of a monatomic quasi-1D lattice of coupled harmonic oscillators, depicted in the inset (**ii**) of Fig. 5.1. The interatomic bonds could be adjusted to the same as in the Si-Ge system to allow for a direct comparison. The phonon transmission is calculated by atomistic Green's Function (AGF) and the thermal conductance can be obtained by following the Landauer-Büttiker formula:

$$G = \int_0^{\omega_{max}} \Xi(\omega) \frac{\partial}{\partial T} n_{\mathrm{BE}} \hbar\omega \frac{d\omega}{2\pi} \tag{5.2}$$

where ω and ω_{max} are the energy and the Debye frequencies. The transmission $\Xi(\omega)$ is obtained from a nonequilibrium Green's function approach Mingo and Yang (2003). as $\mathrm{Tr}[\Gamma_L G_s \Gamma_R G_s^+]$. The advanced and retarded Green functions G_s^+ and G_s can be deduced from $G_s = \left[(\omega + i\Delta)^2 I - K_s - \Sigma_L - \Sigma_R\right]^{-1}$ where Δ is an infinitesimal imaginary part that maintains the causality of the Green's function and $\Sigma_L = K_{ab} g_L K_{ab}^\dagger$, $\Sigma_R = K_{ab} g_R K_{ab}^\dagger$ are the self-energies of the left and right leads. the "†" exponent indicating the Hermitian conjugation. The leads refer to the host lattice of semi-infinite chains. Finally, g_L and g_R refer to the surface Green's functions of the left and the right leads, while K_s and K_{ab} are the force constant matrices derived from the potential, for the scattering region and between neighboring leads, respectively (see inset (**ii**) of Fig. 5.1). The expression of the transmission also includes $\Gamma_L = i(\Sigma_L - \Sigma_L^+)$ and $\Gamma_R = i(\Sigma_R - \Sigma_R^+)$. As shown in Fig. 5.1(a), the AGF prediction of the phonon transmission from the quasi-1D model agrees relatively well with that of the longitudinal phonons transmission from MD simulations in a Si-Ge lattice.

In the quasi-1D tight-binding model of the Fig. 5.1, the self-coupling matrix of

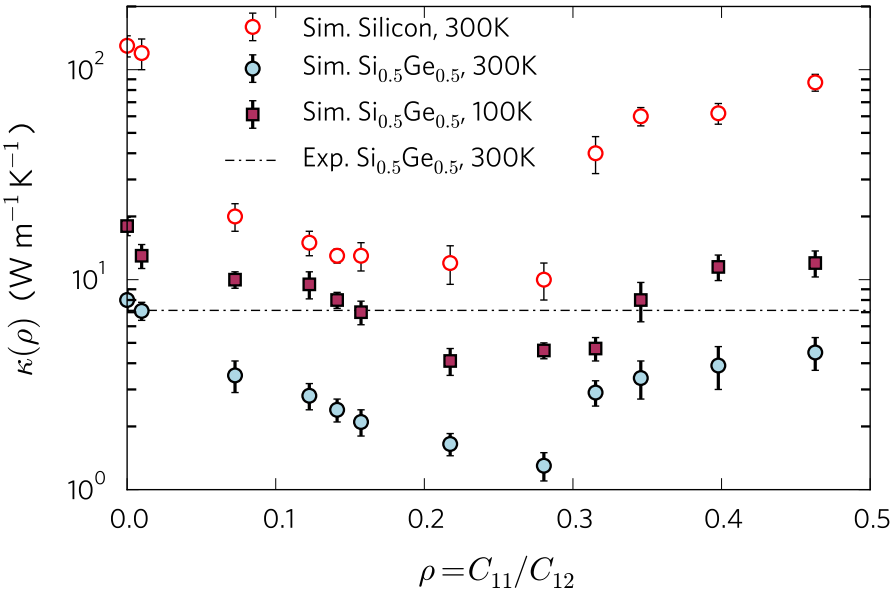

Figure 5.2: *Thermal conductivity κ of bulk Si at 300 K (red open circles) and $Si_{0.5}Ge_{0.5}$ alloy at 100 K (dark red squares) and at 300 K (blue solid circles) versus the relative strength of the second phonon path ρ. For the $Si_{0.5}Ge_{0.5}$ alloy, the thermal conductivities were obtained by averaging five different random atomic distributions. Our first-principle calculations show that natural SiGe alloys has $\rho \approx 5.7\%$.*

the scattering region K_s writes,

$$K_s = \begin{pmatrix} \frac{C_0+C_{11}+C_{12}}{m_1} & -\frac{C_{12}}{\sqrt{m_1 m_2}} & -\frac{C_{11}}{m_1} \\ -\frac{C_{12}}{\sqrt{m_2 m_1}} & \frac{2C_{12}}{m_2} & -\frac{C_{12}}{\sqrt{m_2 m_1}} \\ -\frac{C_{11}}{m_1} & -\frac{C_{12}}{\sqrt{m_1 m_2}} & \frac{C_0+C_{11}+C_{12}}{m_1} \end{pmatrix},$$

The matrix K^L_{ab} coupling the scattering region to the left lead writes,

$$K^L_{ab} = \begin{pmatrix} -\frac{C_0}{m_0} & 0 & 0 \end{pmatrix},$$

The matrix K^R_{ab} coupling the scattering region to the right lead writes,

$$K^R_{ab} = \begin{pmatrix} 0 & 0 & -\frac{C_0}{m_0} \end{pmatrix},$$

In the calculations, the NN bonds in the host lead C_0 equals to that in the scattering region C_{12}.

5.3.3 Alloy thermal conductivity

To demonstrate the effect of the two-path phonon interference on the lattice thermal conductivity of a bulk system, we calculated the thermal conductivity

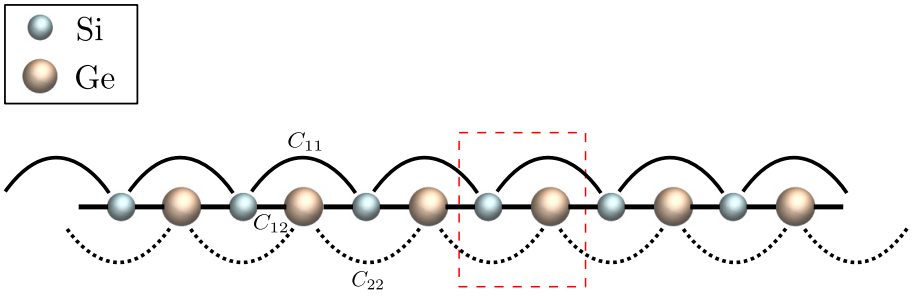

Figure 5.3: *Diatomic 1D model which incorporates the second nearest-neighbour (NN) bonds C_{11} and C_{22} bypassing the nearest-neighbour bonds C_{12} between the host atom with mass m_1 and the guest atom with mass m_2. The host atoms are coupled through the NN bonds C_{12}. The region inside the red dashed rectangle refers to the primitive cell.*

κ of bulk Si and a $Si_{0.5}Ge_{0.5}$ alloy versus the relative second-NN interaction ρ following the Green-Kubo technique in MD simulations, as shown in Fig. 5.2. Similar to the thermal conductance G, κ experiences a transition with a local minimum around $\rho = 0.28$. Surprisingly, even for a bulk Si crystal without any impurity, we observe a reduction of κ by one orders of magnitude from 115 $Wm^{-1}K^{-1}$ down to 12 $Wm^{-1}K^{-1}$ due to the openning and strengthening of the second phonon path. In the $Si_{0.5}Ge_{0.5}$ alloy, both the second-NN force constant C_{11} between Si atoms and those between Ge atoms C_{22} are taken into account in the MD simulation. By introducing nonnegligible second-NN bonds, the MD simulations show that the thermal conductivity of $Si_{0.5}Ge_{0.5}$ alloys is reduced below the experimental alloy limit of $\kappa \approx 7.14$ $Wm^{-1}K^{-1}$ [Wang et al. (2008)].

5.3.4 Phonon spectrum of of the diatomic 1D chain and the SiGe alloy

To understand the extraoridinarily low thermal conductivity due to the phonon interferences, we investigate the lattice dynamics of the $Si_{0.5}Ge_{0.5}$ crystal. The $Si_{0.5}Ge_{0.5}$ crystal has a zinc-blende lattice where one atom of the primitive unit cell is Si and the other is Ge. This $Si_{0.5}Ge_{0.5}$ crystal has a one-to-one correspondance with a 1D tight-binding model of diatomic chain of alternating Si and Ge atoms.

The diatomic 1D model which incorporates the second nearest-neighbour (NN) bonds is depicted in Fig. 5.3. The self-coupling matrix of the primitive cell K_s

writes,

$$K_s = \begin{pmatrix} \frac{2(C_{11}+C_{12})}{m_1} & -\frac{C_{12}}{\sqrt{m_1 m_2}} \\ -\frac{C_{12}}{\sqrt{m_2 m_1}} & \frac{2(C_{22}+C_{12})}{m_2} \end{pmatrix},$$

The matrix K_{ab}^L coupling the scattering region to the left lead writes,

$$K_{ab}^L = \begin{pmatrix} -\frac{C_{11}}{m_1} & -\frac{C_{12}}{\sqrt{m_1 m_2}} \\ 0 & -\frac{C_{22}}{m_2} \end{pmatrix},$$

The matrix K_{ab}^R coupling the scattering region to the right lead writes,

$$K_{ab}^R = \begin{pmatrix} -\frac{C_{11}}{m_1} & 0 \\ -\frac{C_{12}}{\sqrt{m_1 m_2}} & -\frac{C_{22}}{m_2} \end{pmatrix} = K_{ab}^{L\dagger},$$

Then the dynamical matrix of the chain writes,

$$D(k) = K_s + K_{ab}^L \mathrm{e}^{-ika_0} + K_{ab}^R \mathrm{e}^{ika_0},$$

where k is the wave vector along the chain axis and a_0 is the length of the unit cell.
At the Brillouin zone center where $k = 0$, the dynamical matrix reduces to

$$D(k=0) = 2C_{12} \begin{pmatrix} 1/m_1 & -1/\sqrt{(m_1 m_2)} \\ -1/\sqrt{(m_2 m_1)} & 1/m_2 \end{pmatrix}$$

At the Brillouin zone edge where $k = \pi/_0$, the dynamical matrix reduces to

$$D(k=\pi/a_0) = \begin{pmatrix} \frac{2C_{12}+4C_{11})}{m_1} & 0 \\ 0 & \frac{2C_{12}+4C_{22})}{m_1} \end{pmatrix}$$

Therefore, the frequency of the longitudinal acoustic branch $\omega_{\max}^{\mathrm{LA}} \propto \sqrt{2C_{12}+4C_{22}}$ and that of the longitudinal optical branch $\omega_{\max}^{\mathrm{LO}} \propto \sqrt{2C_{12}+4C_{11}}$.

Fig. 5.4(a) and (b) compare the phonon dispersions of the $Si_{0.5}Ge_{0.5}$ crystal without and with strong non-nearest neighbour interactions. The strong second phonon path raises the phonon frequencies at the Brillouin zone edges and thus enhances the group velocities of these phonon modes, especially the acoustic ones. In fact, an analytical calculation shows that at the Brillouin zone boundary, the frequency of the longitudinal acoustic branch $\omega_{\max}^{\mathrm{LA}} \propto \sqrt{2C_{12}+4C_{22}}$ and that of the longitudinal optical branch $\omega_{\max}^{\mathrm{LO}} \propto \sqrt{2C_{12}+4C_{11}}$, as shown in Fig. 5.4 (a) and (b). C_{22} is the second NN bond between Ge atoms and $C_{22} = C_{11}$ since Si and Ge can be considered as isotopes as a first approximation. It is clear that the major heat carriers, that are the transverse and longitudinal acoustic phonons, show larger group velocities for $\rho = 0.28$ than

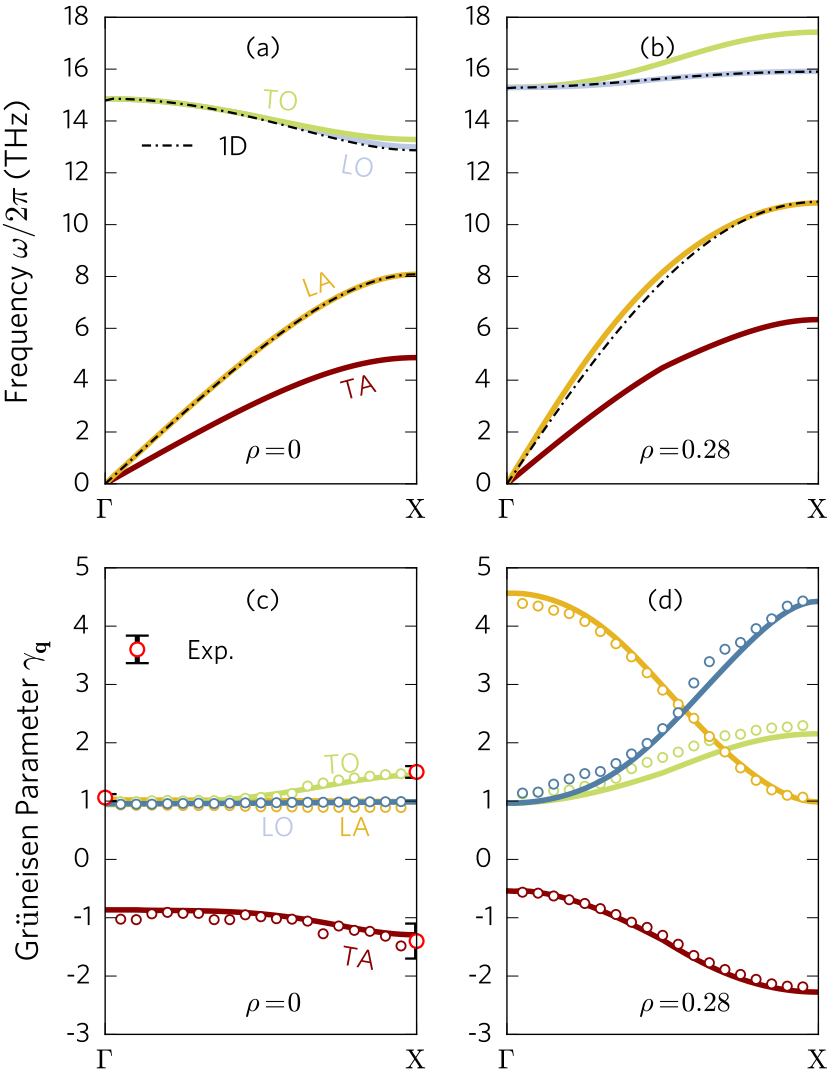

Figure 5.4: *Phonon band structure $\omega - \boldsymbol{k}$ in the $\langle 001 \rangle$ direction of a $Si_{0.5}Ge_{0.5}$ crystal for different relative strengths of the second phonon path: (a) $\rho = 0$ (b) $\rho = 0.28$ corresponding to the minimum thermal conductivity. The letters "T, L, A, O" represent transverse, longitudinal, acoustic and optical modes, respectively. For example, "TA" denotes the transverse acoustic phonon branch. Black dotted-dashed curves are phonon dispersion of a diatomic lattice of alternating Si and Ge atoms, where only longitudinal modes are present. Mode-dependent Grüneisen parameters $\boldsymbol{\gamma_q}$ of the same $Si_{0.5}Ge_{0.5}$ crystal for (c) $\rho = 0$ (d) $\rho = 0.28$. Open circles and lines from the two different methods. Experimentally measured Grüneisen parameters on the Brillouin zone edge and center are for comparison.*

those for $\rho = 0$. One may then question why a $Si_{0.5}Ge_{0.5}$ crystal with the opening of the second phonon path between the non-nearest neighbours would turn out to be an inefficient thermal conductors. The answer lies in the strong phonon localization due to resonant scattering and large anharmonicity associated with the longitudinal acoustic (LA) mode, making the mean free path significantly shorter.

The Grüneisen parameter $\boldsymbol{\gamma}_{\mathbf{q}}$ associated with each vibrational mode can be obtained with

$$\boldsymbol{\gamma}_{\mathbf{q}} = -\frac{1}{6\omega_{\mathbf{q}}^2} \sum_{ijk} \sum_{\alpha\beta\gamma} \frac{\epsilon_{i\alpha}^{\mathbf{q}*} \epsilon_{j\beta}^{\mathbf{q}}}{\sqrt{M_i M_j}} r_k^{\gamma} \Psi_{ijk}^{\alpha\beta\gamma} \mathrm{e}^{\mathrm{i}\mathbf{q}\cdot\mathbf{r}_j} \tag{5.3}$$

where $\Psi_{ijk}^{\alpha\beta\gamma}$ is the third-order force constant and $\epsilon_{i\alpha}^{\mathbf{q}}$ is the component α associated eigenvector ϵ for atom i. M_i is the mass of atom i, and $\mathbf{r}_i$ is the vector locating its position. The results are summarized in Fig. 5.4(c) and (d). $\boldsymbol{\gamma}_{\mathbf{q}}$ can also be obtained from its definition by using differentiation of the phonon band structure:

$$\boldsymbol{\gamma}_{\mathbf{q}} = -\frac{V}{\omega_{\mathbf{q}}} \frac{\partial \omega_{\mathbf{q}}}{\partial V}. \tag{5.4}$$

By prescribing $\rho = 0.28$, the phonon group velocity $v_{\mathrm{LA}}(\mathbf{k} = \Gamma)$ at the Brillouin zone center increases by 85% compared to the one at $\rho = 0$, whereas the mode Grüneisen parameter $\boldsymbol{\gamma}_{\mathrm{LA}}(\mathbf{k} = \Gamma)$ increases by 490% showing a large anharmonicity characterized by $\boldsymbol{\gamma} = 4.51$ for $\rho = 0.28$ when compared to $\boldsymbol{\gamma} = 0.92$ for $\rho = 0$. The thermal conductivity κ can be approximated as [Tritt (2004)] $\kappa = \sum_{\mathbf{k},\nu} \hbar\omega_{\mathbf{q}} \left(v_{\mathbf{q}}^g\right)^2 \tau_{\mathbf{q}} \frac{\partial}{\partial T} n_{\mathrm{BE}}(\omega_{\mathbf{q}}, T)$, where the relaxation time $\tau_{\mathbf{q}}$ of a phonon mode $\mathbf{q}$ is inversely proportional to the square of its associated Grüneisen constant, that is $\tau_{\mathbf{q}} \propto 1/\boldsymbol{\gamma}_{\mathbf{q}}^2$. The enhancement in v_g is overcompensated by that in $\boldsymbol{\gamma}_{\mathbf{q}}$ for acoustic phonons in the vicinity of the Brillouin zone center. The contribution of optical phonons to the variation of κ remains negligible due to their low group velocities in the range $\rho \in [0, 0.3]$ in spite of their large anharmonicity. These observations yield a first explanation on the reduction of the thermal conductivity κ in Fig. 5.2. Our findings are in line with recent works on the low thermal conductivities of rocksalt IV-VI compounds due to strong anharmonic scattering of the transverse optical phonons [Shiga et al. (2012); Shiga et al. (2014); Lee et al. (2014)].

5.3.5 Anharmonic relaxation time

The anharmonic phonon lifetimes τ in the in $Si_{0.5}Ge_{0.5}$ crystal are shown in Fig. 5.5 for the relative second-NN interactions $\rho = 0, 0.16, 0.28$. The lifetime due to phonon-phonon scattering is related to the imaginary part of the phonon

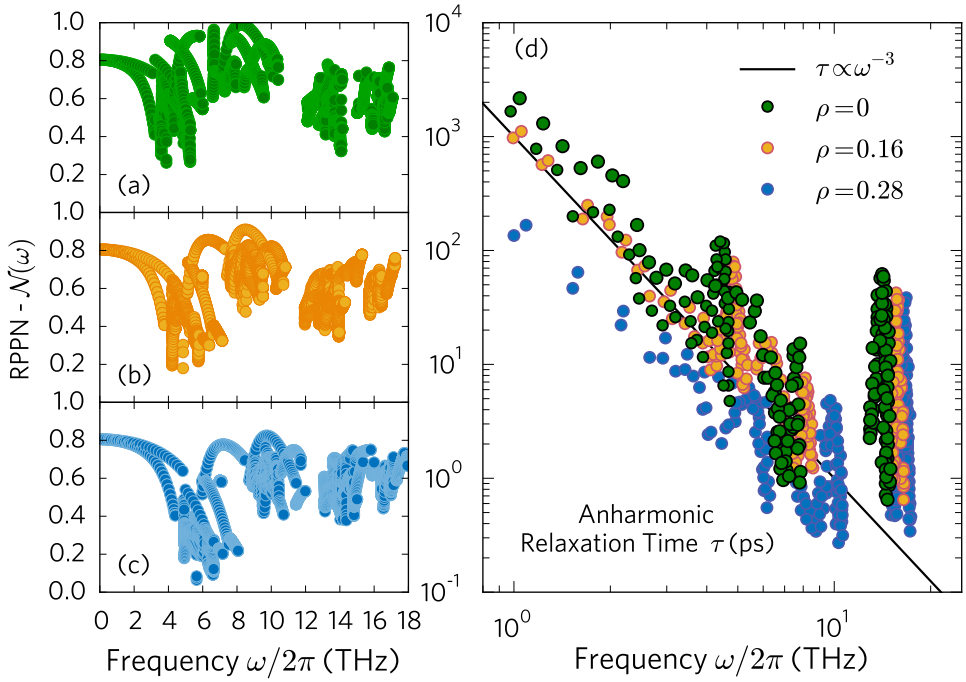

Figure 5.5: *Relative Phonon Participation Number (RPPN) $\mathcal{E}_i\left(\frac{\mathbf{q}}{\omega}\right)$ of $Si_{0.5}Ge_{0.5}$ crystals with relative second-NN interactions (a) $\rho = 0$, (b) $\rho = 0.16$, (c)$\rho = 0.28$. (d) Anharmonic phonon lifetimes $\tau(\omega)$ in $Si_{0.5}Ge_{0.5}$ crystal for different relative second-NN interactions ρ. The band shift is consistent with the phonon dispersion in Fig. 5.4.*

self-energy [Debernardi et al. (1995); Wallace (1998); Lindsay et al. (2012)],

$$1/\tau_{\mathbf{q}} = 2\Gamma_{\mathbf{q}} \tag{5.5}$$

where

$$\begin{aligned}\Gamma_{\mathbf{q}} = \sum_{\mathbf{q}'\mathbf{q}''} \frac{\hbar\pi}{16} \iint_{BZ} \left|\Psi_{\mathbf{q}\mathbf{q}'\mathbf{q}''}\right| \Delta_{\mathbf{q}\mathbf{q}'\mathbf{q}''} \\ \times [(n_{\mathbf{q}'} + n_{\mathbf{q}''} + 1)\delta(\omega_{\mathbf{q}} - \omega_{\mathbf{q}'} - \omega_{\mathbf{q}''}) \\ + 2(n_{\mathbf{q}'} - n_{\mathbf{q}''})\delta(\omega_{\mathbf{q}} - \omega_{\mathbf{q}'} + \omega_{\mathbf{q}''})\mathrm{d}\mathbf{q}'\mathrm{d}\mathbf{q}'']\end{aligned} \tag{5.6}$$

where $\Psi_{\mathbf{q}\mathbf{q}'\mathbf{q}''}$ is the three-phonon matrix. $n_{\mathbf{q}}$ is the equilibrium occupation number for mode $\mathbf{q}$. The delta functions in wave vectors and in frequency ensure the momentum selection rules $\mathbf{q} + \mathbf{q} = \mathbf{q}'' + \mathbf{G}$ for the fusion processes and the energy conservation $\Delta = \omega_{\mathbf{q}} - \omega_{\mathbf{q}'} \pm \omega_{\mathbf{q}''}$. The three-phonon matrix $\Psi_{\mathbf{q}\mathbf{q}'\mathbf{q}''}$ is given by

$$\begin{aligned}\Psi_{\mathbf{q}\mathbf{q}'\mathbf{q}''} = \sum_{ijk}\sum_{\alpha\beta\gamma} \frac{\epsilon^{\mathbf{q}}_{i\alpha}\epsilon^{\mathbf{q}'}_{j\beta}\epsilon^{\mathbf{q}''}_{k\gamma}}{\sqrt{M_i M_j M_k}\sqrt{\omega_{\mathbf{q}}\omega_{\mathbf{q}'}\omega_{\mathbf{q}''}}} \\ \times \Psi^{\alpha\beta\gamma}_{ijk} \mathrm{e}^{\mathrm{i}\mathbf{q}\cdot\mathbf{r}_i + \mathrm{i}\mathbf{q}'\cdot\mathbf{r}_j \mathrm{i}\mathbf{q}''\cdot\mathbf{r}_k}\end{aligned} \tag{5.7}$$

As ρ increases in the range $\rho \in [0,\ 0.3]$, a strong reduction in τ is observed, especially for the acoustic phonons with long wavelengths. This indicates that the phonon interferences due to the opening of the additional phonon path through second-NN interactions can strengthen the anharmonic processes of phonon scattering and severely constrains the phonon propagation.
We note that the strong lattice anharmonicity is not a necessary condition to the low thermal conductivity of solids. Such a claim can be justified by extracting the thermal conductivity κ of $Si_{0.5}Ge_{0.5}$ alloys versus different second-NN bond strengths ρ in molecular dynamics simulations at the temperature $T = 100$ K, as shown in Fig. 5.2. At such a low temperature, a local minimum in κ is however observed in conditions where group velocities, which are not significantly temperature dependent, are increased and inelastic scattering processes are substantially suppressed compared to the case at of $T = 300$ K. This directly demonstrates the predominant role of harmonic phonon interferences in the thermal conductivity of solids despite largely weakened anharmonicity.

The two-path phonon interference carries out significant phonon localization. For a quantitative measure of phonon confinement, we introduce the Relative Phonon Participation Number (RPPN) $\mathcal{N}$:

$$\mathcal{N}\left(\begin{smallmatrix}\mathbf{q}\\ \omega\end{smallmatrix}\right) = \left(\sum_{i=1}^{N} \mathcal{E}_i\left(\begin{smallmatrix}\mathbf{q}\\ \omega\end{smallmatrix}\right)\right)^2 / N \sum_{i=1}^{N} \left[\mathcal{E}_i\left(\begin{smallmatrix}\mathbf{q}\\ \omega\end{smallmatrix}\right)\right]^2, \tag{5.8}$$

where $\mathcal{E}_i\left(\begin{smallmatrix}\mathbf{q}\\ \omega\end{smallmatrix}\right)$, the mean kinetic energy of atom i for a normal mode $\left(\begin{smallmatrix}\mathbf{q}\\ \omega\end{smallmatrix}\right)$ defined by the wave vector $\mathbf{q}$ and the frequency ω, can be found from the corresponding eigenvector $\boldsymbol{\epsilon}_i(\mathbf{q})$, N is the total atom number in the system. $\mathcal{N} \in [0, 1]$ measures the fraction of atoms participating in the normal vibration mode $\left(\begin{smallmatrix}\mathbf{q}\\ \omega\end{smallmatrix}\right)$, cf. Ref. [Bell and Dean (1970)]. Figs. 5.5(a), (b) and (c) present a comparison between the computed $\mathcal{N}(\omega)$ in a $Si_{0.5}Ge_{0.5}$ crystal with the strengths of the second phonon path $\rho = 0, 0.16, 0.28$. In the $Si_{0.5}Ge_{0.5}$ crystal without the second phonon path, as shown in Fig. 5.5(a), the modes in most spectral range are propagative since $\mathcal{N} \gtrsim 0.5$ is characteristic of typical extended phonon modes in a perfect crystal [Bell and Dean (1970)]. But in the crystals with nonnegligible second NN bonds, confined modes with very low $\mathcal{N}(\omega)$ (< 0.2) are observed between 5.1 THz and 7.3 THz. These results demonstrate the strong effect of the two-path phonon interference, $\rho \leq 0.28$, on the phonon confinement and explains the origin of the low thermal conductivity in a crystal with a relatively weak second phonon path.

5.4 Conclusions

In conclusion, we investigate the role of two-path destructive phonon interference induced by long-range interatomic forces on the thermal conductance and conductivity of a silicon-germanium alloy. We provide a "harmonic resistive" mechanism to explain the low thermal conductivity of crystals incorporating long-range interatomic forces with the destructive interferences between multiple phonon paths, in addition to the previous explanation of strong anharmonic scattering due to the softening of the optical phonon bands [Shiga et al. (2012); Shiga et al. (2014); Li et al. (2014); Lee et al. (2014)]. Such interferences offer a new departure in the control of heat conduction through the coherent behaviours of phonons in solids.

Chapter 6

Conclusions and Perspectives

6.1 Conclusions

With a combination of methods including molecular dynamics, phonon Green's function, lattice dynamics, and density functional theory calculations, we have investigated the wave interference of phonons on the nanoscale heat conduction. The main conclusions of this thesis are as follows:

- we provide a comprehensive modeling of atomic-scale phononic metamaterial for the control of heat conduction by exploiting the two-path interference phonon antiresonances. Thermal phonons crossing crystal plane partially filled with resonance defect atoms can undergo complete reflection caused by destructive phonon interference. Such patterned atomic planes can be considered as high-finesse atomic-scale *interference phonon metamirrors*. Interference phonon antiresonances are not deteriorated by the aperiodicity in the defect-atom distribution and the anharmonicity of interatomic bonds. The width of the antiresonance dip provides a measure of the coherence length of the phonon wave packet. And, finally, we would like to emphasize that strong resonance reflection of electromagnetic waves, which has been observed in metafilms partially filled with asymmetrical split-ring arrays, in stereometamaterials, in flexible metasurfaces and in microwave metamirrors, can also be interpreted as interference photon antiresonance in an optically transparent plane, partially filled with subwavelength plasmonic or microwave resonating structures.

- we introduce a novel ultra-compact interference cavity for coherent phonons formed by high-finesse interference mirrors based on atomic-scale semiconductor metamaterials. Through MD simulations We show that the nanocavity stores monochromatic THz lattice waves, which can be used for the phonon lasing - the emission of coherent phonons. Either one- or two-color phonon lasing can be realized depending on the geometry

of the nanodevice. Coherent phonon storage can be achieved by cooling the nanocavity initially thermalized at room temperature or by the pump-probe technique. The confined modes can be released from the nanocavity by applying tunable reversible stress which results in the emission of coherent THz acoustic beams.

- We investigate the role of two-path destructive phonon interference induced by long-range interatomic forces on the thermal conductance and conductivity of a silicon-germanium alloy. We provide a "harmonic resistive" mechanism to explain the low thermal conductivity of crystals incorporating long-range interatomic forces with the destructive interferences between multiple phonon paths, in addition to the previous explanation of strong anharmonic scattering due to the softening of the optical phonon bands. Such interferences offer a new departure in the control of heat conduction through the coherent behaviours of phonons in solids.

6.2 Perspectives

Two perspectives of this thesis could be pursued:

- Phonon interferences might be used to explain the low thermal conductivity of polar materials where the interatomic forces are predominantly long range Coulomb ones. The electrostatic force with respect to the interatomic distance r by following a r^{-2} decay, yielding a relatively strong second nearest neighbor force which is one fourth of the nearest neighbor one. Such an investigation could be achieved by artificially controlling the potential cutoff of the Coulomb force field.

- Phonon interference could play an important role in the thermal transport through molecular junctions in which a single molecule or a whole self-assembled monolayer (SAM) is sandwiched between solid state electrodes has been proposed as very promising candidates for thermoelectric applications. Depending on the scheme of conjugation in the molecule, the electron transmission through the junction may be less affected compared to the phonon counterpart. The tuning of the thermal conductance due to phonon interferences via chemical modifications could be important for thermoelectric applications of molecular junctions.

References

Alaie, S., D. F. Goettler, M. Su, Z. C. Leseman, C. M. Reinke, and I. El-Kady (2015). Thermal transport in phononic crystals and the observation of coherent phonon scattering at room temperature. *Nature communications 6*. *(p. 2, 3, 7)*

Altewischer, E., M. P. Van Exter, and J. P. Woerdman (2002). Plasmon-assisted transmission of entangled photons. *Nature 418*(6895), 304–306. *(p. 45, 75)*

Asadchy, V. S., Y. Radi, J. Vehmas, and S. A. Tretyakov (2015). Functional metamirrors using bianisotropic elements. *Phys. Rev. Lett. 114*, 095503. *(p. 59)*

Ashcroft, N. and N. Mermin (1976). *Solid state physics (Saunders College)(1976)*. Saunders College. *(p. 2)*

Beardsley, R., A. Akimov, M. Henini, and A. Kent (2010). Coherent terahertz sound amplification and spectral line narrowing in a stark ladder superlattice. *Physical review letters 104*(8), 085501. *(p. 62, 66)*

Bell, L. E. (2008). Cooling, heating, generating power, and recovering waste heat with thermoelectric systems. *Science 321*(5895), 1457–1461. *(p. 2, 3)*

Bell, R. and P. Dean (1970). Atomic vibrations in vitreous silica. *Discussions of the Faraday society 50*, 55–61. *(p. 69, 88)*

Beugnon, J., M. P. A. Jones, J. Dingjan, B. Darquié, G. Messin, A. Browaeys, and P. Grangier (2006). Quantum interference between two single photons emitted by independently trapped atoms. *Nature 440*(7085), 779–782. *(p. 46, 76)*

Biswas, K., J. He, I. D. Blum, C.-I. Wu, T. P. Hogan, D. N. Seidman, V. P. Dravid, and M. G. Kanatzidis (2012). High-performance bulk thermoelectrics with all-scale hierarchical architectures. *Nature 489*(7416), 414–418. *(p. 2, 3)*

Cahill, D. G., P. V. Braun, G. Chen, D. R. Clarke, S. Fan, K. E. Goodson, P. Keblinski, W. P. King, G. D. Mahan, A. Majumdar, et al. (2014). Nanoscale thermal transport. ii. 2003–2012. *Applied Physics Reviews 1*(1), 011305. *(p. 2)*

Callaway, J. (1959). Model for lattice thermal conductivity at low temperatures. *Physical Review 113*(4), 1046. *(p. 35)*

Casher, A. and J. Lebowitz (1971a). Heat flow in regular and disordered harmonic chains. *Journal of Mathematical Physics 12*(8), 1701–1711. *(p. 19)*

Casher, A. and J. L. Lebowitz (1971b). Heat flow in regular and disordered harmonic chains. *J. Math. Phys. 12*(8), 1701–1711. *(p. 46)*

Chen, G. and A. Shakouri (2002). Heat transfer in nanostructures for solid-state energy conversion. *Tran. Am. Soc. Mech. Eng. 124*, 242–252. *(p. 46)*

Chen, P., N. A. Katcho, J. P. Feser, W. Li, M. Glaser, O. G. Schmidt, D. G. Cahill, N. Mingo, and A. Rastelli (2013). Role of surface-segregation-driven intermixing on the thermal transport through planar Si/Ge superlattices. *Phys. Rev. Lett. 111*(11), 115901. *(p. 46, 56, 76)*

Chiritescu, C., D. G. Cahill, N. Nguyen, D. Johnson, A. Bodapati, P. Keblinski, and P. Zschack (2007). Ultralow thermal conductivity in disordered, layered wse2 crystals. *Science 315*(5810), 351–353. *(p. 2, 3)*

Chowdhury, I., R. Prasher, K. Lofgreen, G. Chrysler, S. Narasimhan, R. Mahajan, D. Koester, R. Alley, and R. Venkatasubramanian (2009). On-chip cooling by superlattice-based thin-film thermoelectrics. *Nature Nanotechnology 4*(4), 235–238. *(p. 46, 76)*

Colvard, C., R. Merlin, M. Klein, and A. Gossard (1980). Observation of folded acoustic phonons in a semiconductor superlattice. *Physical Review Letters 45*(4), 298. *(p. 3)*

Costescu, R., D. Cahill, F. Fabreguette, Z. Sechrist, and S. George (2004). Ultra-low thermal conductivity in w/al2o3 nanolaminates. *Science 303*(5660), 989–990. *(p. 2)*

Debernardi, A., S. Baroni, and E. Molinari (1995). Anharmonic phonon lifetimes in semiconductors from density-functional perturbation theory. *Physical review letters 75*(9), 1819. *(p. 40, 87)*

Degiron, A., H. J. Lezec, N. Yamamoto, and T. W. Ebbesen (2004). Optical transmission properties of a single subwavelength aperture in a real metal. *Opt. Commun. 239*(1), 61–66. *(p. 56)*

Dove, M. T. (1993). *Introduction to lattice dynamics*, Volume 4. Cambridge university press. *(p. 37)*

Duda, J. C., J. L. Smoyer, P. M. Norris, and P. E. Hopkins (2009). Extension of the diffuse mismatch model for thermal boundary conductance between isotropic and anisotropic materials. *Applied Physics Letters 95*(3), 031912. *(p. 21)*

Estrada, H., P. Candelas, A. Uris, F. Belmar, F. J. G. de Abajo, and F. Meseguer (2008). Extraordinary sound screening in perforated plates. *Phys. Rev. Lett. 101*(8), 084302. *(p. 53)*

Fainstein, A., N. D. Lanzillotti-Kimura, B. Jusserand, and B. Perrin (2013). Strong optical-mechanical coupling in a vertical gaas/alas microcavity for subterahertz phonons and near-infrared light. *Physical review letters 110*(3), 037403. *(p. 62, 66)*

Fano, U. (1961). Effects of configuration interaction on intensities and phase shifts. *Phys. Rev. 124*(6), 1866. *(p. 50)*

Fedotov, V. A., M. Rose, S. L. Prosvirnin, N. Papasimakis, and N. I. Zheludev (2007). Sharp trapped-mode resonances in planar metamaterials with a broken structural symmetry. *Phys. Rev. Lett. 99*(14), 147401. *(p. 45, 59, 75)*

Fellay, A., F. Gagel, K. Maschke, A. Virlouvet, and A. Khater (1997). Scattering of vibrational waves in perturbed quasi-one-dimensional multichannel waveguides. *Phys. Rev. B 55*(3), 1707. *(p. 46, 76)*

García-Meca, C., R. Ortuño, F. J. Rodríguez-Fortuño, J. Martí, and A. Martínez (2009). Negative refractive index metamaterials aided by extraordinary optical transmission. *Opt. Express 17*(8), 6026–6031. *(p. 46, 75)*

Garg, J., N. Bonini, B. Kozinsky, and N. Marzari (2011). Role of disorder and anharmonicity in the thermal conductivity of silicon-germanium alloys: A first-principles study. *Phys. Rev. Lett. 106*(4), 045901. *(p. 54)*

Giannozzi, P., S. Baroni, N. Bonini, M. Calandra, R. Car, C. Cavazzoni, D. Ceresoli, G. L. Chiarotti, M. Cococcioni, I. Dabo, et al. (2009). Quantum espresso: a modular and open-source software project for quantum simulations of materials. *Journal of Physics: Condensed Matter 21*(39), 395502. *(p. 77)*

Grudinin, I. S., H. Lee, O. Painter, and K. J. Vahala (2010). Phonon laser action in a tunable two-level system. *Physical review letters 104*(8), 083901. *(p. 62, 66)*

Han, H., B. Li, S. Volz, and Yu. A. Kosevich (2015). Ultracompact interference phonon nanocapacitor for storage and lasing of coherent terahertz lattice waves. *Phys. Rev. Lett. 114*, 145501. *(p. 47, 76, 77)*

Han, H., L. G. Potyomina, A. N. Darinskii, S. Volz, and Yu. A. Kosevich (2014). Phonon interference and thermal conductance reduction in atomic-scale metamaterials. *Phys. Rev. B 89*(18), 180301. *(p. 47, 50, 59, 62, 63, 64, 67, 76, 77)*

Han, T., X. Bai, D. Gao, J. T. L. Thong, B. Li, and C.-W. Qiu (2014). Experimental demonstration of a bilayer thermal cloak. *Phys. Rev. Lett. 112*(5), 054302. *(p. 47)*

Hochbaum, A. I., R. Chen, R. D. Delgado, W. Liang, E. C. Garnett, M. Najarian, A. Majumdar, and P. Yang (2008). Enhanced thermoelectric performance of rough silicon nanowires. *Nature 451*(7175), 163–167. *(p. 2, 3)*

Holland, M. (1963). Analysis of lattice thermal conductivity. *Physical Review 132*(6), 2461. *(p. 35)*

Hong, C. K., Z. Y. Ou, and L. Mandel (1987). Measurement of subpicosecond time intervals between two photons by interference. *Phys. Rev. Lett. 59*(18), 2044. *(p. 46, 52, 75)*

Hsu, K. F., S. Loo, F. Guo, W. Chen, J. S. Dyck, C. Uher, T. Hogan, E. Polychroniadis, and M. G. Kanatzidis (2004). Cubic agpbmsbte2+ m: Bulk thermoelectric materials with high figure of merit. *Science 303*(5659),

818–821. *(p. 2, 3)*

Huynh, A., N. Lanzillotti-Kimura, B. Jusserand, B. Perrin, A. Fainstein, M. Pascual-Winter, E. Peronne, and A. Lemaître (2006). Subterahertz phonon dynamics in acoustic nanocavities. *Physical review letters 97*(11), 115502. *(p. 62, 70)*

Joannopoulos, J. D., P. R. Villeneuve, and S. Fan (1997). Photonic crystals: putting a new twist on light. *Nature 386*(6621), 143–149. *(p. 2)*

John, S. (1987). Strong localization of photons in certain disordered dielectric superlattices. *Physical review letters 58*(23), 2486. *(p. 2)*

Kaburaki, H., J. Li, S. Yip, and H. Kimizuka (2007). Dynamical thermal conductivity of argon crystal. *J. Appl. Phys. 102*(4), 043514. *(p. 48)*

Kabuss, J., A. Carmele, T. Brandes, and A. Knorr (2012). Optically driven quantum dots as source of coherent cavity phonons: a proposal for a phonon laser scheme. *Physical review letters 109*(5), 054301. *(p. 69)*

Kepesidis, K., S. Bennett, S. Portolan, M. D. Lukin, and P. Rabl (2013). Phonon cooling and lasing with nitrogen-vacancy centers in diamond. *Physical Review B 88*(6), 064105. *(p. 69)*

Khalatnikov, I. M. (2000). *An Introduction to the Theory of Superfluidity*. New York: Westview Press. *(p. 54)*

Khokhlova, T. D., Y.-N. Wang, J. C. Simon, B. W. Cunitz, F. Starr, M. Paun, L. A. Crum, M. R. Bailey, and V. A. Khokhlova (2014). Ultrasound-guided tissue fractionation by high intensity focused ultrasound in an in vivo porcine liver model. *Proceedings of the National Academy of Sciences 111*(22), 8161–8166. *(p. 63)*

Khurgin, J., M. Pruessner, T. Stievater, and W. Rabinovich (2012). Laser-rate-equation description of optomechanical oscillators. *Physical review letters 108*(22), 223904. *(p. 62)*

Kim, W., J. Zide, A. Gossard, D. Klenov, S. Stemmer, A. Shakouri, and A. Majumdar (2006). Thermal conductivity reduction and thermoelectric figure of merit increase by embedding nanoparticles in crystalline semiconductors. *Phys. Rev. Lett. 96*(4), 045901. *(p. 3, 46, 57, 76)*

Kippenberg, T. J. and K. J. Vahala (2008). Cavity optomechanics: back-action at the mesoscale. *science 321*(5893), 1172–1176. *(p. 62)*

Kittel, C. (2005). *Introduction to solid state physics*. Wiley. *(p. 2)*

Klemens, P. (1955). The scattering of low-frequency lattice waves by static imperfections. *Proceedings of the Physical Society. Section A 68*(12), 1113. *(p. 35)*

Kosevich, Yu. A. (1997). Capillary phenomena and macroscopic dynamics of complex two-dimensional defects in crystals. *Prog. in Surf. Sci. 55*(1), 1–57. *(p. 46, 47, 50, 62, 63, 76)*

Kosevich, Yu. A. (2008). Multichannel propagation and scattering of phonons and photons in low-dimension nanostructures. *Physics-Uspekhi 51*(8), 848–859. *(p. 47, 50, 53, 59)*

Kosevich, Yu. A., A. Feher, and E. S. Syrkin (2008). Resonance absorption,

reflection, transmission of phonons and heat transfer through interface between two solids. *Low Temp. Phys. 34*(7), 575–582. *(p. 47)*

Kosevich, Yu. A. and V. V. Gann (2013). Magnon localization and Bloch oscillations in finite Heisenberg spin chains in an inhomogeneous magnetic field. *J. Phys.-Condens. Mat. 25*, 246002. *(p. 52)*

Kosevich, Yu. A. and E. S. Syrkin (1991). Resonant interaction of elastic waves with a planar crystal defect. *Sov. Phys.-Sol. State 33*(7), 1156–1157. *(p. 47, 50)*

Kubo, R., M. Toda, and N. Hashitsume (2012). *Statistical physics II: nonequilibrium statistical mechanics*, Volume 31. Springer Science & Business Media. *(p. 40)*

Kushwaha, M. S., P. Halevi, L. Dobrzynski, and B. Djafari-Rouhani (1993). Acoustic band structure of periodic elastic composites. *Physical Review Letters 71*(13), 2022. *(p. 2)*

Landau, L. D. and E. M. Lifshitz (1991). *Quantum Mechanics (Non-Relativistic Theory)*. Oxford: Pergamon Press. *(p. 52)*

Lang, C., C. Eichler, L. Steffen, J. M. Fink, M. J. Woolley, A. Blais, and A. Wallraff (2013). Correlations, indistinguishability and entanglement in Hong-Ou-Mandel experiments at microwave frequencies. *Nature Phys. 9*(6), 345–348. *(p. 46)*

Lanzillotti-Kimura, N., A. Fainstein, A. Huynh, B. Perrin, B. Jusserand, A. Miard, and A. Lemaître (2007). Coherent generation of acoustic phonons in an optical microcavity. *Physical review letters 99*(21), 217405. *(p. 62, 70)*

Lee, S., K. Esfarjani, T. Luo, J. Zhou, Z. Tian, and G. Chen (2014). Resonant bonding leads to low lattice thermal conductivity. *Nature communications 5*. *(p. 85, 88)*

Li, C., J. Ma, H. Cao, A. May, D. Abernathy, G. Ehlers, C. Hoffmann, X. Wang, T. Hong, A. Huq, et al. (2014). Anharmonicity and atomic distribution of snte and pbte thermoelectrics. *Physical Review B 90*(21), 214303. *(p. 88)*

Li, N., J. Ren, L. Wang, G. Zhang, P. Hänggi, and B. Li (2012a). Colloquium: Phononics: Manipulating heat flow with electronic analogs and beyond. *Reviews of Modern Physics 84*(3), 1045. *(p. 62)*

Li, N., J. Ren, L. Wang, G. Zhang, P. Hänggi, and B. Li (2012b). Phononics: Manipulating heat flow with electronic analogs and beyond. *Rev. Mod. Phys. 84*(3), 1045. *(p. 47)*

Lindsay, L., D. Broido, and T. Reinecke (2012). Thermal conductivity and large isotope effect in gan from first principles. *Physical review letters 109*(9), 095901. *(p. 40, 87)*

Liu, N., H. Liu, S. Zhu, and H. Giessen (2009). Stereometamaterials. *Nat. Photonics 3*(3), 157–162. *(p. 45, 59, 75)*

Liu, Z., X. Zhang, Y. Mao, Y. Y. Zhu, Z. Yang, C. T. Chan, and P. Sheng (2000). Locally resonant sonic materials. *Science 289*(5485), 1734–1736.

(p. 2, 53, 56)

Luckyanova, M. N., J. Garg, K. Esfarjani, A. Jandl, M. T. Bulsara, A. J. Schmidt, A. J. Minnich, S. Chen, M. S. Dresselhaus, Z. Ren, et al. (2012). Coherent phonon heat conduction in superlattices. *Science 338*(6109), 936–939. *(p. 2, 3, 4, 76)*

Mahboob, I., K. Nishiguchi, A. Fujiwara, and H. Yamaguchi (2013). Phonon lasing in an electromechanical resonator. *Physical review letters 110*(12), 127202. *(p. 62, 72)*

Mahboob, I., K. Nishiguchi, H. Okamoto, and H. Yamaguchi (2012). Phonon-cavity electromechanics. *Nature Physics 8*(5), 387–392. *(p. 62)*

Maldovan, M. (2013). Narrow low-frequency spectrum and heat management by thermocrystals. *Phys. Rev. Lett. 110*(2), 025902. *(p. 2, 3, 7, 47)*

Maryam, W., A. Akimov, R. Campion, and A. Kent (2013). Dynamics of a vertical cavity quantum cascade phonon laser structure. *Nature communications 4*. *(p. 62, 66)*

Mendonca, J. T., H. Terças, G. Brodin, and M. Marklund (2010). A phonon laser in ultra-cold matter. *EPL (Europhysics Letters) 91*(3), 33001. *(p. 62)*

Mingo, N., D. Hauser, N. P. Kobayashi, M. Plissonnier, and A. Shakouri (2009). "Nanoparticle-in-Alloy" approach to efficient thermoelectrics: Silicides in SiGe. *Nano Lett. 9*(2), 711–715. *(p. 46, 76)*

Mingo, N. and L. Yang (2003). Phonon transport in nanowires coated with an amorphous material: An atomistic green's function approach. *Physical Review B 68*(24), 245406. *(p. 21, 80)*

Mitrofanov, O., M. Lee, J. M. P. Hsu, L. N. Pfeiffer, K. W. West, J. D. Wynn, and J. F. Federici (2001). Terahertz pulse propagation through small apertures. *Appl. Phys. Lett. 79*(7), 907–909. *(p. 56)*

Narayana, S. and Y. Sato (2012). Heat flux manipulation with engineered thermal materials. *Phys. Rev. Lett. 108*(21), 214303. *(p. 47)*

Narayanamurti, V., H. Störmer, M. Chin, A. Gossard, and W. Wiegmann (1979). Selective transmission of high-frequency phonons by a superlattice: The" dielectric" phonon filter. *Physical Review Letters 43*(27), 2012. *(p. 3)*

Okamoto, H., A. Gourgout, C.-Y. Chang, K. Onomitsu, I. Mahboob, E. Y. Chang, and H. Yamaguchi (2013). Coherent phonon manipulation in coupled mechanical resonators. *Nature Physics 9*(8), 480–484. *(p. 62)*

Padture, N. P., M. Gell, and E. H. Jordan (2002). Thermal barrier coatings for gas-turbine engine applications. *Science 296*(5566), 280–284. *(p. 2)*

Pernot, G., M. Stoffel, I. Savic, F. Pezzoli, P. Chen, G. Savelli, A. Jacquot, J. Schumann, U. Denker, I. Mönch, et al. (2010). Precise control of thermal conductivity at the nanoscale through individual phonon-scattering barriers. *Nat. Mater. 9*(6), 491–495. *(p. 46, 76)*

Plimpton, S. (1995). Fast parallel algorithms for short-range molecular dynamics. *J. Comput. Phys. 117*(1), 1–19. Available at `http://lammps.`

sandia.gov. *(p. 49, 64, 77)*

Poudel, B., Q. Hao, Y. Ma, Y. Lan, A. Minnich, B. Yu, X. Yan, D. Wang, A. Muto, D. Vashaee, et al. (2008). High-thermoelectric performance of nanostructured bismuth antimony telluride bulk alloys. *Science 320*(5876), 634–638. *(p. 2, 3)*

Puller, V., B. Lounis, and F. Pistolesi (2013). Single molecule detection of nanomechanical motion. *Physical review letters 110*(12), 125501. *(p. 63, 73)*

Rajabpour, A. and S. Volz (2010). Thermal boundary resistance from mode energy relaxation times: Case study of argon-like crystals by molecular dynamics. *Journal of Applied Physics 108*(9), 094324. *(p. 34)*

Ravichandran, J., A. K. Yadav, R. Cheaito, P. B. Rossen, A. Soukiassian, S. Suresha, J. C. Duda, B. M. Foley, C.-H. Lee, Y. Zhu, et al. (2014). Crossover from incoherent to coherent phonon scattering in epitaxial oxide superlattices. *Nature materials 13*(2), 168–172. *(p. 2, 3, 7, 64, 76)*

Rubin, R. J. and W. L. Greer (1971a). Abnormal lattice thermal conductivity of a one-dimensional, harmonic, isotopically disordered crystal. *Journal of Mathematical Physics 12*(8), 1686–1701. *(p. 19)*

Rubin, R. L. and W. L. Greer (1971b). Abnormal lattice thermal conductivity of a one-dimensional, harmonic, isotopically disordered crystal. *J. Math. Phys. 12*(8), 1686–1701. *(p. 46)*

Santori, C., D. Fattal, J. Vučković, G. S. Solomon, and Y. Yamamoto (2002). Indistinguishable photons from a single-photon device. *Nature 419*(6907), 594–597. *(p. 46, 76)*

Savin, A. V. and Yu. A. Kosevich (2014). Thermal conductivity of molecular chains with asymmetric potentials of pair interactions. *Phys. Rev. E 89*(3), 032102. *(p. 47)*

Schelling, P., S. Phillpot, and P. Keblinski (2002a). Phonon wave-packet dynamics at semiconductor interfaces by molecular-dynamics simulation. *Applied Physics Letters 80*(14), 2484–2486. *(p. 21, 23)*

Schelling, P., S. Phillpot, and P. Keblinski (2004). Kapitza conductance and phonon scattering at grain boundaries by simulation. *Journal of Applied Physics 95*(11), 6082–6091. *(p. 21, 23)*

Schelling, P. K. and S. R. Phillpot (2003). Multiscale simulation of phonon transport in superlattices. *J. Appl. Phys. 93*(9), 5377–5387. *(p. 58)*

Schelling, P. K., S. R. Phillpot, and P. Keblinski (2002b). Phonon wave-packet dynamics at semiconductor interfaces by molecular-dynamics simulation. *Appl. Phys. Lett. 80*(14), 2484–2486. *(p. 49)*

Schimka, L., J. Harl, A. Stroppa, A. Grüneis, M. Marsman, F. Mittendorfer, and G. Kresse (2010). Accurate surface and adsorption energies from many-body perturbation theory. *Nature Materials 9*(9), 741–744. *(p. 19)*

Shiga, T., T. Murakami, T. Hori, O. Delaire, and J. Shiomi (2014). Origin of anomalous anharmonic lattice dynamics of lead telluride. *Applied Physics Express 7*(4), 041801. *(p. 85, 88)*

Shiga, T., J. Shiomi, J. Ma, O. Delaire, T. Radzynski, A. Lusakowski, K. Esfarjani, and G. Chen (2012). Microscopic mechanism of low thermal conductivity in lead telluride. *Physical Review B 85*(15), 155203. *(p. 85, 88)*

Simkin, M. and G. Mahan (2000). Minimum thermal conductivity of superlattices. *Physical Review Letters 84*(5), 927. *(p. 2, 3)*

Snyder, G. J. and E. S. Toberer (2008). Complex thermoelectric materials. *Nature materials 7*(2), 105–114. *(p. 2, 3)*

Srivastava, G. P. (1990). *The physics of phonons*. CRC Press. *(p. 37)*

Steele, B. C. and A. Heinzel (2001). Materials for fuel-cell technologies. *Nature 414*(6861), 345–352. *(p. 2)*

Stillinger, F. H. and T. A. Weber (1985a). Computer simulation of local order in condensed phases of silicon. *Physical review B 31*(8), 5262. *(p. 24)*

Stillinger, F. H. and T. A. Weber (1985b). Computer simulation of local order in condensed phases of silicon. *Phys. Rev. B 31*(8), 5262–5271. *(p. 48, 54, 64, 77)*

Swartz, E. T. and R. O. Pohl (1989). Thermal boundary resistance. *Reviews of modern physics 61*(3), 605. *(p. 20)*

Tadano, T., Y. Gohda, and S. Tsuneyuki (2014). Anharmonic force constants extracted from first-principles molecular dynamics: applications to heat transfer simulations. *Journal of Physics: Condensed Matter 26*(22), 225402. *(p. 79)*

Thomas, J. A., J. E. Turney, R. M. Iutzi, C. H. Amon, and A. J. McGaughey (2010). Predicting phonon dispersion relations and lifetimes from the spectral energy density. *Physical Review B 81*(8), 081411. *(p. 37)*

Tian, B., X. Zheng, T. J. Kempa, Y. Fang, N. Yu, G. Yu, J. Huang, and C. M. Lieber (2007). Coaxial silicon nanowires as solar cells and nanoelectronic power sources. *Nature 449*(7164), 885–889. *(p. 2)*

Tian, Y., P. Navarro, and M. Orrit (2014). Single molecule as a local acoustic detector for mechanical oscillators. *Physical review letters 113*(13), 135505. *(p. 63, 73)*

Toberer, E. S., L. L. Baranowski, and C. Dames (2012). Advances in thermal conductivity. *Annual Review of Materials Research 42*, 179–209. *(p. 2, 3)*

Trigo, M., A. Bruchhausen, A. Fainstein, B. Jusserand, and V. Thierry-Mieg (2002). Confinement of acoustical vibrations in a semiconductor planar phonon cavity. *Physical review letters 89*(22), 227402. *(p. 62, 70)*

Tritt, T. M. (2004). *Thermal conductivity: theory, properties, and applications*. Springer Science & Business Media. *(p. 85)*

Turney, J., E. Landry, A. McGaughey, and C. Amon (2009). Predicting phonon properties and thermal conductivity from anharmonic lattice dynamics calculations and molecular dynamics simulations. *Physical Review B 79*(6), 064301. *(p. 37)*

Vahala, K., M. Herrmann, S. Knünz, V. Batteiger, G. Saathoff, T. W. Hän-

sch, and T. Udem (2009). A phonon laser. *Nature Physics 5*(9), 682–686. *(p. 62, 72)*

Venkatasubramanian, R., E. Siivola, T. Colpitts, and B. O'quinn (2001). Thin-film thermoelectric devices with high room-temperature figures of merit. *Nature 413*(6856), 597–602. *(p. 2, 3)*

Vineis, C. J., A. Shakouri, A. Majumdar, and M. G. Kanatzidis (2010). Nanostructured thermoelectrics: big efficiency gains from small features. *Advanced Materials 22*(36), 3970–3980. *(p. 2)*

Walia, S., C. M. Shah, P. Gutruf, H. Nili, D. R. Chowdhury, W. Withayachumnankul, M. Bhaskaran, and S. Sriram (2015). Flexible metasurfaces and metamaterials: A review of materials and fabrication processes at micro- and nano-scales. *Appl. Phys. Rev. 2*, 011303. *(p. 45, 59)*

Wallace, D. C. (1998). *Thermodynamics of crystals*. Courier Corporation. *(p. 40, 87)*

Wang, J., Y. Hashimoto, J. Kono, A. Oiwa, H. Munekata, G. Sanders, and C. Stanton (2005). Propagating coherent acoustic phonon wave packets in in x mn 1- x as/ ga sb. *Physical Review B 72*(15), 153311. *(p. 3)*

Wang, S. M., S. Y. Mu, C. Zhu, Y. X. Gong, P. Xu, H. Liu, T. Li, S. Zhu, and X. Zhang (2012). Hong-Ou-Mandel interference mediated by the magnetic plasmon waves in a three-dimensional optical metamaterial. *Opt. Express 20*(5), 5213–5218. *(p. 46, 76)*

Wang, X., H. Lee, Y. Lan, G. Zhu, G. Joshi, D. Wang, J. Yang, A. Muto, M. Tang, J. Klatsky, et al. (2008). Enhanced thermoelectric figure of merit in nanostructured n-type silicon germanium bulk alloy. *Applied Physics Letters 93*(19), 193121. *(p. 82)*

Xu, H., X. Shi, F. Gao, H. Sun, and B. Zhang (2014). Ultrathin three-dimensional thermal cloak. *Phys. Rev. Lett. 112*(5), 054301. *(p. 47)*

Yablonovitch, E. (1987). Inhibited spontaneous emission in solid-state physics and electronics. *Physical review letters 58*(20), 2059. *(p. 2)*

Zebarjadi, M., K. Esfarjani, M. Dresselhaus, Z. Ren, and G. Chen (2012). Perspectives on thermoelectrics: from fundamentals to device applications. *Energy & Environmental Science 5*(1), 5147–5162. *(p. 2)*

Zen, N., T. A. Puurtinen, T. J. Isotalo, S. Chaudhuri, and I. J. Maasilta (2014). Engineering thermal conductance using a two-dimensional phononic crystal. *Nature communications 5*. *(p. 2, 3, 7)*

Zhang, L., P. Keblinski, J.-S. Wang, and B. Li (2011). Interfacial thermal transport in atomic junctions. *Phys. Rev. B 83*(6), 064303. *(p. 47)*

Zhao, H. and J. Freund (2005). Lattice-dynamical calculation of phonon scattering at ideal si–ge interfaces. *Journal of applied physics 97*(2), 024903. *(p. 21)*

Ziman, J. M. (1960). *Electrons and phonons: the theory of transport phenomena in solids*. Oxford University Press. *(p. 12, 35)*